

AN ABSTRACT OF THE THESIS OF

David H. Katzev for the degree of Master of Science in Civil Engineering presented  
on January 14, 1992.

Title: Simulation of Coastal Processes in a Circular Wave Basin

Abstract approved: Redacted for Privacy  
William G. McDougal

The circular wave basin provides a means of physically modeling the nearshore without the typical problems associated with end walls. Three different coastal processes were examined to demonstrate the use of a spiral wavemaker in a circular wave basin. These were longshore currents, shear waves, and groin circulation. A beach was designed and constructed to concentrate breaking in a narrow region and minimize wave reflection. Currents in the longshore direction were generated by both the motion of the wavemaker and oblique wave approach. Two methods for measuring nearshore currents were employed. First, a 3-D acoustic current meter was positioned at various locations in the cross shore and the local radial and tangential velocities were recorded. Second, a video camera was placed approximately 8 meters above the wave basin to record the motion of a ball in the nearshore. The video tape was digitized by an image processor and the motion of the ball was determined.

Measurements of nearshore circulation in the circular wave basin were used to

investigate longshore currents, shear waves, and groin circulation. Average measured longshore current profiles in the cross shore were compared with numerical model predictions. An analysis of the existence of shear waves in the circular wave basin was performed by calculating longshore and cross shore current spectra. Particular attention was focused on the low frequency end of the spectra where shear waves are most energetic. Model groins were placed in the circular wave basin and measured currents were compared to predicted circulation patterns. All three applications indicated that the circular wave basin is a useful device for simulating coastal processes in a laboratory environment.

**Simulation of Coastal Processes in a Circular Wave Basin**

**by**

**David H. Katzев**

**A THESIS**

**submitted to**

**Oregon State University**

**in partial fulfillment of  
the requirements for the  
degree of**

**Master of Science**

**Completed January 14, 1992**

**Commencement June, 1992**

Thesis Approval:

*Redacted for Privacy*

William G. McDougal, Professor in charge of major

*Redacted for Privacy*

Wayne C. Huber, Head of Civil Engineering

*Redacted for Privacy*

David H. Katzev

Date Thesis is presented: January 14, 1992

Typed by: David H. Katzev

Formatted by: David H. Katzev

## Acknowledgments

While at Oregon State University, I was fortunate to have the opportunity to do research in the ocean engineering department at the O.H. Hinsdale Wave Research Lab. I would like to especially thank my major professor, William G. McDougal, for continually providing me with challenging work and for many enjoyable games of basketball. I would like to thank the Wave Research Lab staff; Chuck Sollitt, Terry Dibble, Bill Hollings, and Dave Standley for their assistance and encouragement with all phases of the experiment. I would also like to thank Andy Jansky for finally putting together a tracking system that worked. Finally, I would like to thank the students for creating a fun learning environment and to Cherly Zedwick for helping me figure out WordPerfect. This research was possible with a grant to OSU from the Office of Naval Research under the University Research Initiative contract #N00014-86-K-0687.

Table of Contents

	<u>Page</u>
Chapter 1 Introduction	1
1.1 Motivation for Research	1
1.2 Background	2
1.3 Objectives	4
Chapter 2 Spiral Wavemaker and Circular Wave Basin	6
2.1 Spiral Wavemaker	6
2.2 Beach Profile	14
2.3 Reflection and Circulation	16
Chapter 3 Longshore Currents	35
3.1 Introduction	35
3.2 Longshore Current Model	37
3.3 Longshore Current Experiments	41
3.4 Longshore Current Data Analysis	47
Chapter 4 Shear Waves	67
4.1 Introduction	67
4.2 Theoretical Background	68
4.3 Shear Wave Experimental Analysis	71

Table of Contents cont.

	<u>Page</u>
<b>Chapter 5 Groins</b>	82
<b>5.1 Introduction</b>	82
<b>5.2 Groin Design and Predicted Circulation</b>	84
<b>5.3 Groin Circulation Experiments</b>	86
<b>Chapter 6 Conclusions</b>	94
<b>6.1 Summary of Results</b>	94
<b>6.2 Future Research</b>	95
<b>References</b>	97
<b>Appendix A</b>	100

## List of Figures

<u>Figure</u>	<u>Page</u>
2.1 Plan view of spiral wavemaker and circular wave basin.	8
2.2 Side view of spiral wavemaker and circular wave basin.	9
2.3 Radial decay of waves for small spiral wavemaker (Elsasser, 1989).	10
2.4 Measured vs. predicted wave heights (Elsasser, 1989).	10
2.5 Predicted and measured two component wave forms (Elsasser, 1989).	12
2.6 Input and measured spectra for 11 component wave system (Elsasser, 1989).	12
2.7 Random wave spectra: $H_s=0.20$ in, $T_p=2.0$ sec (Elsasser, 1989).	13
2.8 Random wave spectra: $H_s=0.20$ in, $T_p=2.0$ sec (Elsasser, 1989).	13
2.9 Beach profile design.	15
2.10 Sheet metal templates and placement in wave basin.	17
2.11 Finished beach in wave basin.	18
2.12 Experimental setup.	18
2.13 Wave profile 142 cm from wavemaker: $T=1.0$ sec, $H=7.6$ cm.	20
2.14 Wave profile 97 cm from wavemaker: $T=1.0$ sec, $H=7.6$ cm.	20
2.15 Wave profile 142 cm from wavemaker: $T_1=0.5$ sec, $T_2=1.0$ sec.	21
2.16 Wave profile 97 cm from wavemaker: $T_1=0.5$ sec, $T_2=1.0$ sec.	21
2.17 Wave profile 142 cm from wavemaker: 11 component wave.	22
2.18 Wave profile 97 cm from wavemaker: 11 component wave.	22
2.19 Tangential velocity 137 cm from wavemaker: No fins.	27
2.20 Tangential velocity 137 cm from wavemaker: With fins.	27
2.21 Tangential velocity 117 cm from wavemaker: No fins.	28
2.22 Tangential velocity 117 cm from wavemaker: With fins.	28
2.23 Tangential velocity 97 cm from wavemaker: No fins.	29
2.24 Tangential velocity 97 cm from wavemaker: With fins.	29
2.25 Mean tangential velocity with and without fins: $T=1.0$ sec, $H=7.6$ cm.	32

List of Figures cont.

<u>Figure</u>	<u>Page</u>
2.26 Tangential and radial velocity with fins: T=2.0 sec, H=4.2 cm.	32
2.27 Repeatability test for mean tangential velocity: T=2.0 sec, H=4.2 cm.	33
2.28 Stationarity test for mean tangential velocity with fins: T=1.0 sec, H=7.6 cm (#1) and T=2.0 sec, H=4.2 cm (#2).	33
3.1 Plan and profile view of surf zone (McDougal and Hudspeth, 1986).	36
3.2 Longshore current profile for a plane beach calculated with NMLONG.	40
3.3 Longshore current profile for a convex beach calculated with NMLONG.	40
3.4 Experimental setup with video camera.	43
3.5 Coordinate system for velocities in circular wave basin.	49
3.6 Tangential velocity for two cases: T=0.8 sec, H=4.88 cm.	50
3.7 Average tangential velocity for two cases: T=0.8 sec, H=4.88 cm.	50
3.8 Tangential velocity for two cases: T=1.0 sec, H=7.6 cm.	51
3.9 Average tangential velocity for two cases: T=1.0 sec, H=7.6 cm.	51
3.10 Tangential velocity for two cases: T=1.2 sec, H=6.65 cm.	52
3.11 Average tangential velocity for two cases: T=1.2 sec, H=6.65 cm.	52
3.12 Tangential velocity for two cases: T <sub>1</sub> =0.5 sec, T <sub>2</sub> =1.0 sec.	53
3.13 Average tangential velocity for two cases: T <sub>1</sub> =0.5 sec, T <sub>2</sub> =1.0 sec.	53
3.14 Tangential velocity for three cases: 11 component wave.	54
3.15 Average tangential velocity for three cases: 11 component wave.	54
3.16 Average tangential velocity vs. cross shore distance in circular wave basin: T=0.8 sec, H=4.88 cm.	56
3.17 Average tangential velocity vs. cross shore distance in circular wave basin: T=1.0 sec, H=7.6 cm.	57
3.18 Average tangential velocity vs. cross shore distance in circular wave basin: T=1.2 sec, H=6.65 cm.	58
3.19 Startup conditions for 30 sec data segments: T=1.0 sec, H=7.6 cm.	59

List of Figures cont.

<u>Figure</u>	<u>Page</u>
3.20 Circulation at end of run for 15 sec data segments: T=1.0 sec, H=7.6 cm.	59
3.21 Comparison of tangential velocity taken with the video and current meter: T=1.0 sec, H=7.6 cm.	60
3.22 Method for calculating the angle of incidence of a spiral wave in the circular wave basin.	62
3.23 NMLONG profile and longshore current meter data: T=1.0 sec, H=7.6 cm, $\theta=4^\circ$ .	64
3.24 NMLONG profile and video measured longshore current data: T=1.0 sec, H=7.6 cm, $\theta=4^\circ$ .	64
3.25 NMLONG profile and video measured longshore current data: T=0.8 sec, H=4.88 cm, $\theta=4^\circ$ .	65
3.26 NMLONG profile and video measured longshore current data: T=1.2 sec, H=6.65 cm, $\theta=4^\circ$ .	65
4.1 Longshore velocity 142 cm from wavemaker: T=1.0 sec, H=7.6 cm.	73
4.2 Longshore velocity spectrum: T=1.0 sec, H=7.6 cm.	73
4.3 Cross shore velocity 142 cm from wavemaker: T=1.0 sec, H=7.6 cm.	74
4.4 Cross shore velocity spectrum: T=1.0 sec, H=7.6 cm.	74
4.5 Wave profile 142 cm from wavemaker: T=1.0 sec, H=7.6 cm.	75
4.6 Wave profile spectrum: T=1.0 sec, H=7.6 cm.	75
4.7 Low frequency spectrum for longshore velocity: T=1.0 sec, H=7.6 cm.	76
4.8 Low frequency spectrum for cross shore velocity: T=1.0 sec, H=7.6 cm.	76
4.9 Low frequency spectrum for wave profile: T=1.0 sec, H=7.6 cm.	76
4.10 Cross shore velocity measured with video: T=1.0 sec, H=7.6 cm.	78
4.11 Cross shore video velocity spectrum: T=1.0 sec, H=7.6 cm.	78
4.12 Longshore velocity measured with video: T=1.0 sec, H=7.6 cm.	79
4.13 Longshore video velocity spectrum: T=1.0 sec, H=7.6 cm.	79

List of Figures cont.

<u>Figure</u>	<u>Page</u>
4.14 Low frequency spectrum for cross shore (U) and longshore (V) velocities measured with the video: T=1.0 sec, H=7.6 cm.	81
5.1a Adjusted shoreline for a single groin.	83
5.1b Adjusted shoreline for a system of groins.	83
5.2 Groin design and placement in circular wave basin.	85
5.3a Generation of rip current within two groins (Dean, 1978).	87
5.3b Generation of cell circulation within two groins (Dean, 1978).	87
5.4 Velocity vector field with one groin: T=1.0 sec, H=7.6 cm.	89
5.5 Velocity vector field with two groins: T=1.0 sec, H=7.6 cm.	90
5.6 Average longshore velocity with and without groins: T=1.0 sec, H=7.6 cm.	92

List of Tables

<u>Table</u>	<u>Page</u>
2.1 Wave height data	23
2.2 Current meter data	30
3.1 Video data for longshore current experiment	45

List of Symbols

a	wave amplitude
$a_i$	amplitude of incident wave
$a_r$	amplitude of reflected wave
$A_1$	Fourier coefficient
$A_2$	Fourier coefficient
$B_1$	Fourier coefficient
$B_2$	Fourier coefficient
C	numerical constant
$C_f$	bottom friction coefficient
$c_p$	phase velocity
d	total water depth
e	exponential constant
f	frequency
g	acceleration due to gravity
h	still water depth
$h_x$	bottom slope
H	wave height
$H_s$	significant wave height
i	complex number
j	counter
k	local wave number
$k_o$	deep water wave number
$K_r$	reflection coefficient
L	wavelength
$L_o$	deep water wavelength
MWL	mean water level

List of Symbols cont.

$n$	linear wave theory term
$N$	numerical constant
$r, \Theta$	radial and angular coordinate
$s$	wavemaker stroke amplitude
$S_{xy}$	onshore-longshore component of radiation stress
$SWL$	still water level
$t$	time
$T$	wave period
$T_p$	peak wave period
$u$	cross shore velocity
$\mathbf{u}$	total velocity vector
$v$	longshore velocity
$V$	depth and time averaged longshore current
$V_r$	radial velocity
$V_\theta$	tangential velocity
$V_x$	velocity in x-direction
$V_y$	velocity in y-direction
$x, y$	horizontal surface coordinates
$x_B$	distance from shoreline to breaker line
$z$	vertical depth coordinate
$\alpha$	numerical constant
$\Delta$	delta
$\epsilon_r$	phase angle of reflected wave
$\eta$	water surface elevation
$\langle \eta \rangle$	wave setup/setdown
$\theta$	incident wave angle
$\theta_b$	incident wave angle at breaker line
$\kappa$	breaker index

List of Symbols cont.

$\mu$	radial wave decay factor
$\mu_e$	eddy viscosity coefficient
$\rho$	density of water
$\sigma$	angular wave frequency
$\tau_{by}$	longshore component of bottom stress
$\psi$	stream function

# **Simulation of Coastal Processes in a Circular Wave Basin**

## **Chapter 1**

### **Introduction**

#### **1.1 Motivation for Research**

Nearshore field experiments are both difficult and expensive. Adverse conditions such as storms and large waves which can result in significant erosion are often the most interesting cases. Storms are also the most difficult events to monitor. Large waves are extremely energetic and can damage experimental instruments such as wave gauges, current meters, and pressure transducers. An ideal situation is to study coastal processes in a controlled environment. As a result, a great deal of coastal research has been done in wave research laboratories.

Most laboratory wave basins are rectangular. In a rectangular basin, longshore currents can be created by incident waves approaching the beach at an oblique angle. However, the length of the surf zone in the longshore direction is limited by the tank width. Coastal studies involving longshore processes are difficult to simulate due to end wall effects. In a circular basin it is possible to simulate a wave breaking on a infinitely long beach. The wavemaker in a circular basin generates a wave by

oscillating eccentrically about a center axis. When viewed from above, the wave crest has a spiral shape and hence, this type of wavemaker is called a spiral wavemaker. As the spiral wave propagates away from the wavemaker, both the wave height and angle of incidence decrease with distance from the wavemaker. With the addition of a beach around the circumference of the basin, a long stretch of coastline is simulated around the perimeter of the basin. Because the wave breaks on the beach at an angle, a longshore current is generated. With no end wall effects, it is possible to more realistically study the behavior of nearshore circulation and sediment transport in a laboratory setting.

## 1.2 Background

The spiral wavemaker in a circular wave basin offers a new tool for the experimental investigation of coastal processes. In this study, three different examples of coastal currents were examined; longshore currents, shear waves, and groin circulation. These three cases were selected to demonstrate the usefulness of the spiral wavemaker for studying coastal processes.

When waves break at an oblique angle to the shoreline, a longshore current is developed that flows parallel to the coast. Longuet-Higgins (1970a,b) developed an early model to predict longshore currents based on radiation stresses. Radiation stress is defined as the excess flux of momentum due to the presence of waves. In determining the magnitude of the longshore current, the radiation stress model is used because in wave breaking, momentum is conserved where as energy is dissipated. If

there is a gradient in this momentum flux, then there is a force. Waves which break at an angle to the coastline have a radiation stress gradient in the cross shore direction. This is the major forcing mechanism for the longshore current.

A new class of waves have recently been discovered in the nearshore. These waves are the result of a shear instability which can occur with a steady longshore current. Holman and Bowen (1989) refer to these waves as shear waves. The theory is based on the conservation of potential vorticity and the forcing is due to the shear of the longshore current. For shear waves to be trapped in the nearshore, the longshore current profile must have an inflection point. This is the case for the longshore current on most natural beach profiles. Oltman-Shay, et al (1989) measured shear waves in the field. They were found to be very energetic with velocities of the same order of magnitude as the longshore current.

Knowledge of nearshore circulation is important to the coastal engineer in design of shoreline structures. Groins and jetties are examples of structures utilized in the coastal region. Groins and jetties are constructed in the surf zone and alter the longshore transport of sand. Groins are often built to stabilize beaches and can create both accretion and erosion along a stretch of coastline. Jetties can provide safe navigational channels and entrances to harbors or bays by reducing the effects of wave shoaling. Both groins and jetties interact with incoming waves and thus alter the nearshore current system in the coastal zone.

### 1.3 Objectives

The major goal of this research is to demonstrate the usefulness of the spiral wavemaker in a circular wave basin for studying coastal processes. By constructing a beach in the wave basin, it will be possible to simulate an infinitely long stretch of coastline. With the spiral wavemaker, it is possible to vary the wave height and wave period. Both monochromatic and random wave conditions will be analyzed with respect to wave height and current data. Two methods will be employed to measure radial and tangential circulation which in effect are cross shore and longshore velocities, respectively. A current meter will only be used in the offshore, outside of the surf zone due to the shallow water depths in the nearshore. A video camera will be set up directly over the wave basin to film an object circulating with the wave motion. Software integrated with an image processor will enable the object to be tracked in time in order to calculate velocities. The video method will enable currents in the surf zone to be analyzed where the current meter could not be used.

Three different examples of coastal processes will be examined. First, a longshore current model and solution will be analyzed for the circular wave basin with the insertion of a specific beach slope. Currents will be measured with both the current meter and the video system. Measured current data in the longshore direction will be averaged in the cross shore direction and compared with numerical model solutions for longshore currents. Second, spectral analysis of the current data will be performed to determine if shear waves exist in the circular wave basin. Special attention will be focused to the low frequency end of the spectrum for the longshore

current where shear waves are believed to be most energetic. Finally, groins will be inserted in the circular wave basin. The groins will be aligned perpendicular to the shoreline to interrupt the flow of the longshore current. The effects that these structures have on currents and circulation will be presented.

## Chapter 2

### Spiral Wavemaker and Circular Wave Basin

#### 2.1 Spiral Wavemaker

A review of the literature and research on a spiral wavemaker in a circular wave basin shows that it is possible to simulate coastal processes in a laboratory environment. Dalrymple and Dean (1973) presented a linear spiral wavemaker theory and demonstrated the usefulness of a spiral wavemaker for experimental littoral drift studies. It was clear from their work that a circular wave basin could provide an effective means to study nearshore processes. Mei (1973) presented an analysis of spiral waves with the addition of a sloping bottom with circular contours. Williams and McDougal (1989) developed a linear solution for a spiral wavemaker considering the gap between the bottom side of the wavemaker and the tank. Elsasser (1989) examined a random spiral wavemaker and circular wave basin. His results, based on linear superposition, compared favorably with laboratory measurements.

The O.H. Hinsdale Wave Research Lab (WRL) at Oregon State University maintains four wave basins which can simulate ocean waves. The west wing houses the original wave channel which is 106.7 m long, 4.6 m deep, and 3.7 m wide. It can generate periodic and random waves up to 1.5 m high. The east wing contains three wave tanks; a rectangular wave basin 26.5 m long, 18.3 m wide, and 1.5 m deep with a multi-directional wavemaker; and two circular wave basins, one 15.2 m in diameter and 1.5 m deep, and the other, a 3/10 model of the first, 4.6 m in diameter and

0.46 m deep. Both circular wave tanks are capable of generating monochromatic and random spiral waves. The spiral wavemaker for the larger basin consists of sixteen individual paddles arranged in a circle which can operate independently of each other. The wavemaker in the smaller basin is a circular cylinder which oscillates eccentrically about a center axis.

A plan view of the small wave basin is shown in Figure 2.1 which shows the wave crest spiraling out from the wavemaker. A side view of the wavemaker and wave tank is given in Figure 2.2 showing the offset of the wavemaker from the center axis. The circular cylinder is 0.6 m in diameter and height with a gap of 0.64 cm at the bottom of the tank. The spiral wavemaker motion is achieved by the addition of two translational motions in the horizontal plane. The motions in the x-direction and y-direction are independently controlled. If each axis is driven separately by either a sine or cosine function; the summation of the two creates the circular wavemaker motion. In this case, only one wave circles around the basin. To create random waves, a number of predetermined sine and cosine motions with appropriate amplitudes and phases are summed. The radial decay of waves for the small spiral wavemaker is shown in Figure 2.3 in which  $\mu$  is the ratio of the wave amplitude at an arbitrary distance from the wavemaker divided by the wave amplitude at the wavemaker,  $k_o$  is the deep water wave number determined from linear wave theory,  $r$  is the radial distance from the center of rotation, and  $a$  is the wavemaker radius. This plot shows how the wave height decreases as a function of radial distance from the wavemaker.

Elsasser (1989) presented and verified with experimental measurements linear

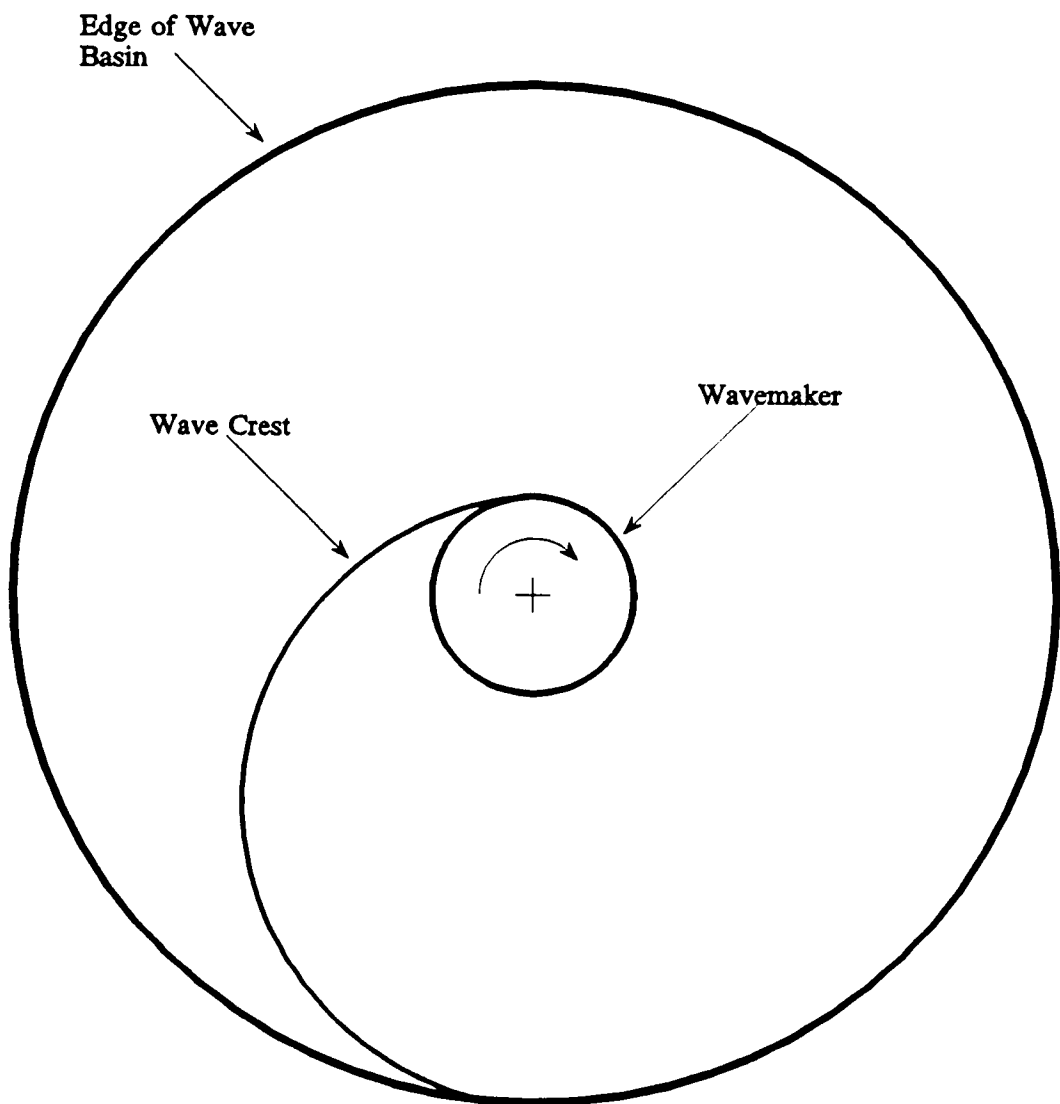


Figure 2.1 Plan view of spiral wavemaker and circular wave basin.

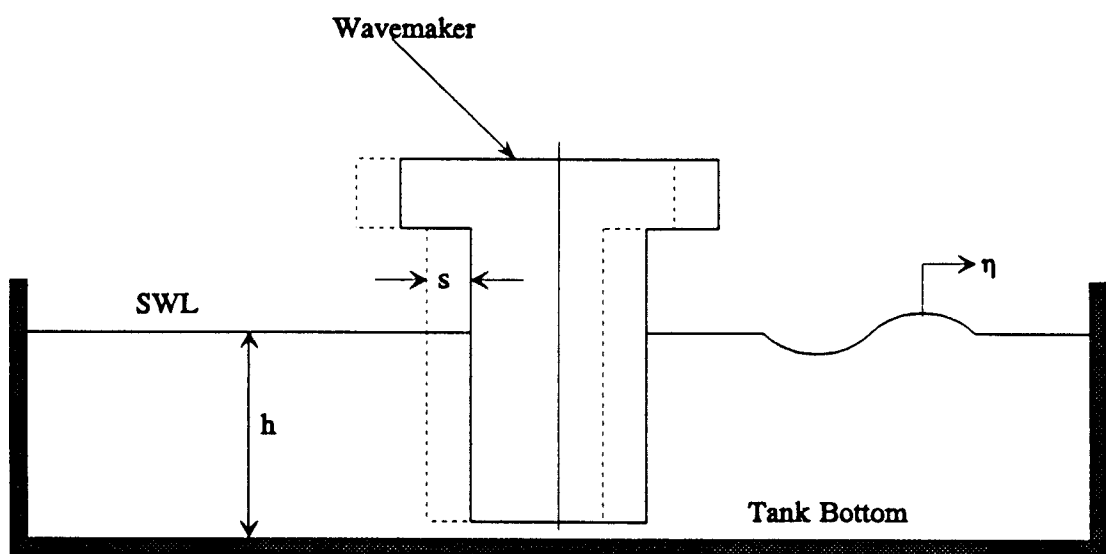


Figure 2.2 Side view of spiral wavemaker and circular wave basin.

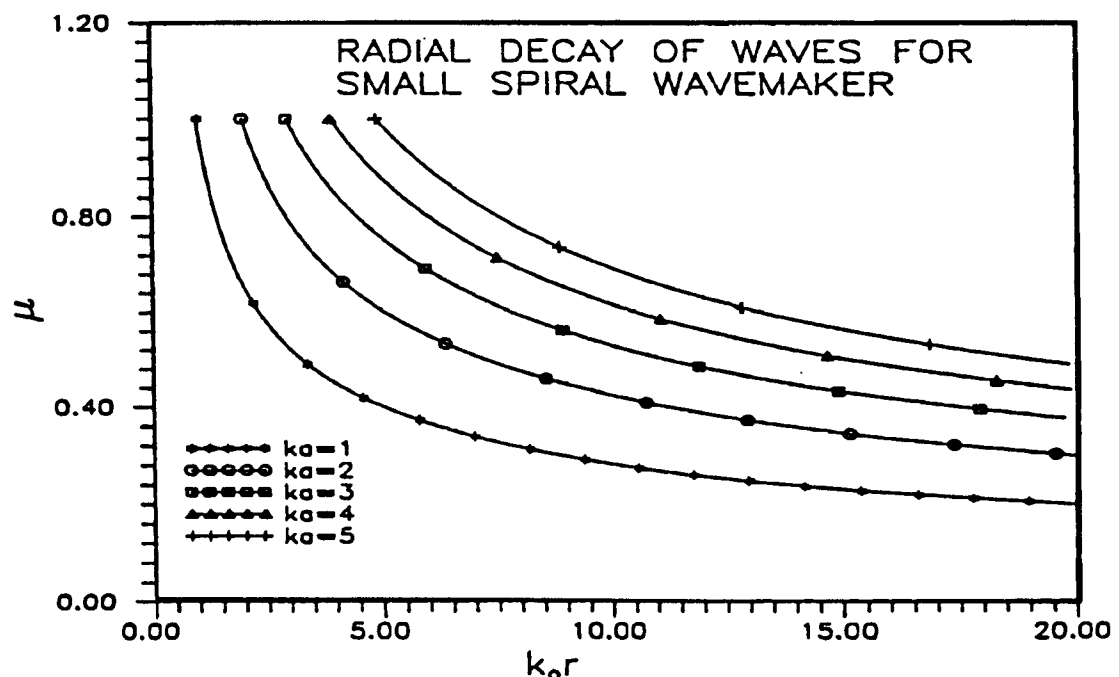


Figure 2.3 Radial decay of waves for small spiral wavemaker (Elsasser, 1989).

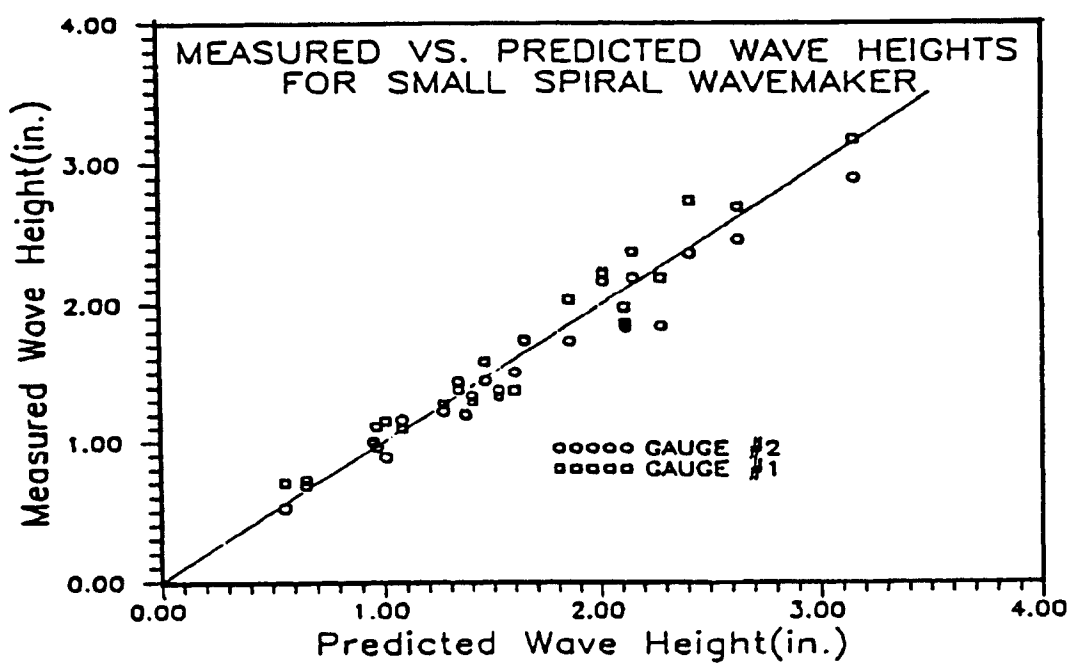


Figure 2.4 Measured vs. predicted wave heights (Elsasser, 1989).

spiral wavemaker theory in the model circular wave basin at the WRL. Wave height data was taken with two resistance gages placed 180° apart and 1.4 m from the center of the wavemaker. The tank circumference was lined with horse hair to absorb the wave energy. Maximum wave heights are limited by either the stroke of the spiral wavemaker or wave breaking limits. The maximum stroke amplitude for the spiral wavemaker is  $\pm 8.9$  cm. Wave breaking can be limited by either deep or shallow water limits. For typical experimental conditions, the deep water condition is more important. As waves travel away from the wavemaker, the wave height decreases. Figure 2.4 shows a plot of predicted and measured wave heights for simple periodic waves. It is clear that there is good agreement between theoretical predictions and actual measurements.

Three different random wave cases were investigated by Elsasser (1989) in the circular wave basin. Figure 2.5 shows the measured and predicted wave forms for a two frequency component wave with good agreement. The second case was a multiple frequency composite wave. Figure 2.6 shows the similarity for the input and measured spectra for an 11 component wave system. The third was based on a theoretical wave spectrum. The stroke amplitude was determined using linear spiral wavemaker theory. The phase spectrum was assumed to be random to develop time series of wavemaker motion. Figure 2.7 and 2.8 show predicted and measured wave spectra for a JONSWAP energy spectrum. From these plots it is apparent that the spiral wavemaker is able to accurately generate random waves.

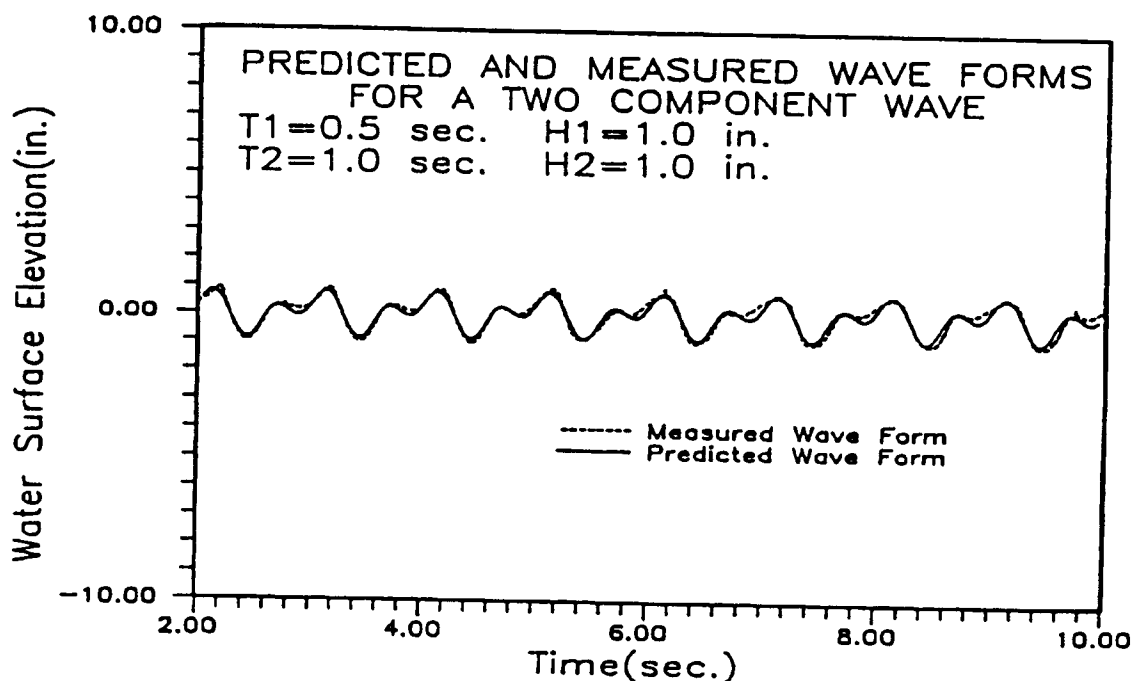


Figure 2.5 Predicted and measured two component wave forms (Elsasser, 1989).

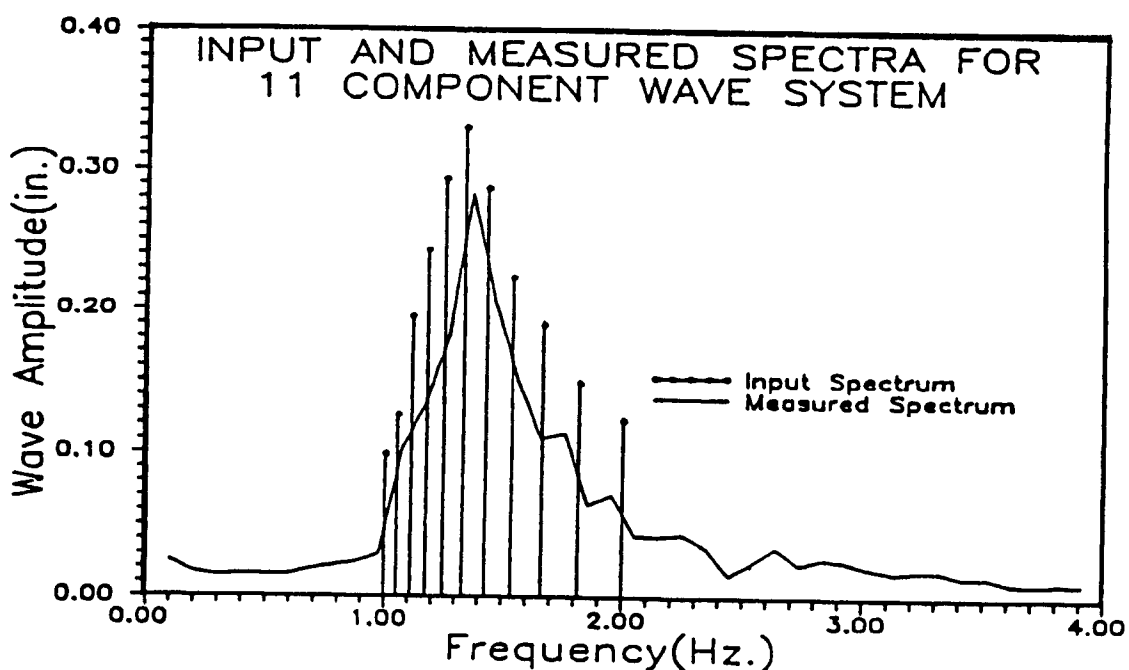


Figure 2.6 Input and measured spectra for 11 component wave system (Elsasser, 1989).

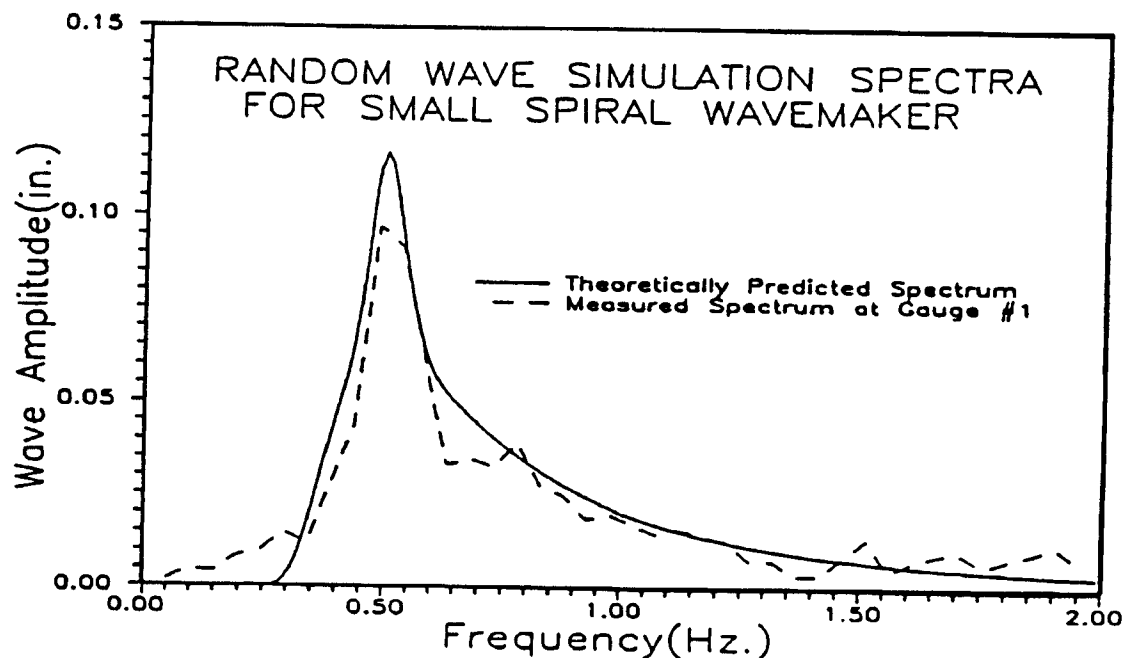


Figure 2.7 Random wave spectra:  $H_s=0.20$  in,  $T_p=2.0$  sec (Elsasser, 1989).

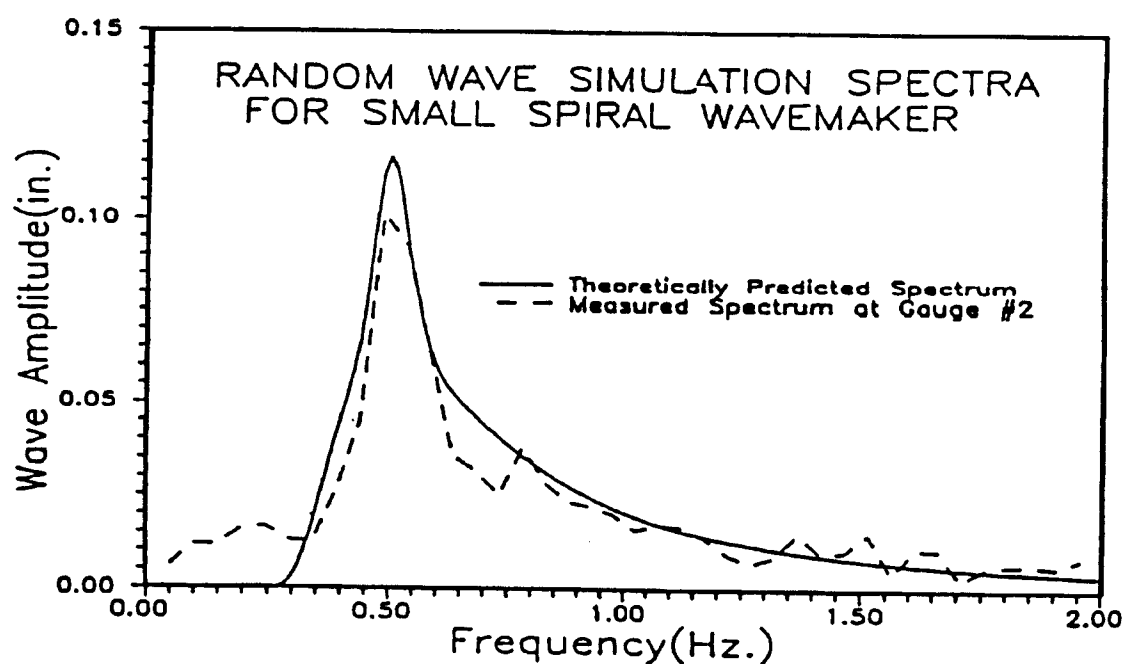


Figure 2.8 Random wave spectra:  $H_s=0.20$  in,  $T_p=2.0$  sec (Elsasser, 1989).

## 2.2 Beach Profile

By constructing a beach in the circular wave basin, nearshore currents can be generated and analyzed. A beach was designed for the circular wave basin which would minimize reflection. It was necessary to minimize reflection in order to eliminate contamination in long term simulations. Svendsen and Jonsson (1976) suggested that to keep reflection negligible,  $h_x L/h \approx 1.0$  where  $h$  is the bottom depth,  $h_x$  is the bottom slope, and  $L$  is the wave length. Dalrymple (1985) showed that by utilizing this relationship for linear long waves, the beach profile for minimum reflection is given by

$$h(x) = \alpha x^2 \quad (2.1)$$

where  $\alpha$  is a constant, and  $x$  is the cross shore distance out from the shoreline. This design shape is a parabola and shown in Figure 2.9. With this beach profile, reflection can be kept to 5% of the incident wave height or 0.25 % of the incident wave energy (Dalrymple, 1985).

It was decided that the parabolic design shape would be the most effective single profile for simulating coastal processes in the circular wave basin. Besides minimizing reflection, this profile also isolates breaking to a narrow region. The exact dimensions of the beach were determined in proportion to the size of the basin. The depth of the beach is 38.1 cm leaving 7.62 cm to the top. The beach extends 152.4 cm radially out from the edge of the basin leaving 47.0 cm to the wavemaker. For these dimensions, the constant coefficient  $\alpha=0.0016 \text{ cm}^{-1}$ . This beach profile is not *representative of typical beach slopes in the field*, nevertheless it suits the purpose of

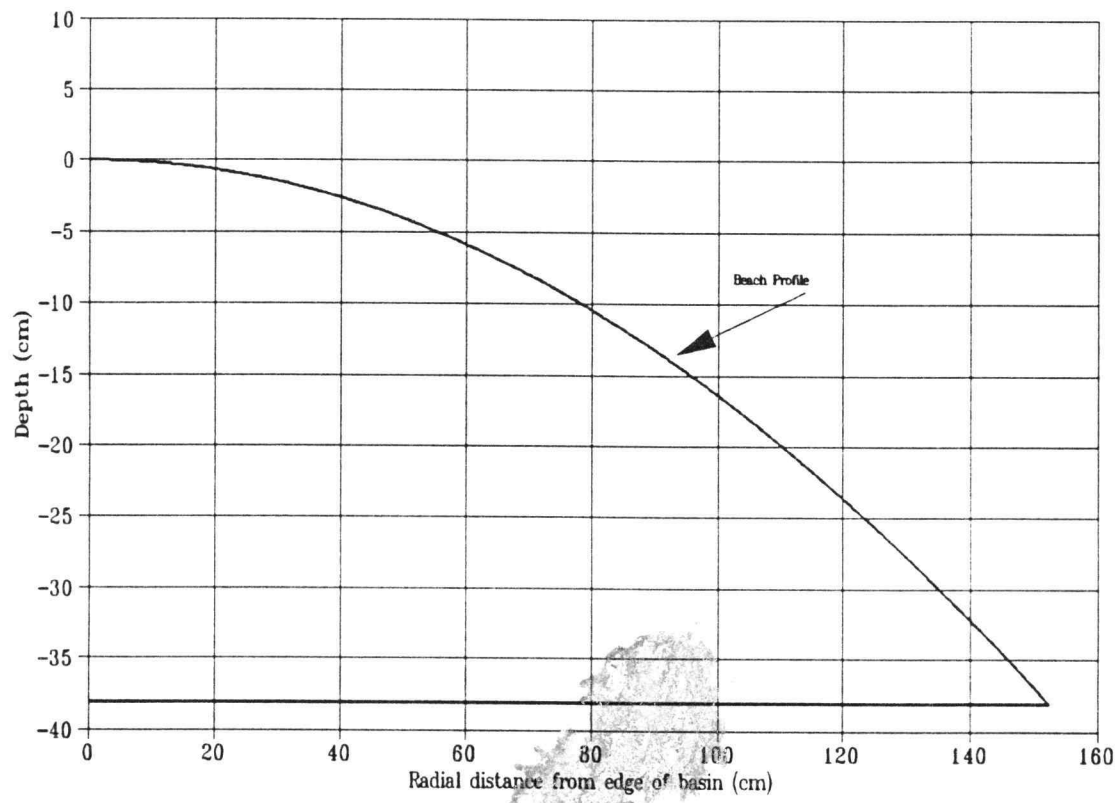


Figure 2.9 Beach profile design.

simulating coastal processes in the circular wave basin.

The profile was constructed from a sand-cement mix. To achieve the design profile, 16 sheet metal templates were fabricated with the profile of the desired beach. The templates were placed in the wave tank dividing it into 16 equal sections. Figure 2.10 shows a view of one template and how the templates were placed in the wave tank. To reduce the required grout volume, each section was filled in with sand and packed down with a tamping block leaving approximately 5.0 cm on the surface for the layer of concrete. The sections were then filled in with concrete and the templates were used as guides to trowel the concrete out smoothly to the design beach profile. The tank was filled with water to allow the concrete to cure while avoiding cracking of the surface. Once the concrete had cured, a sealer was applied to the surface to seal the beach and smooth out the rough spots. The finished beach profile as constructed in the wave tank is shown in Figure 2.11.

### **2.3 Reflection and Circulation**

Initial tests were run in the model circular wave basin upon completion of the beach to evaluate reflection and circulation. Resistance gauges, designed and constructed by Terry Dibble of the WRL, were used to record wave height data. A 3-D acoustic current meter was used to record current measurements in both the radial and tangential directions. Figure 2.12 shows the experimental set-up. The wave gauges and current meters were supported on a beam which was placed directly across the center of the wavemaker. Signal output from both the current meter and wave

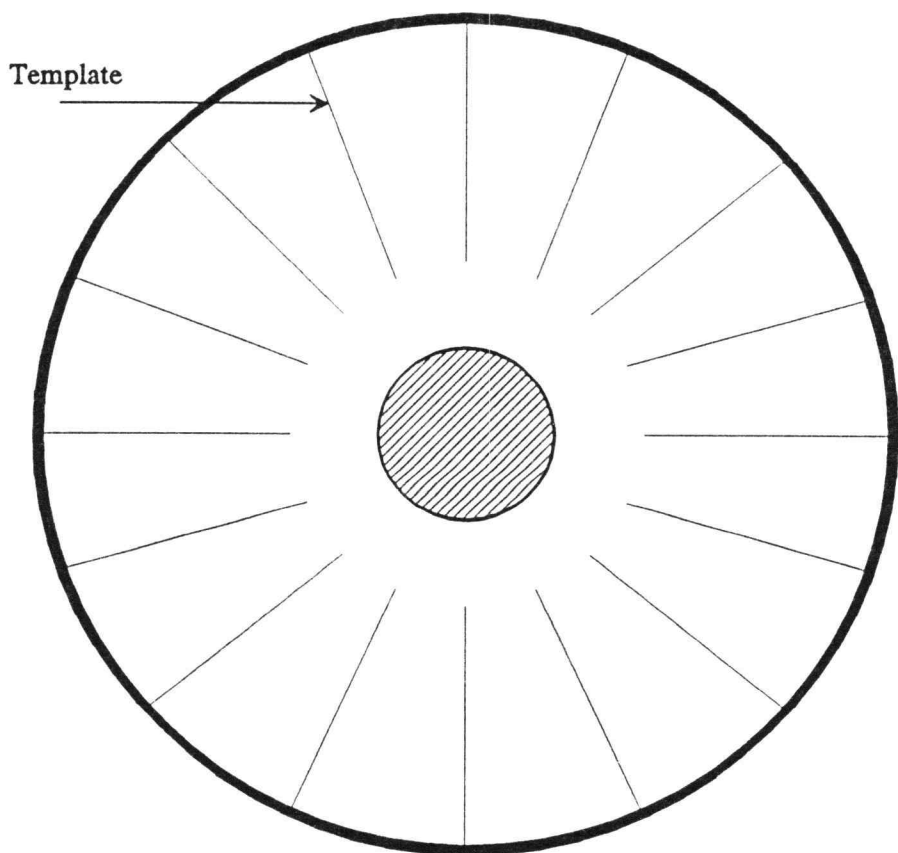
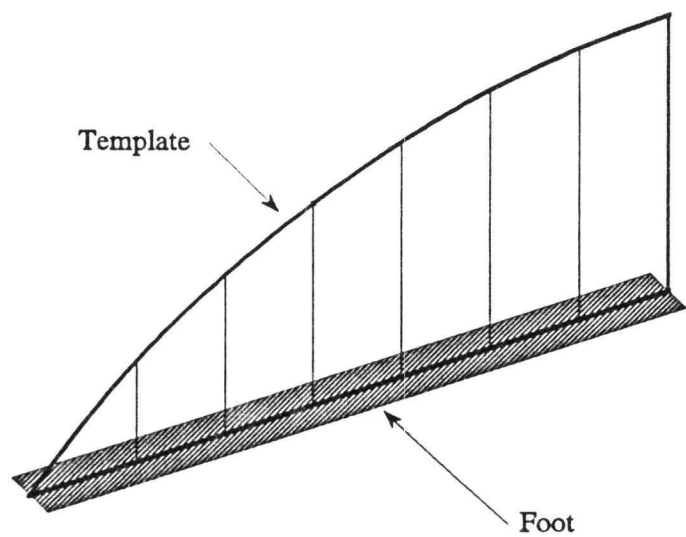


Figure 2.10 Sheet metal templates and placement in wave basin.

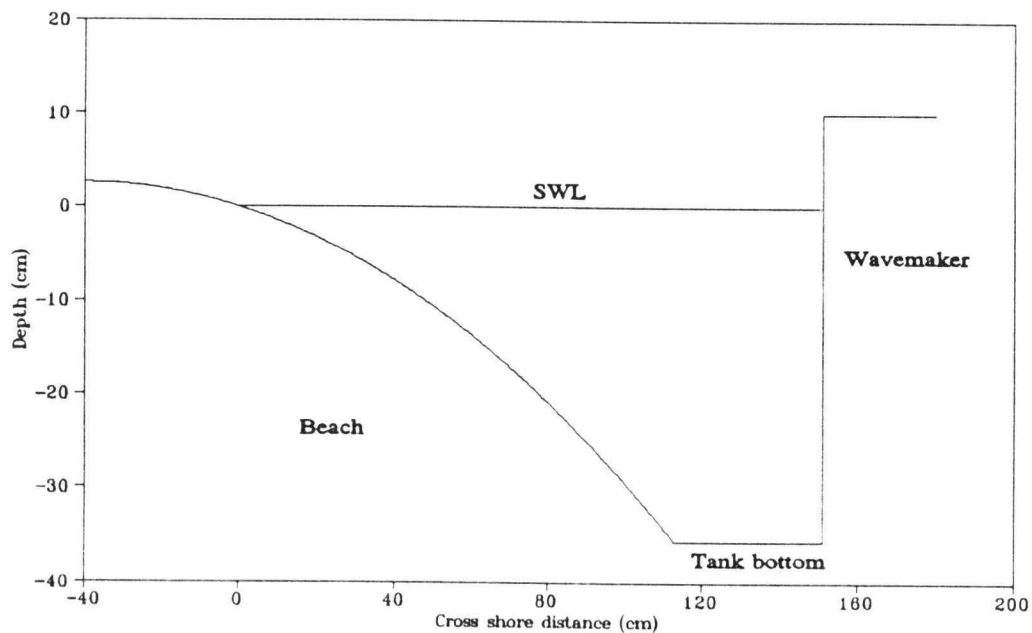


Figure 2.11 Finished beach in wave basin.

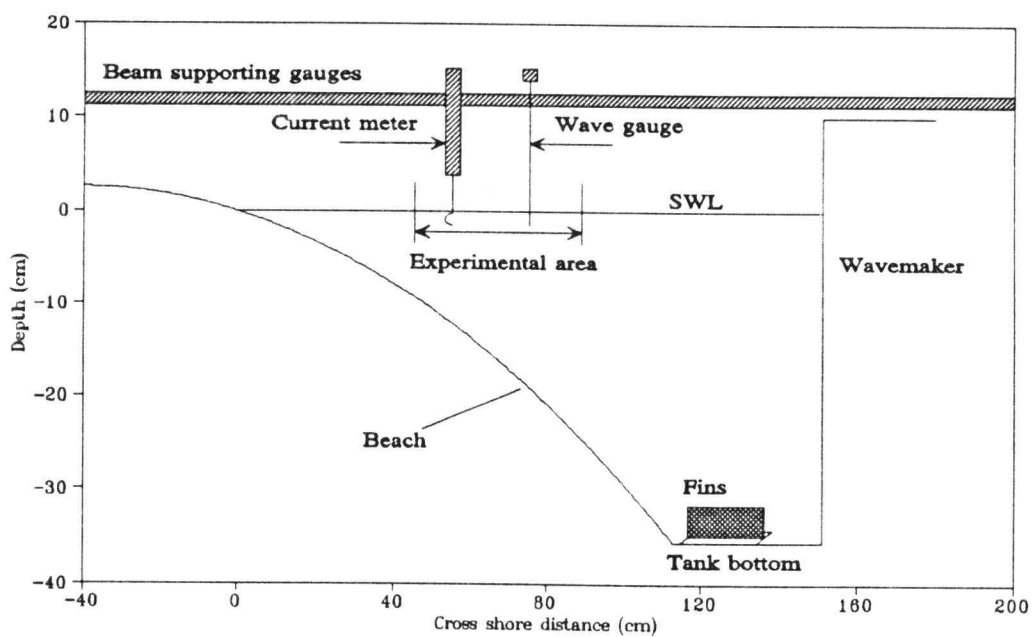


Figure 2.12 Experimental setup.

gauges were connected to filters and a personal computer. Labtech Notebook, a commercial available data acquisition software package was used with the personal computer to record wave height and current data. Labtech Notebook wrote the current and wave profile measurements to ascii files which could be imported into the spreadsheet Quattro Pro to be plotted and analyzed. Tests were performed at a water depth of 35.6 cm.

To measure wave height, two resistance gauges were placed directly in line at radial distances of 97 and 142 cm from the center of the wavemaker. Figures 2.13 to 2.18 show wave height time series sampled at 16 hz for monochromatic, two frequency component, and random waves. For each time series, a group of representative waves were selected to evaluate wave height. For each monochromatic test, wave heights were calculated for approximately 10 waves and averaged. Values for wave height for the two frequency component and 11 frequency component wave were taken from Elsasser (1989). The wave gauges were calibrated at the end of each period of data acquisition. The wave gauges were moved manually in the positive and negative vertical direction by approximately 1.0 cm increments while recording the corresponding change in voltage. The data was then plotted and a calibration coefficient was determined by calculating the slope of a best fit line. A summary of wave profile tests is shown in Table 2.1.

When the spiral waves propagate away from the wavemaker and break on the beach, reflection occurs. A reflected wave then propagates away from the beach back towards the wavemaker. This process continues until a wave envelope is developed

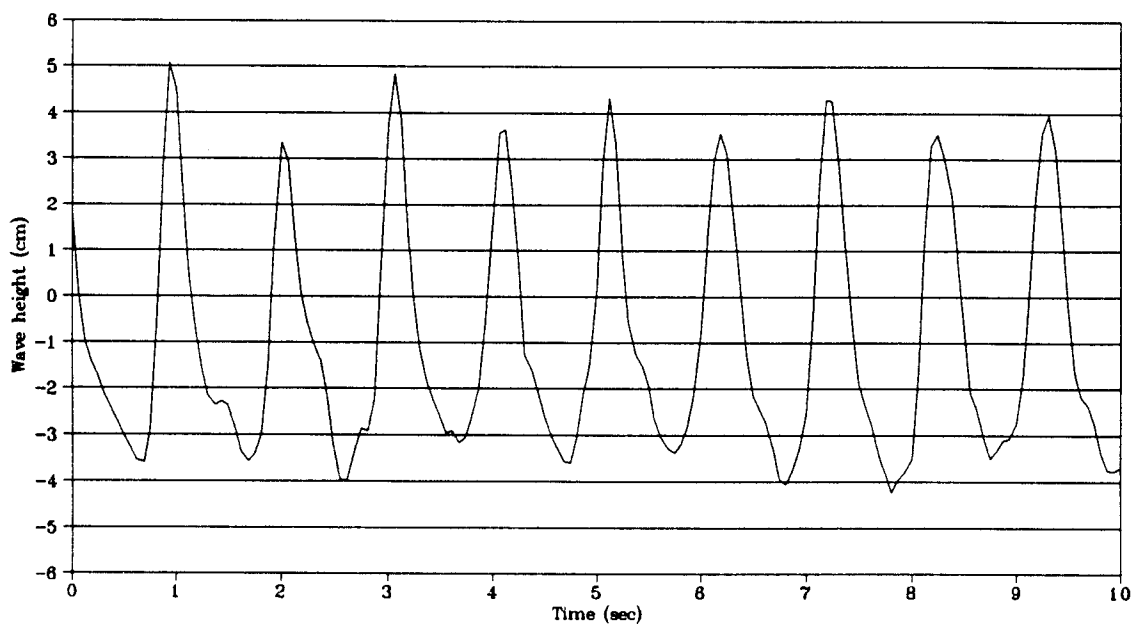


Figure 2.13 Wave profile 142 cm from wavemaker:  $T=1.0$  sec,  $H=7.6$  cm.

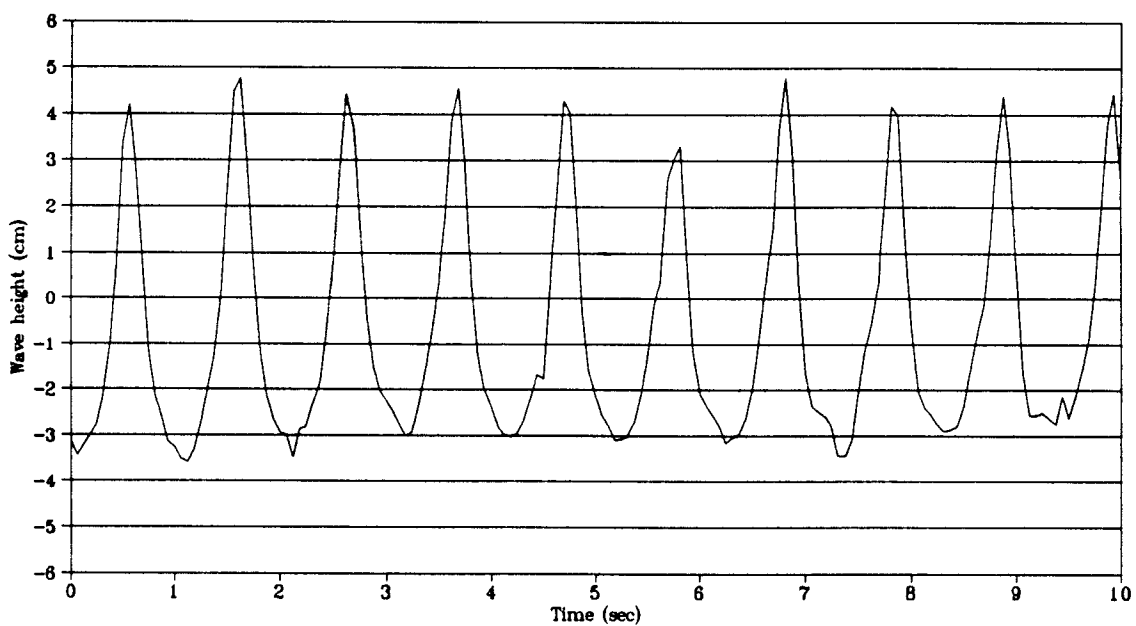


Figure 2.14 Wave profile 97 cm from wavemaker:  $T=1.0$  sec,  $H=7.6$  cm.

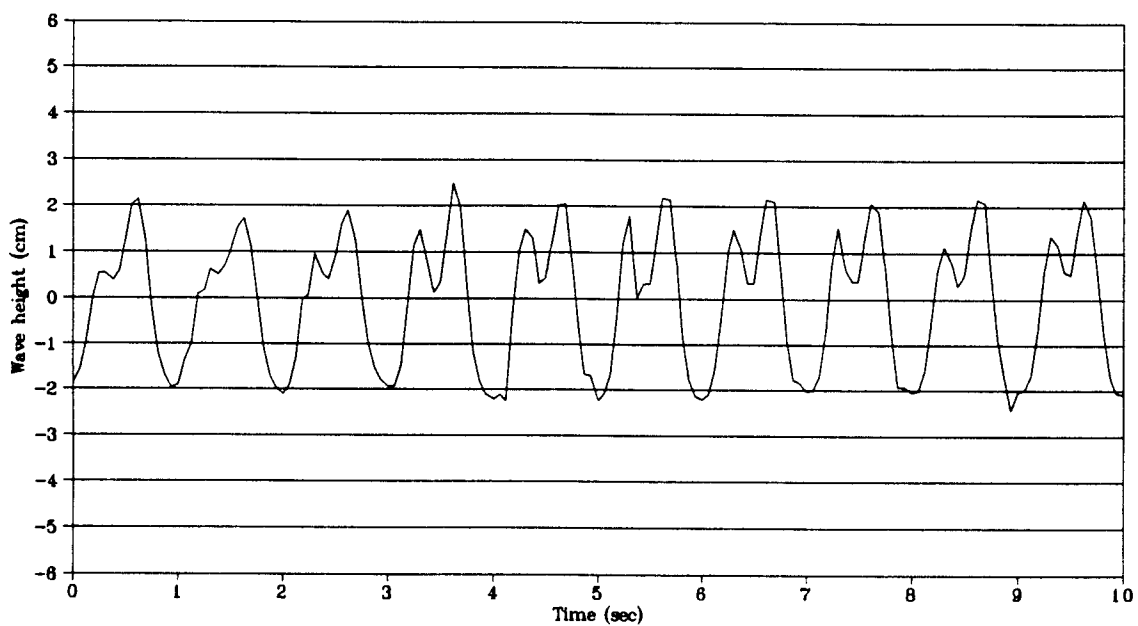


Figure 2.15 Wave profile 142 cm from wavemaker:  $T_1=0.5$  sec,  $T_2=1.0$  sec.

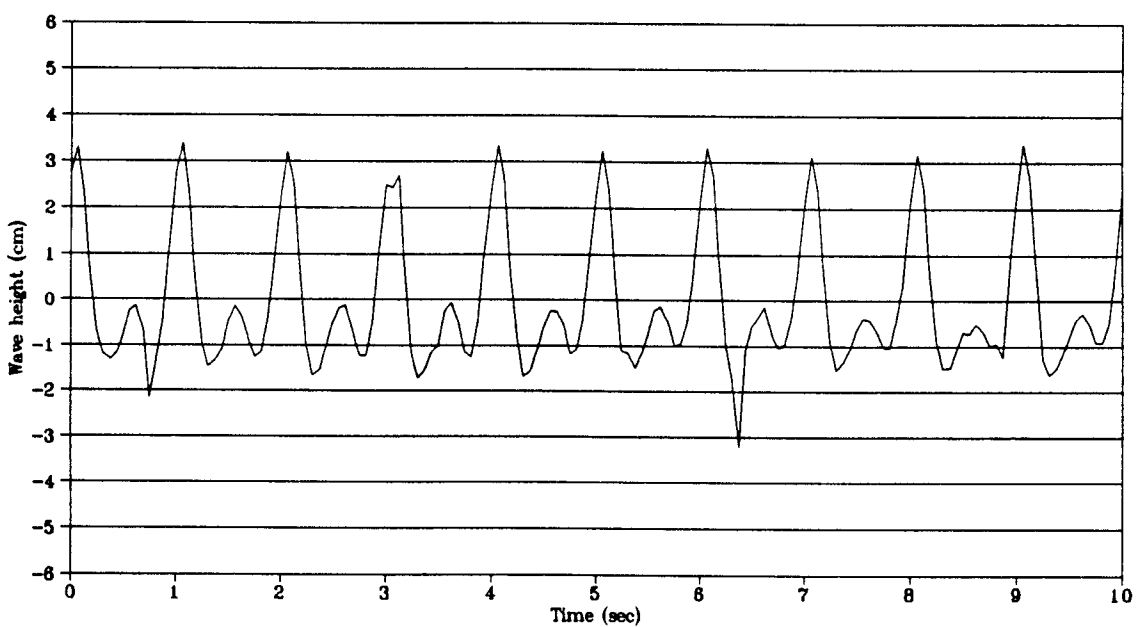


Figure 2.16 Wave profile 97 cm from wavemaker:  $T_1=0.5$  sec,  $T_2=1.0$  sec.

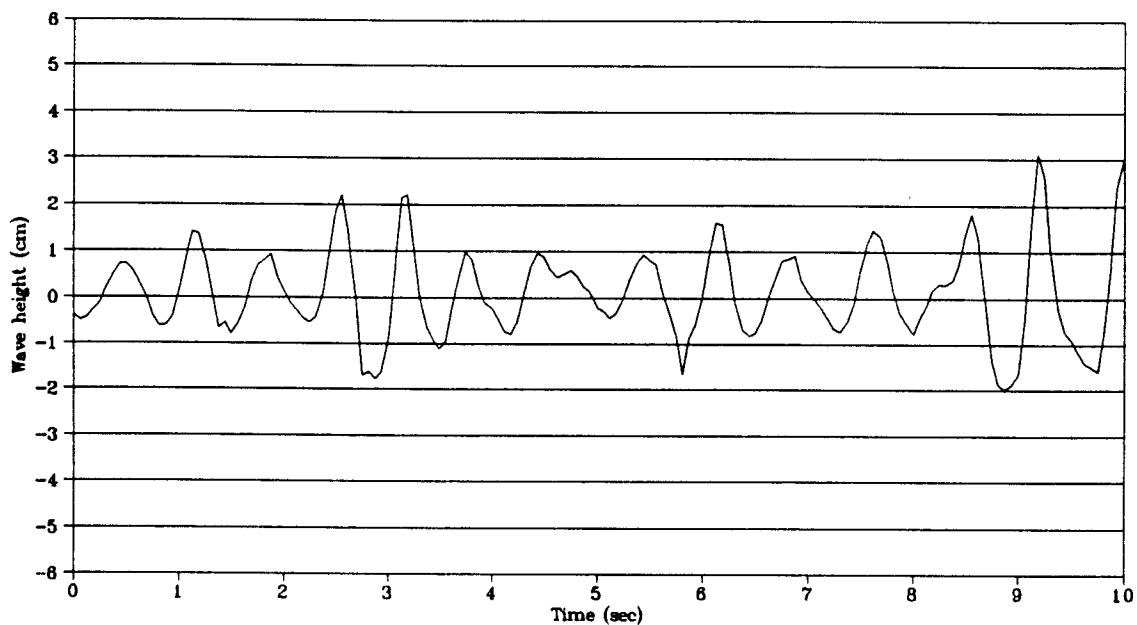


Figure 2.17 Wave profile 142 cm from wavemaker: 11 component wave.

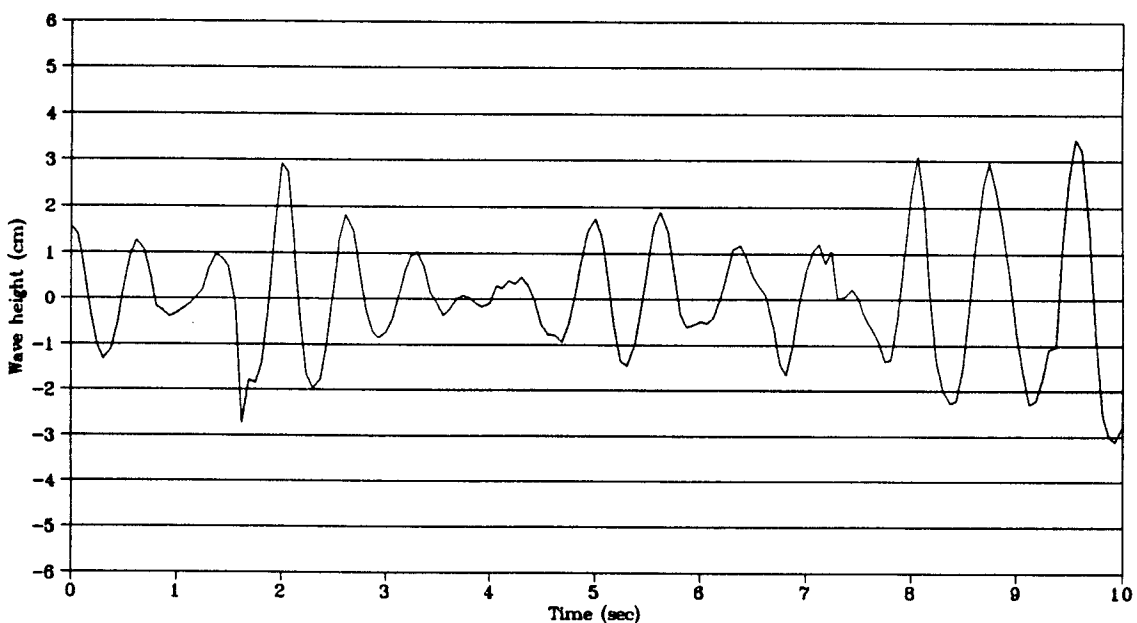


Figure 2.18 Wave profile 97 cm from wavemaker: 11 component wave.

**Table 2.1 Wave Height Data**

<b>Monochromatic Waves</b>	
<b>T(sec)</b>	<b>H(cm)</b>
1.0	7.6
2.0	4.2
<b>Two Frequency Component Wave</b>	
(Elsasser, 1989)	
<b>T1=0.5, T2=1.0</b>	<b>H1=2.54, H2=2.54</b>
<b>Random Waves: 11 component</b>	
(Elsasser, 1989)	
<b>T1=0.50</b>	<b>H1=0.625</b>
<b>T2=0.55</b>	<b>H2=0.757</b>
<b>T3=0.60</b>	<b>H3=0.963</b>
<b>T4=0.65</b>	<b>H4=1.133</b>
<b>T5=0.70</b>	<b>H5=1.458</b>
<b>T6=0.75</b>	<b>H6=1.676</b>
<b>T7=0.80</b>	<b>H7=1.494</b>
<b>T8=0.85</b>	<b>H8=1.234</b>
<b>T9=0.90</b>	<b>H9=0.991</b>
<b>T10=0.95</b>	<b>H10=0.640</b>
<b>T11=1.00</b>	<b>H11=0.503</b>

where the wave system can be considered a superposition of incident and reflected waves. For linear wave theory, the wave profile  $\eta$  and the horizontal water particle velocity  $u$ , are in phase. Let incident waves traveling towards the beach be in the positive direction and reflected waves traveling away from the beach be in the negative direction. This assumes that the wave angles are small. A superposition of incident and reflected components for  $\eta$  and  $u$  can be represented by

$$\eta = a_i \cos(kr - \sigma t) + a_r \cos(kr + \sigma t + \epsilon_r) \quad (2.2)$$

$$u = a_i C \cos(kr - \sigma t) - a_r C \cos(kr + \sigma t + \epsilon_r) \quad (2.3)$$

$$C = \frac{gk}{\sigma} \frac{\cosh k(h+z)}{\cosh(kh)} \quad (2.4)$$

where  $a_i$  and  $a_r$  are the incident and reflected wave amplitudes,  $k$  is the local wave number,  $\sigma$  is the angular wave frequency,  $\epsilon_r$  is the phase angle of the reflected wave, and  $C$  is a constant for each wave condition. Equations 2.2 and 2.3 can be expanded by using trigonometric identities and reduced to the following

$$\eta = A_1 \cos(\sigma t) + B_1 \sin(\sigma t) \quad (2.5)$$

$$u = A_2 \cos(\sigma t) + B_2 \sin(\sigma t) \quad (2.6)$$

where

$$A_1 = a_i \cos(kr) + a_r \cos(kr + \epsilon_r) \quad (2.7)$$

$$B_1 = a_i \sin(kr) - a_r \sin(kr + \epsilon_r) \quad (2.8)$$

$$A_2 = a_i C \cos(kr) - a_r C \cos(kr + \epsilon_r) \quad (2.9)$$

$$B_2 = a_i C \sin(kr) + a_r C \sin(kr + \epsilon_r) \quad (2.10)$$

The reflection coefficient,  $K_r$ , is the ratio of the amplitude of the reflected wave to the amplitude of the incident wave and given by

$$K_r = \frac{a_r}{a_i} \quad (2.11)$$

Equations 2.7-2.10 are a set of four equations with four unknowns. To calculate the value of the reflection coefficient a solution to the four equations was determined to be

$$K_r = \sqrt{\frac{P}{a_i^2} - 1} \quad (2.12)$$

where P is given by

$$P = \frac{1}{2}(A_1^2 + B_1^2) + \frac{1}{2C^2}(A_2^2 + B_2^2) \quad (2.13)$$

and  $a_i$  is measured from the beginning of the time series where the incident wave is not contaminated by the reflected wave. The amplitudes of  $A_1$ ,  $B_1$ ,  $A_2$ , and  $B_2$  are estimated from a Fourier analysis of the time series for the wave profile  $\eta$ , and the horizontal water particle velocity,  $u$ . The wave length for each case was calculated from the linear wave theory dispersion equation.

To conduct the Fourier analysis, a wave gauge and current meter were placed at the same location in the circular wave basin, 137 cm from the center of the

wavemaker. Three separate cases of monochromatic waves were run and time series for  $\eta$  and  $u$  were recorded. The duration of the tests were 256 seconds and the data was sampled at 16 Hz. An FFT was performed for each time series and the real and imaginary coefficients at the dominant wave frequencies were determined. Upon completion of the tests, the reflection coefficient for each wave period was calculated with equation 2.12. For the monochromatic cases,  $T=0.8, 1.0$ , and  $1.2$  seconds, the reflection coefficient  $K_r=0.28, 0.28$ , and  $0.29$  respectively. These calculated values for the reflection coefficient show that the amplitude of the reflected wave is approximately 30% that of the incident wave.

To measure circulation, the 3-D acoustic current meter was placed at various radial locations from 97 to 142 cm from the center of the wavemaker. From initial tangential current meter readings and visual observations, it was apparent that the motion of the wavemaker was producing quite a strong current. The magnitude of this current would increase as time progressed. A strong circulation was also observed throughout the water column close to the wavemaker. This is referred to as "tank spin-up" and is unfavorable because it is not induced by the waves. It is due to the rotation of the wavemaker. To minimize tank spin-up, baffling devices were placed on the tank bottom adjacent to the wavemaker. Eight fins were constructed of perforated sheet metal and positioned in the circular wave basin as shown in Figure 2.12. These were approximately 30 cm wide and 20 cm high. The fins significantly reduced the current close to the wavemaker and were effective in minimizing tank spin-up. Time series for the tangential velocity are shown in Figures 2.19 through

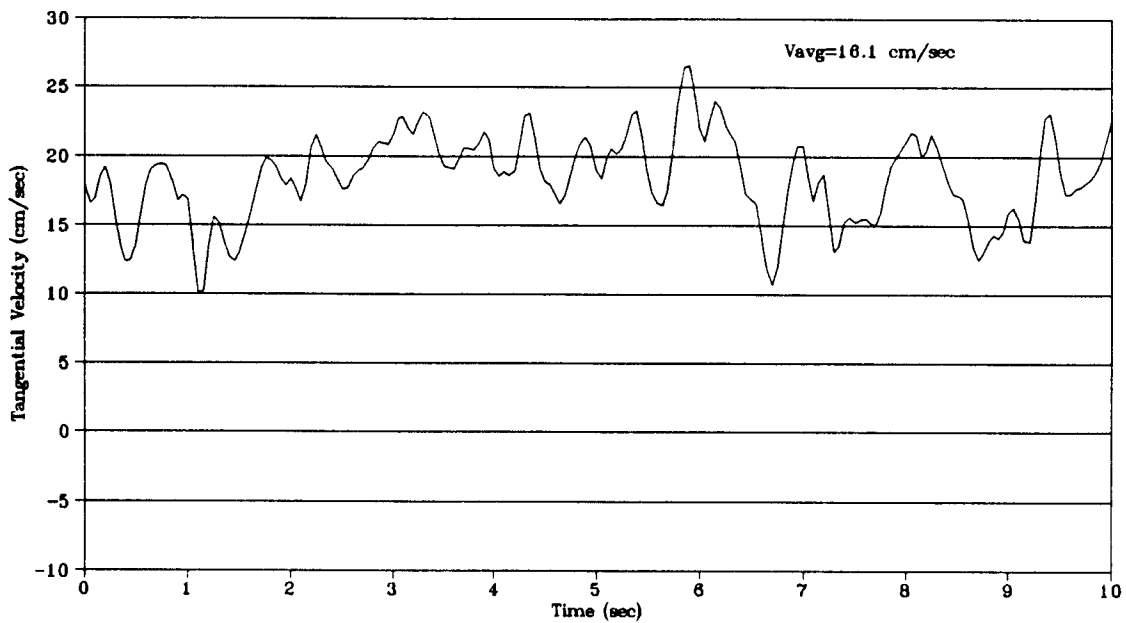


Figure 2.19 Tangential velocity 137 cm from wavemaker: No Fins.

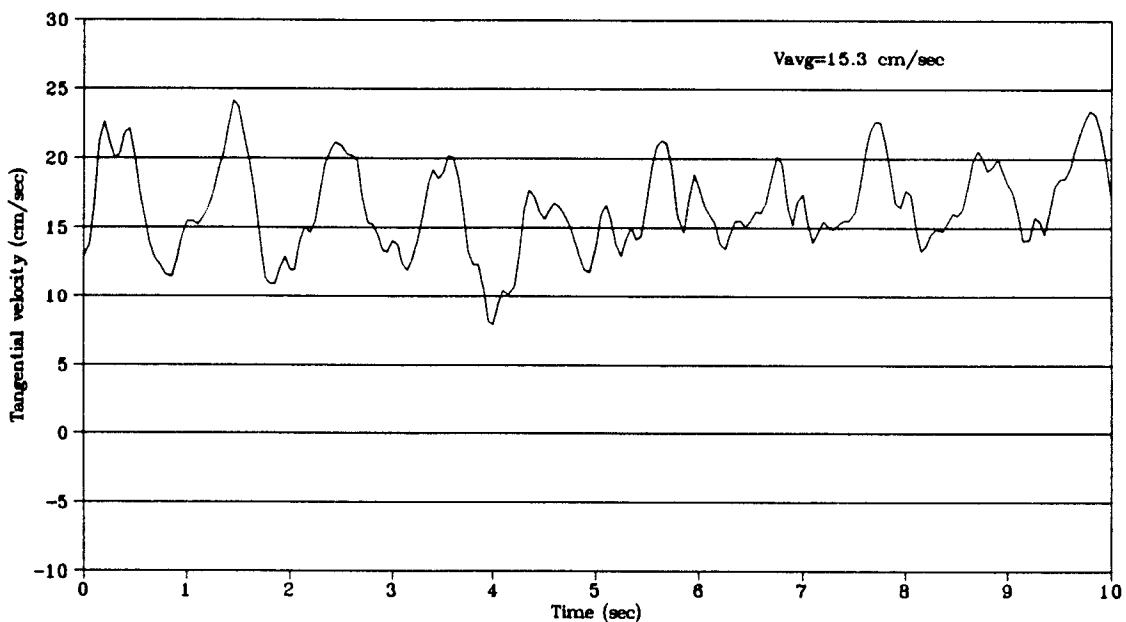


Figure 2.20 Tangential velocity 137 cm from wavemaker: With Fins.

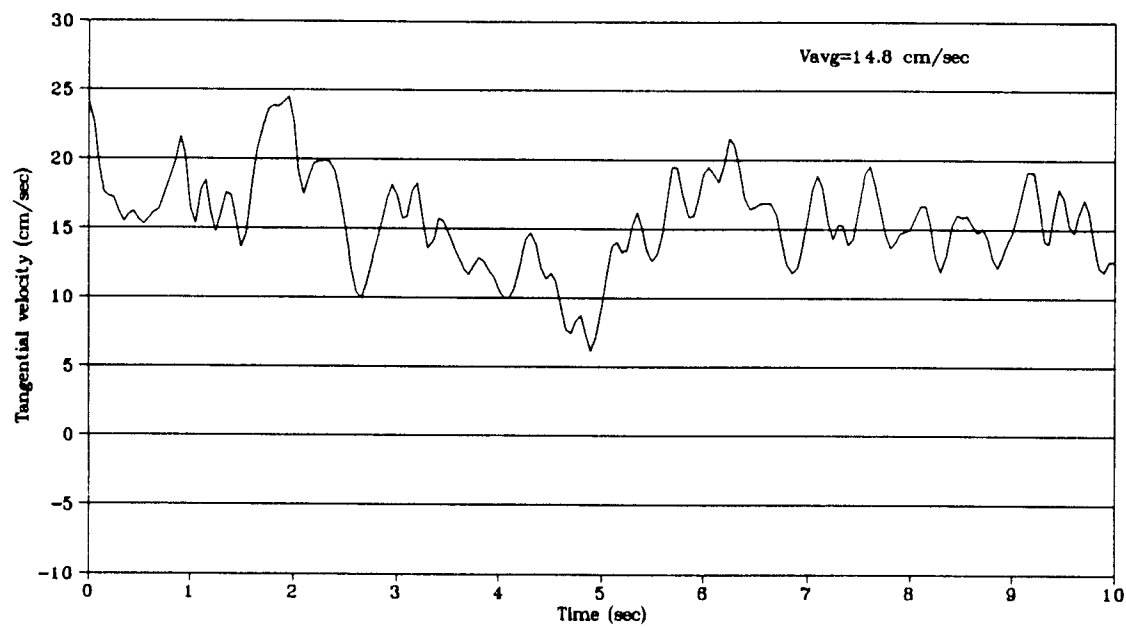


Figure 2.21 Tangential velocity 117 cm from wavemaker: No Fins.

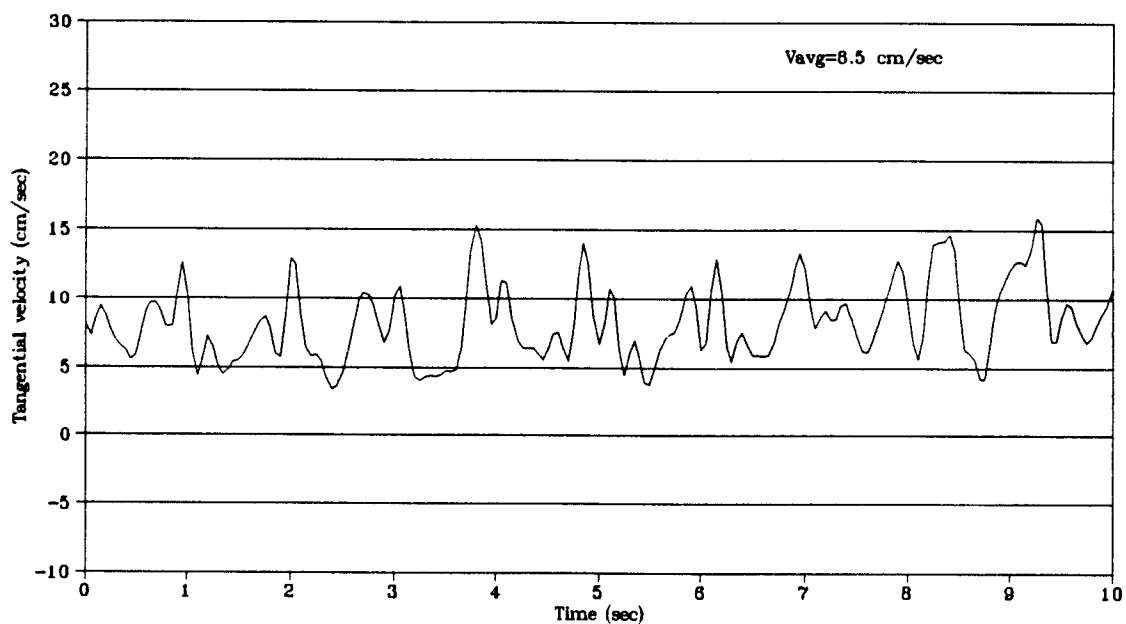


Figure 2.22 Tangential velocity 117 cm from wavemaker: With Fins.

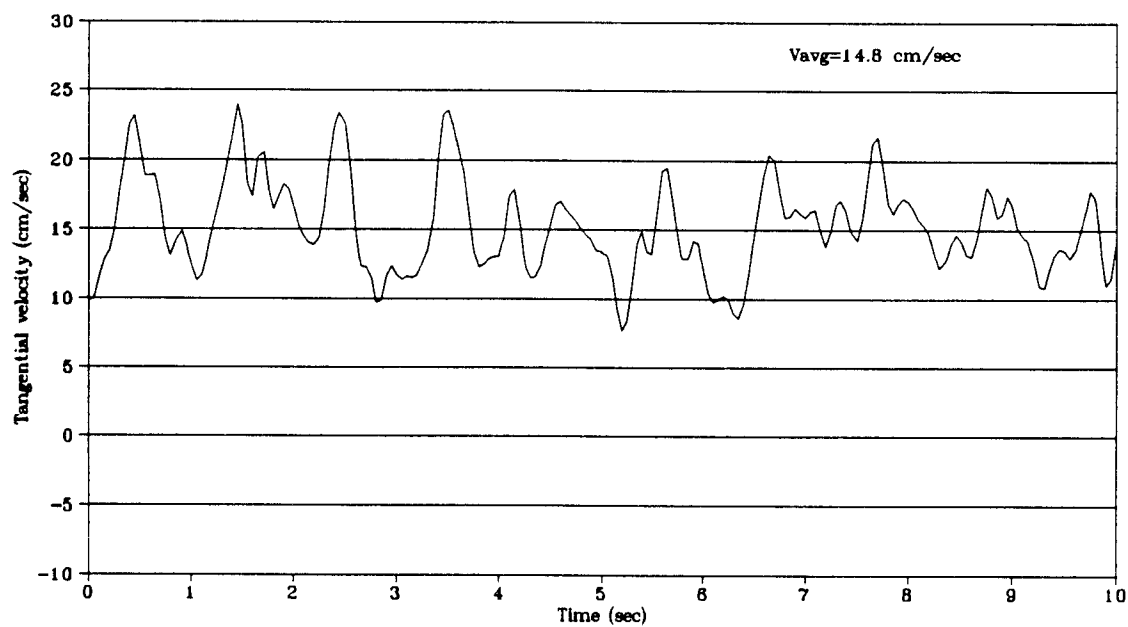


Figure 2.23 Tangential velocity 97 cm from wavemaker: No Fins.

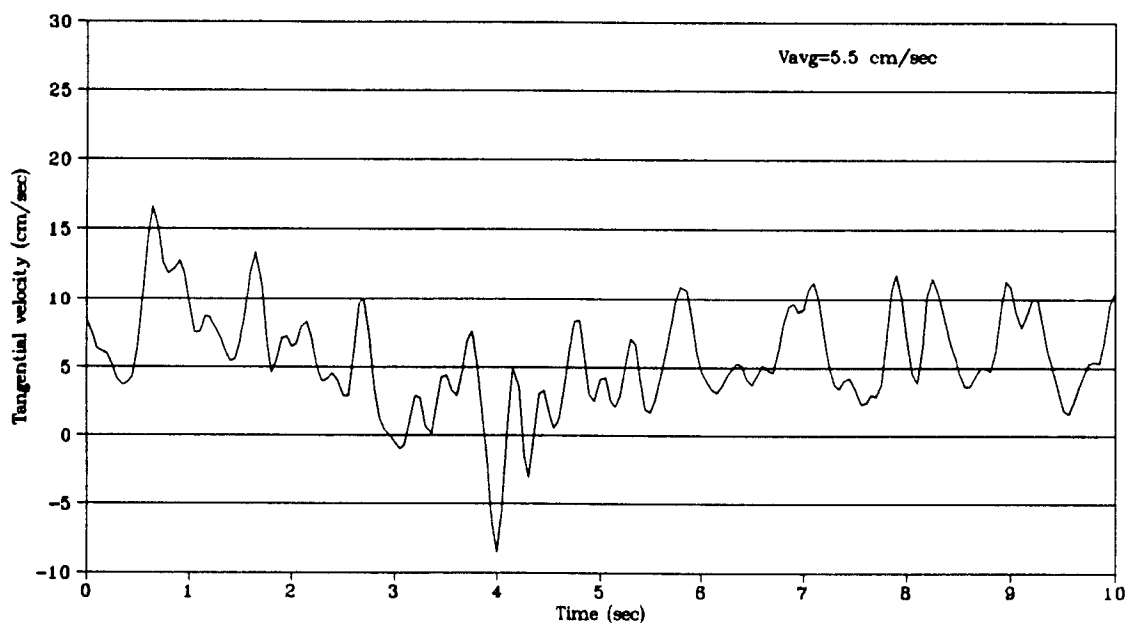


Figure 2.24 Tangential velocity 97 cm from wavemaker: With Fins.

Table 2.2 Current meter data

Waves		Current Meter Location(cm)	Fins	Duration of Run
T(sec)	H(cm)			
1	7.6	142	Yes	205 sec
1	7.6	137	Yes	205 sec
1	7.6	132	Yes	205 sec
1	7.6	127	Yes	205 sec
1	7.6	117	Yes	205 sec
1	7.6	107	Yes	205 sec
1	7.6	97	Yes	205 sec
1	7.6	97	No	205 sec
1	7.6	107	No	205 sec
1	7.6	117	No	205 sec
1	7.6	127	No	205 sec
1	7.6	142	No	205 sec
1	7.6	137	No	205 sec
1	7.6	132	No	205 sec
1	7.6	142	Yes	1024 sec
2	4.2	142	Yes	1024 sec
2	4.2	142	Yes	256 sec
2	4.2	142	Yes	256 sec
2	4.2	142	Yes	256 sec
2	4.2	142	Yes	256 sec
2	4.2	137	Yes	256 sec
2	4.2	132	Yes	256 sec
2	4.2	127	Yes	256 sec
2	4.2	117	Yes	256 sec
2	4.2	107	Yes	256 sec
2	4.2	97	Yes	256 sec

2.24 with and without fins. These figures do, in fact, show that the current has been reduced by the insertion of the fins.

A summary of current meter tests is given in Table 2.2. Mean velocities in both the tangential and radial directions were calculated for all tests. Figure 2.25 shows the mean tangential velocity as a function of radial distance from the center of the wavemaker with and without fins for two monochromatic wave conditions. It is clear from this plot that the fins significantly reduce the tangential current towards the wavemaker. It is also apparent that with increasing radial distance from the wavemaker, the fins have little effect on the tangential current towards the surf zone. While reducing the spin up, the spectra for the tangential current with and without the fins were compared and showed that the fins reduce the amount of energy in the very low frequency. The approximate breakpoint for these tests was at 160 cm from the center of the wavemaker. Thus, the fins seem to have little effect on wave induced currents in the nearshore area in the circular wave basin.

Figure 2.26 shows a comparison between velocities in both the radial and tangential directions with fins for one case of monochromatic waves with  $T=2.0$  sec and  $H=4.2$  cm. The radial velocity is measured on the surface and remains constant out from the wavemaker until the breaker zone where it increases as the waves begin to break. In order to compensate for this average onshore flux of water, a current was observed traveling in the offshore direction along the bottom towards the wavemaker. The tangential velocity steadily increases as a function of radial distance from the wavemaker. Figure 2.27 shows five consecutive tests for mean tangential velocity for

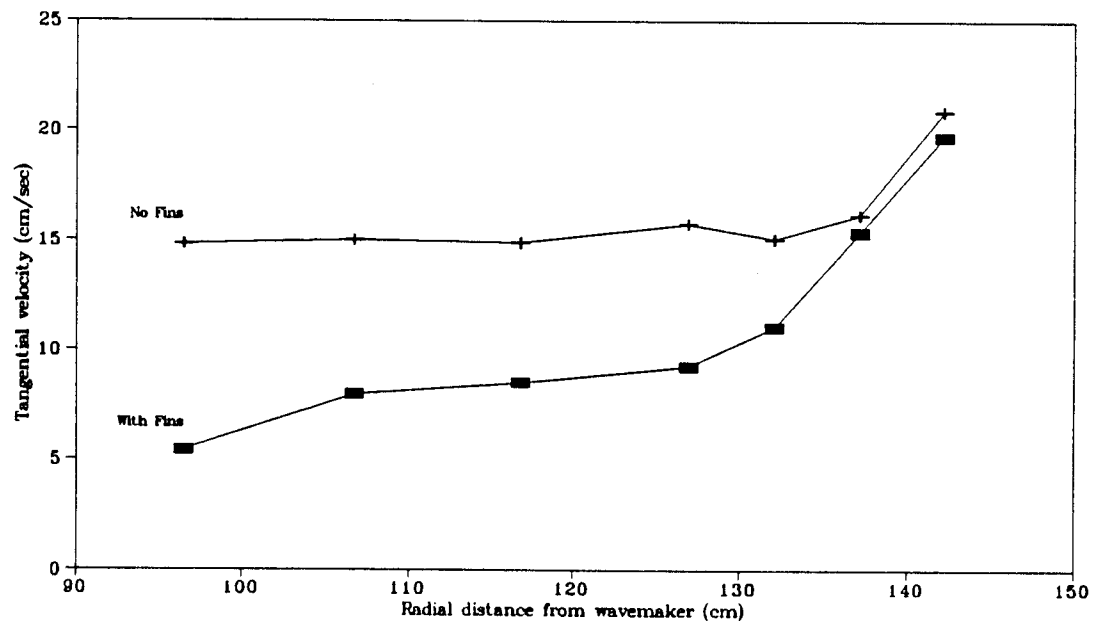


Figure 2.25 Mean tangential velocity with and without fins:  $T=1.0$  sec,  $H=7.6$  cm.

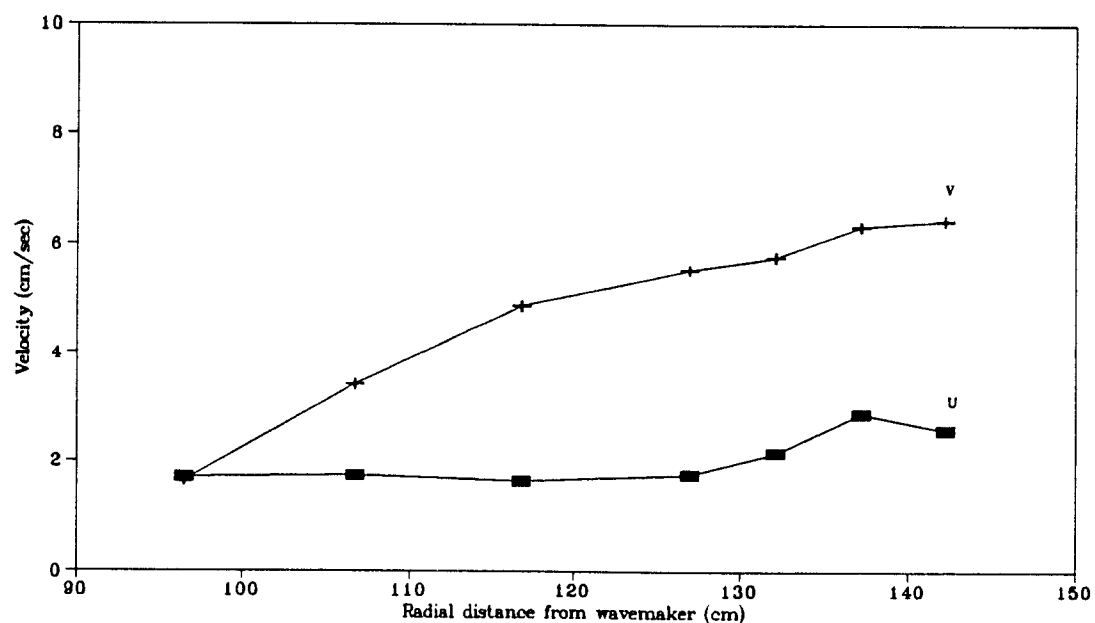


Figure 2.26 Tangential and radial velocity with fins:  $T=2.0$  sec,  $H=4.2$  cm.

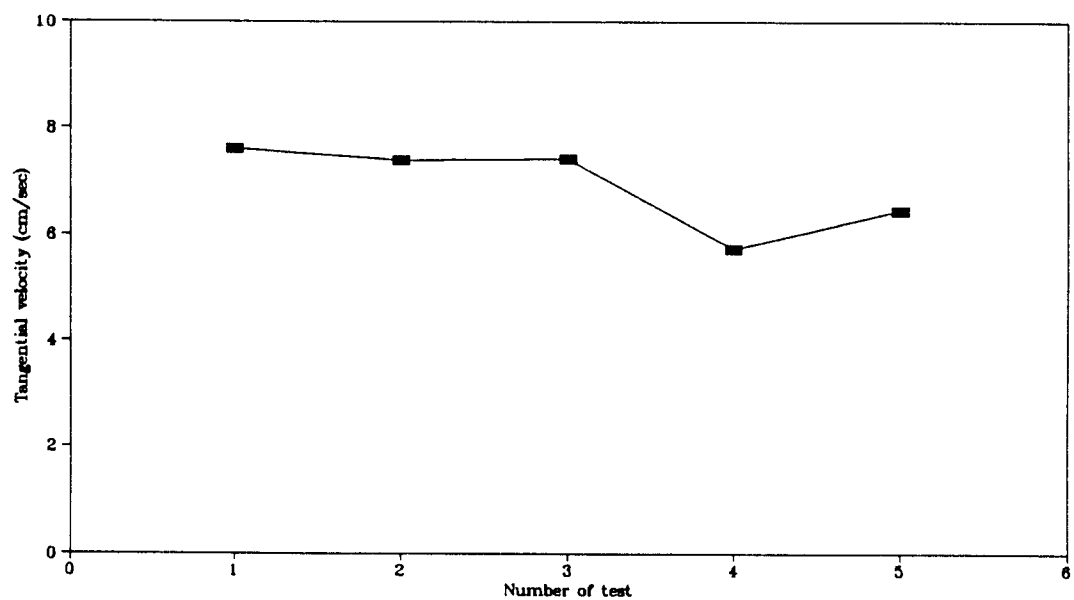


Figure 2.27 Repeatability for mean tangential velocity:  $T=2.0$  sec,  $H=4.2$  cm.

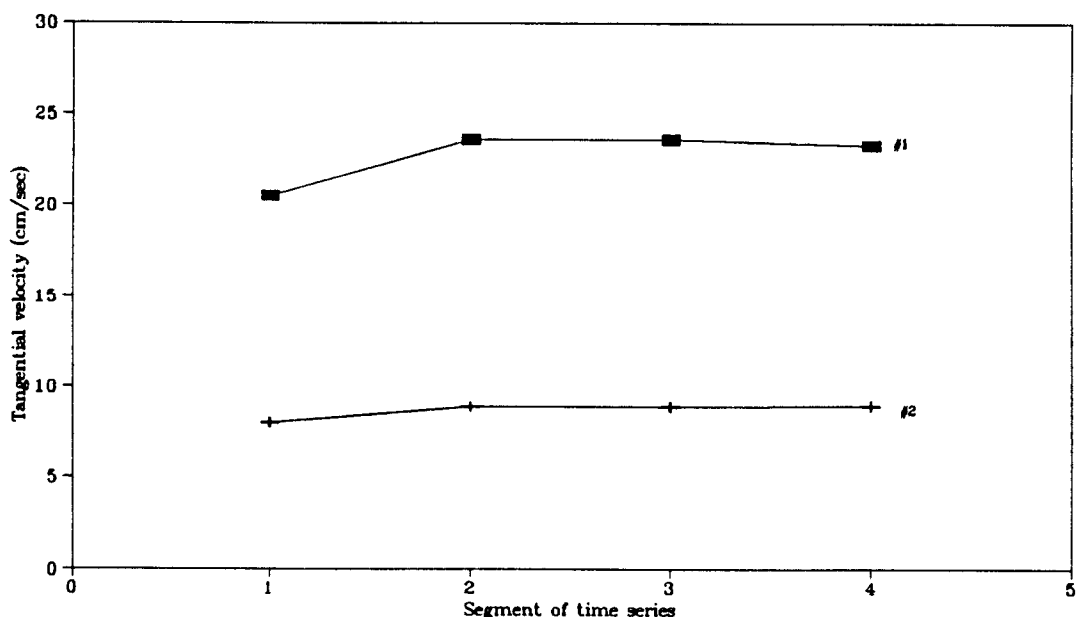


Figure 2.28 Stationarity test for mean tangential velocity with fins:  
 $T=1.0$  sec,  $H=7.6$  cm (#1) and  $T=2.0$  sec,  $H=4.2$  cm (#2).

monochromatic waves with  $T=2.0$  sec and  $H=4.2$  cm. The current measurements were recorded at the same radial location from rest. Each test showed similar results for average tangential velocity. By repeating the same wave conditions, the magnitude of the tangential current generated is relatively constant as a function of radial distance from the wavemaker. In addition to repeatability, two tests were performed for a duration of approximately 1024 sec. Each data file for tangential velocity was then divided into four segments, each 256 sec long. Figure 2.28 shows mean tangential velocity with  $T=1.0$  sec,  $H=7.6$  cm and  $T=2.0$  sec,  $H=4.2$  cm respectively for the four segments in the time series. From this plot the individual segments give similar results and the tests appear to be steady over an extended length of time.

## Chapter 3

### Longshore Currents

#### 3.1 Introduction

An important area of research interest in coastal engineering is nearshore currents. Wave induced currents can cause significant erosion and accretion of sediments along the shoreline. The longshore current is generated by waves breaking at an oblique angle to the shoreline. The resulting current transports sediment and plays a major role in adjusting the overall beach morphology. In the design and construction of coastal structures, it is imperative to have a good understanding of longshore currents in order to evaluate littoral processes.

Plan and profile views of the surf zone are shown in Figure 3.1. The plan view shows  $x_B$  which is the cross shore distance from the shoreline to the breaker line. Outside the breaker line a wave crest is shown approaching the shoreline at an angle of incidence  $\theta$ . This area is referred to as the nearshore. The profile view in Figure 3.1 shows the setup and setdown of the mean water level, MWL, with the existing beach profile in the circular wave basin at the WRL. SWL is the still water level,  $\langle \eta \rangle$  is the wave setup/setdown,  $h$  is the still water depth, and  $d$  is the total water depth ( $h + \langle \eta \rangle$ ). With this beach profile, the spiral wavemaker can create a surf zone area in which waves break on the beach at an oblique angle of incidence. In the circular wave basin a longshore current is produced in the direction of wave angle approach which circulates around the tank. Currently, there is no published literature

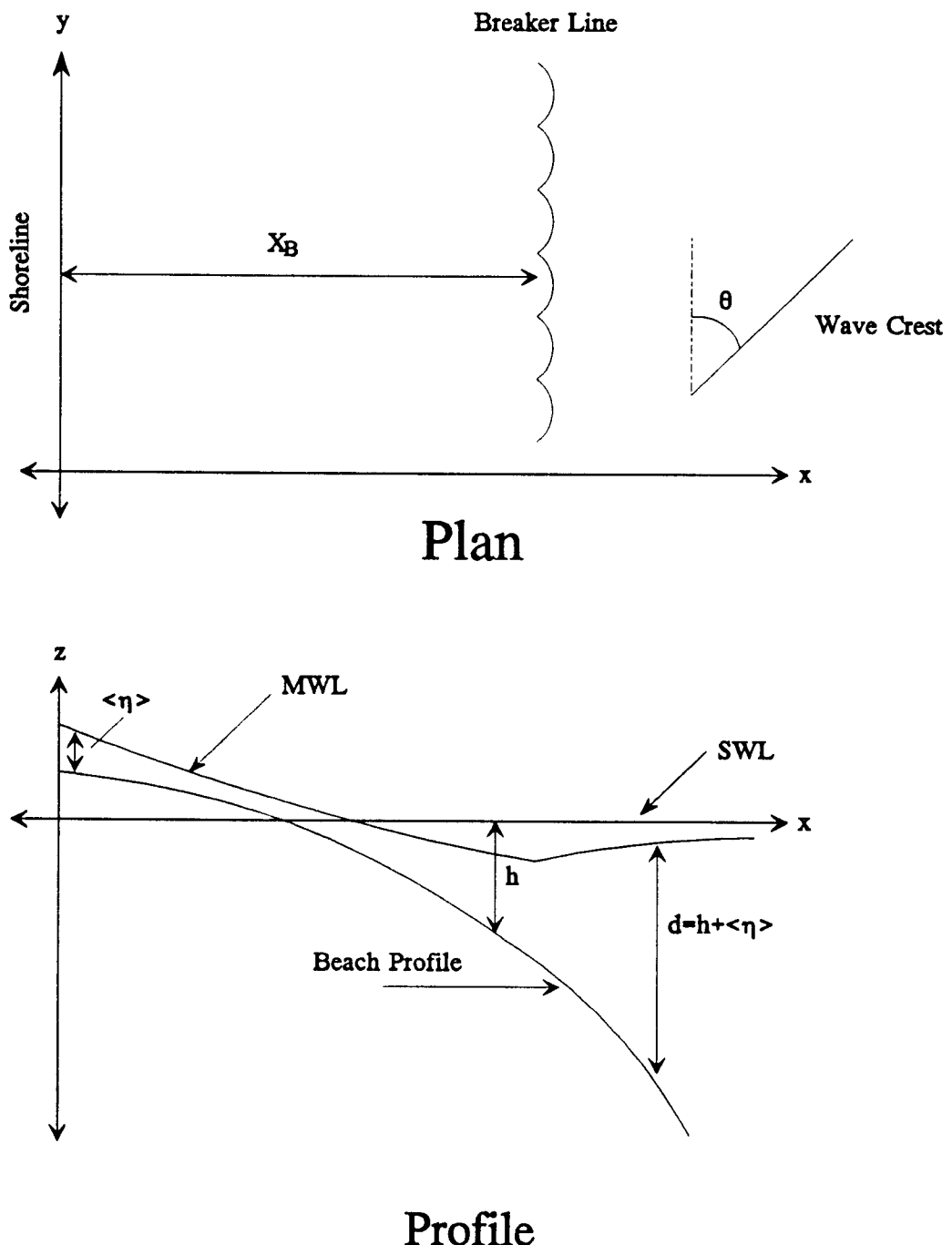


Figure 3.1 Plan and profile view of surf-zone (McDougal and Hudspeth, 1986).

on the generation and prediction of longshore currents in a circular wave basin by a spiral wavemaker.

### 3.2 Longshore Current Model

To determine a general equation of motion for wave induced longshore currents in the surf zone, Longuet-Higgins (1970b) derived a model to include forces due to radiation stress, bottom stress and turbulent mixing. The model shows that the wave driving term, the gradient in the radiation stress, is balanced by both a bottom friction and an eddy viscosity term and given by

$$-\frac{d}{dx}S_{xy} + \tau_{by} + \frac{d}{dx}[\mu_e d \frac{d}{dx} V] = 0 \quad (3.1)$$

where  $S_{xy}$  is the onshore-longshore component of radiation stress;  $\tau_{by}$  is the longshore component of bottom stress;  $\mu_e$  is the eddy viscosity coefficient;  $d$  is the total depth ( $h+\eta$ ) and  $V$  is the depth and time averaged longshore current. Assumptions important in deriving this equation are: steady state process; no longshore gradients; slowly varying depth; no surface stresses; the turbulent transport of momentum is much larger than that of the viscous transport; and an eddy viscosity model (Longuet-Higgins, 1970b). The onshore-cross shore component of the radiation stress,  $S_{xy}$  is given by linear wave theory as

$$S_{xy} = \frac{1}{2}\rho g a^2 n \sin\theta \cos\theta \quad (3.2)$$

where  $\rho$  is the density of water;  $g$  is the acceleration due to gravity;  $a$  is the wave

amplitude; and  $\theta$  is the angle of incidence of the wave. Linear wave theory gives  $n$  as

$$n = \frac{1+2kh}{2\sinh 2kh} \quad (3.3)$$

where  $k$  is the local wave number, and  $h$  is the still water depth. Shallow water assumptions and Snell's law for refraction are used to estimate  $S_{xy}$  inside the surf zone. Outside the surf zone, the cross shore gradient of the radiation stress is taken to be zero (McDougal and Hudspeth, 1988). The gradient in the cross shore of  $S_{xy}$  is given as

$$\frac{d}{dx} S_{xy} = \begin{cases} -\frac{5}{32} \rho g \kappa^2 \sin 2\theta_B d \left( \frac{d}{d_B} \right) \frac{d}{dx}(d) & ; x < x_B \\ 0 & ; x > x_B \end{cases} \quad (3.4)$$

where  $\kappa$  is the breaker index; and the subscript B refers to values at the breaker line.

A shallow water, linear approximation to the bottom shear stress in the surf zone is given by Liu and Dalrymple (1978) as

$$\tau_{by} = -\frac{C_f}{\pi} \kappa \rho \sqrt{gd} V \quad (3.5)$$

where  $C_f$  is the bottom friction coefficient on the order of 0.01. An eddy viscosity coefficient model is often used which scales the eddy size to the total depth offshore (McDougal and Hudspeth, 1986)

$$\mu_e = N \rho d \sqrt{gd} \quad (3.6)$$

where  $N$  is a numerical constant.

A numerical model was developed by the US Army Corps of Engineers to predict the cross shore structure of the longshore current (Kraus and Larson, 1991). The governing momentum equation used is similar to equation 3.1, however it includes convection, nonlinear friction, and a wind driving term. A finite difference formulation was used to solve for the longshore current. Kraus and Larson (1991) assumed two boundary conditions: 1) no longshore current far offshore and 2) a finite value for the longshore current at the most shoreward point neglecting mixing. The second boundary condition is different than most typical boundary conditions in solving the momentum equation where the longshore current is assumed to go to zero at the shoreline. Field observations usually show a longshore current in the swash zone. This new representation of the shoreward boundary condition will hopefully better predict the magnitude of the longshore current in shallow water close to the shoreline.

The numerical model, called NMLONG (Kraus and Larson, 1991) can be run on a desktop personal computer. The user enters the wave conditions, i.e. wave period, wave height, angle of incidence, and wind speed and direction. A beach profile is also entered which should extend approximately one surf zone width past the breaker line. A longshore current profile for a plane beach profile and the convex profile in the circular wave basin are shown in Figures 3.2 and 3.3. Monochromatic waves were used in the calculations where  $T=1.0$  sec,  $H=7.6$  cm, and  $\theta=4^\circ$ . The coefficient of friction used in these calculations was 0.01. Both cases show zero longshore current offshore as expected. For the convex case, the longshore current reaches a maximum value at approximately 50 cm from the edge of the basin. For the

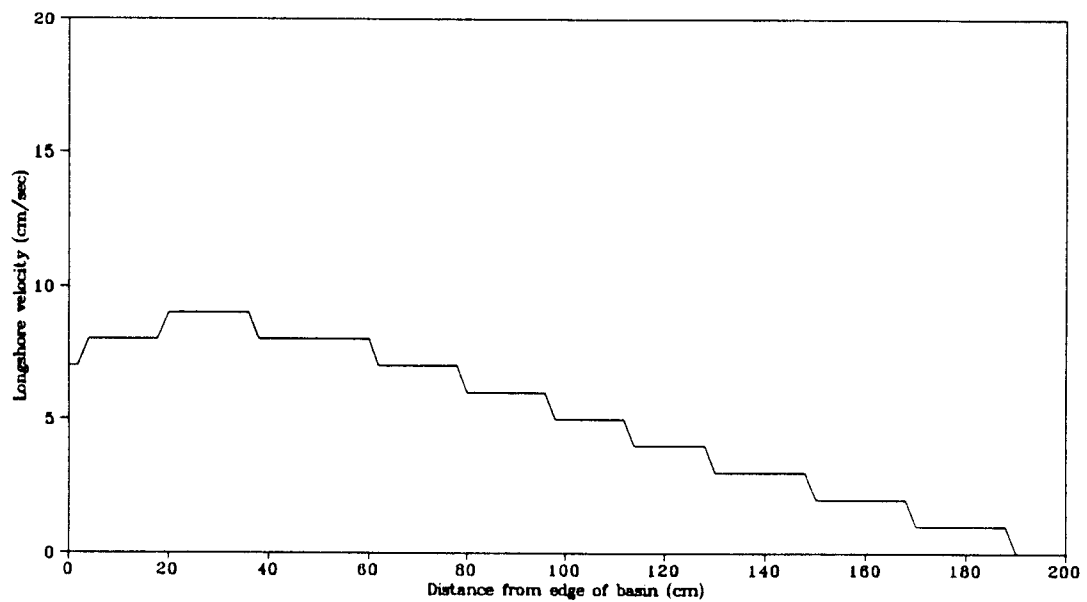


Figure 3.2 Longshore current profile for a plane beach calculated with NMLONG.

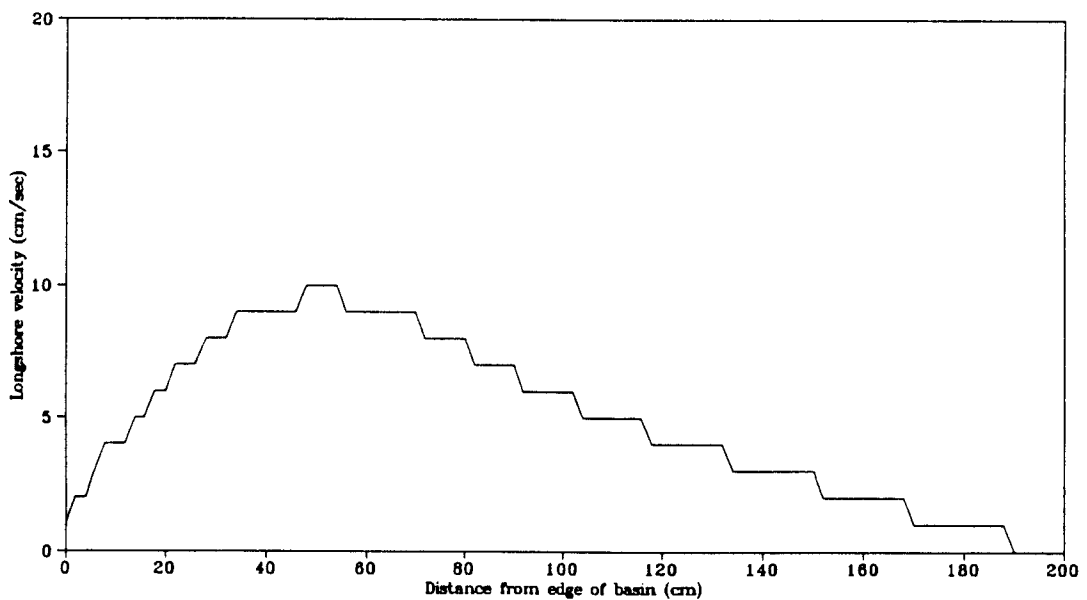


Figure 3.3 Longshore current profile for a convex beach calculated with NMLONG.

plane beach the longshore current reaches a maximum at approximately 30 cm from the edge of the basin. The SWL for the convex and plane beach profiles is at 40 cm, and 10 cm respectively from the edge of the basin. In each case the longshore current reaches a maximum approximately 10 to 20 cm offshore from the shoreline. For the convex case, the breaker line was observed to be 25 to 30 cm from the shoreline. The numerical model predicts a local maximum in the longshore current just inside the breaker line for the convex beach profile.

### 3.3 Longshore Current Experiments

The first phase of data collection to measure longshore currents utilized the acoustic 3-D current meter as discussed in Chapter 2. Velocities were recorded in the radial and tangential directions. The current meter was attached at various locations to a beam spanning the wave basin. It was necessary to keep the current meter completely submerged in order to acquire accurate data. This was a problem as the current meter was placed closer and closer to the shoreline. Inside the breaker line, the shallow water depths made it impossible for the current meter to work effectively. With the basin water depth at 35.6 cm, the distance from the edge of the circular wave basin to the SWL was 40 cm. At this water depth, the experimental area was between 47 and 92 cm from the shoreline. Closer to the shoreline, less than 47 cm from the edge of the water, the current meter would not remain submerged due to breaking waves. To measure currents inside the breaker zone, it was necessary to develop an alternative measurement technique.

To determine the magnitude of the currents inside the surf zone, the motion of a buoyant object in the nearshore was tracked with a video camera. A video image processing system was recently acquired and is currently being installed at the WRL. The system has the capability to capture a field of view and digitize each frame into pixels using an image processor. A software package was written by Andrew Jansky, to track an object in the field of view. To track the object, it is necessary to film the process with a video camera and send the pictures to the image processor. The image processor then digitizes each picture into pixels and assigns to each pixel on the screen a shade of gray between black and white. To achieve the greatest contrast between the object to be tracked and the background, it is necessary to have either black on white or white on black. Because breaking waves and reflected light show up as white on the screen, a white background and a black tracking object were selected to produce the best resolution. Therefore, the beach in the circular wave basin was painted white and a black ball with a slight positive buoyancy was used as the object to be tracked.

To view the entire model circular wave basin, the video camera was placed directly overhead as shown in Figure 3.4. Two pieces of aluminum tubing were welded together at 60 degree angles to a base plate by Chuck Swensen at the OSU machine shop. A manual pan and tilt camera attachment was bolted to the base plate. The aluminum tubing frame was then bolted to the wall with hinges. A cable was attached to the base plate, fed through two pulleys on the ceiling, and connected to a winch bolted to the wall next to the wave basin. With this setup it was possible to raise and lower the video camera to various heights to accommodate different views.

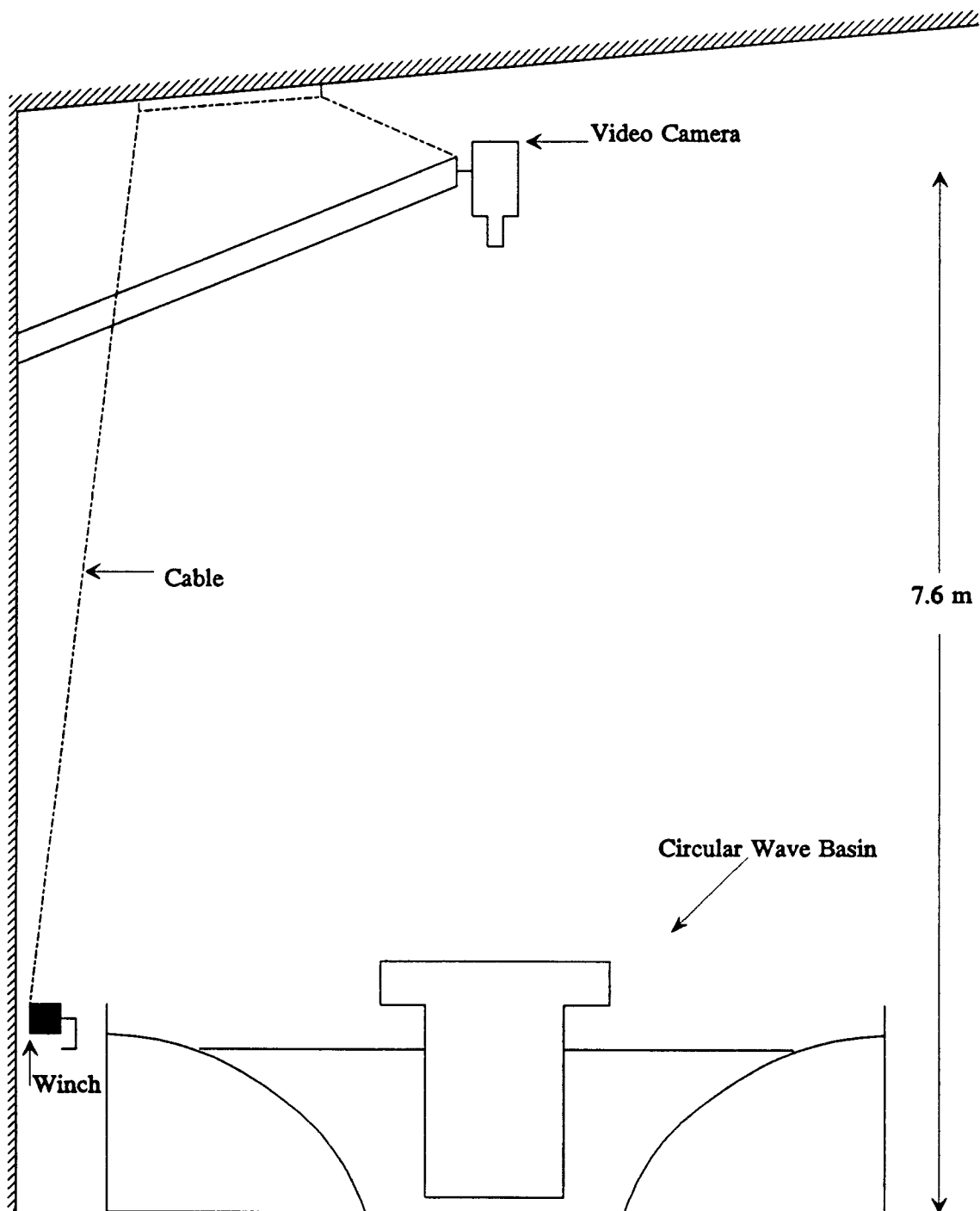


Figure 3.4 Experimental setup with video camera.

The camera was placed directly over the center of the basin perpendicular to the center axis of the wavemaker. As a result of this camera alignment it was not necessary to rectify the image.

Longshore currents for three different monochromatic and two random wave conditions were measured. When a ball was placed in the basin with waves present, it was observed that the ball moved both with the waves and the current in a circular pattern. It was also clear that the spiral wavemaker in the model circular wave basin produced a current in the direction of the wavemaker motion. Since the current meter could not be placed inside the surf zone, it seemed reasonable to track the movement of the ball and correlate that motion to nearshore circulation. A summary of tests filmed and recorded on super VHS tapes is shown in Table 3.1. For monochromatic waves, the ball was tracked for approximately 30 minutes in order to collect a significant amount of data across the surf zone. The length of the random wave tests were limited. The two frequency component wave was filmed for 5 minutes and the 11 component frequency wave for 1 minute. Startup conditions with waves were filmed to measure the velocity of the ball in the initial development of circulation. The ball was tracked for 3 revolutions around the basin. End of run conditions without waves were filmed to measure the circulation after the run. The ball was tracked for 1 revolution after the wavemaker was shut off.

Several different types of targets were tested. All were spherical in shape so they would roll off of the beach. Ball 1 was a superball, approximately 3 cm in diameter. It was the primary object tracked because it had a slight positive buoyancy

Table 3.1 Video data for longshore current experiment

Waves		Object Tracked	Duration of run (min)	Notes
T (sec)	H (cm)			
1.0	7.6	Ball 1	30	Run a: Live
1.0	7.6	Ball 1	30	Run b: Repeat of a
1.0	7.6	Ball 1	30	Run c: Repeat of a
1.0	7.6	Ball 1	1.0	Startup: 1 rev
1.0	7.6	Ball 1	1.5	Startup: 2 rev
1.0	7.6	Ball 1	2.5	Startup: 3 rev
1.0	7.6	Ball 1	1.0	End of run: 1 rev
1.0	7.6	Ball 1	.50	End of run: 1/2 rev
1.0	7.6	Ball 1	.25	End of run: 1/4 rev
1.0	7.6	Ball 1	30	Run d: Live
0.8	4.88	Ball 1	30	Run a: Live
0.8	4.88	Ball 1	30	Run b: Repeat of a
0.8	4.88	Ball 1	30	Run c: Live
0.8	4.88	Ball 1	30	Run d: Repeat of c
0.8	4.88	Ball 1	0.5	End of run: 1/2 rev
0.8	4.88	Ball 1	1.0	End of run: 1 rev
0.8	4.88	Ball 2	0.5	End of run: 1/2 rev
0.8	4.88	Ball 2	1.0	End of run: 1 rev
1.2	6.65	Ball 1	30	Run a: Live
1.2	6.65	Ball 1	30	Run b: Live
1.2	6.65	Ball 3	1.0	End of run: 1 rev
1.2	6.65	Ball 1	1.0	End of run: 1 rev
1.2	6.65	Ball 4	1.0	End of run: 1 rev
1.2	6.65	Ball 2	1.0	End of run: 1 rev
T1=0.5, T2=1.0	H1=2.54, H2=2.54	Ball 1	5	Run a: Live
T1=0.5, T2=1.0	H1=2.54, H2=2.54	Ball 1	5	Run b: Live
11 comp. wave	11 comp. wave	Ball 1	1.0	Run a: Live
11 comp. wave	11 comp. wave	Ball 1	1.0	Run b: Live
11 comp. wave	11 comp. wave	Ball 1	1.0	Run c: Live

and it tended to remain in the surf zone during the tests. Ball 2 was also a superball about half the size of Ball 1, but was not large enough to be recognized by the tracking software. Balls 3 and 4 were a squash ball and wood ball, respectively. They were not used because they were too light, and would roll on the beach too frequently. Each test began with the tracking object at rest and at a water depth of 35.6 cm.

After each test was completed the VHS tape was analyzed by the video image software which tracked the motion of the ball. Two points of known location were determined at the beginning of each run to ground truth the images. The ground truth points were also used to determine the location of the center of the wavemaker. The tracking software would follow the movement of the ball on the screen. It would write the time in hours, minutes, seconds, and frames and the x and y coordinates in pixels to a file. To run the software, the user would play the video and position a box around the ball with the mouse. When the box was on top of the ball on the screen the user would click the mouse button and the system would begin the tracking process. The origin for this coordinate system is in the upper left hand corner of the field of view. The software was unable to track the superball at equal time intervals. It would sample approximately every 4 to 6 frames of video tape. The image processor digitizes the video at 30 frames/second, so the sampling interval was approximately 0.167 sec. Occasionally the tracking box would lose the ball when it would become submerged in the waves. The tracking box would also at times move off the ball onto a group of pixels on either the wavemaker or the area around the basin. Each time the tracking box lost the ball, the process could be reset with the

mouse button. It was necessary to monitor the tracking software at all times.

### 3.4 Longshore Current Data Analysis

A Fortran program LSCBALL, was written to read the tracking data file and calculate velocities in both the radial and tangential directions. The velocity of the ball is obtained by the following

$$V_x = \frac{[x(i+1)-x(i)]}{\Delta t} \quad (3.7)$$

$$V_y = \frac{[y(i+1)-y(i)]}{\Delta t} \quad (3.8)$$

were  $V_x$  and  $V_y$  are velocities in the  $x$  and  $y$  direction,  $x(i+1)$ ,  $y(i+1)$ , and  $x(i)$ ,  $y(i)$  are two successive ball coordinates, and  $\Delta t$  is the time difference between measurements. The position of the velocity vector is placed midway between the two points. The velocities in Cartesian coordinates are then converted to polar coordinates,  $r$  and  $\Theta$ , with origin at the center of the wave basin. The origin is determined by calibrating two ground truth points with the dimensions of the basin. The radial and tangential velocities are calculated by

$$V_r = V_x \cos\Theta + V_y \sin\Theta \quad (3.9)$$

$$V_\Theta = -V_x \sin\Theta + V_y \cos\Theta \quad (3.10)$$

where  $V_r$  and  $V_\Theta$  correspond to the cross shore and longshore velocities. A diagram of the transformation from Cartesian coordinates to polar coordinates is shown in

Figure 3.5. The surf zone area is divided into concentric annuli, each 2.54 cm wide. Velocities in each annulus are summed and averaged. By averaging the velocities in each annulus, a cross shore profile of the radial and tangential velocities can be obtained. For each wave condition, the ball would bounce up on the beach after being pushed forward by the motion of the waves. The ball would collide with the beach at approximately 20 cm from the shoreline. Current data was discarded shoreward of this point because the ball would move independently of the water on the beach face. A sample data file from the video image tracking software and an output data file from program LSCBALL are given in Appendix A.

Figures 3.6 to 3.15 show averaged tangential velocity plots for the concentric annuli as a function of radial distance from the center of the wavemaker. For the monochromatic wave conditions, Figures 3.6, 3.8, and 3.10 show two separate runs for each case. Figure 3.12 shows two separate cases for a two frequency component wave and Figure 3.14 shows three separate cases for an 11 component wave system. For the monochromatic and random wave velocity plots, separate cases for the same run do not always give similar results. This may be due to the difference in the total number of measurements in each annulus. Each wave condition for separate cases were averaged. Figures 3.7, 3.9, 3.11, 3.13, and 3.15 show average tangential velocity plots for each monochromatic and random wave case.

The breaker line for the monochromatic and random wave cases was approximately 160-165 cm from the center of the wavemaker. With respect to the beach, the breaker line was approximately 25-30 cm from the shoreline. Figures 3.16

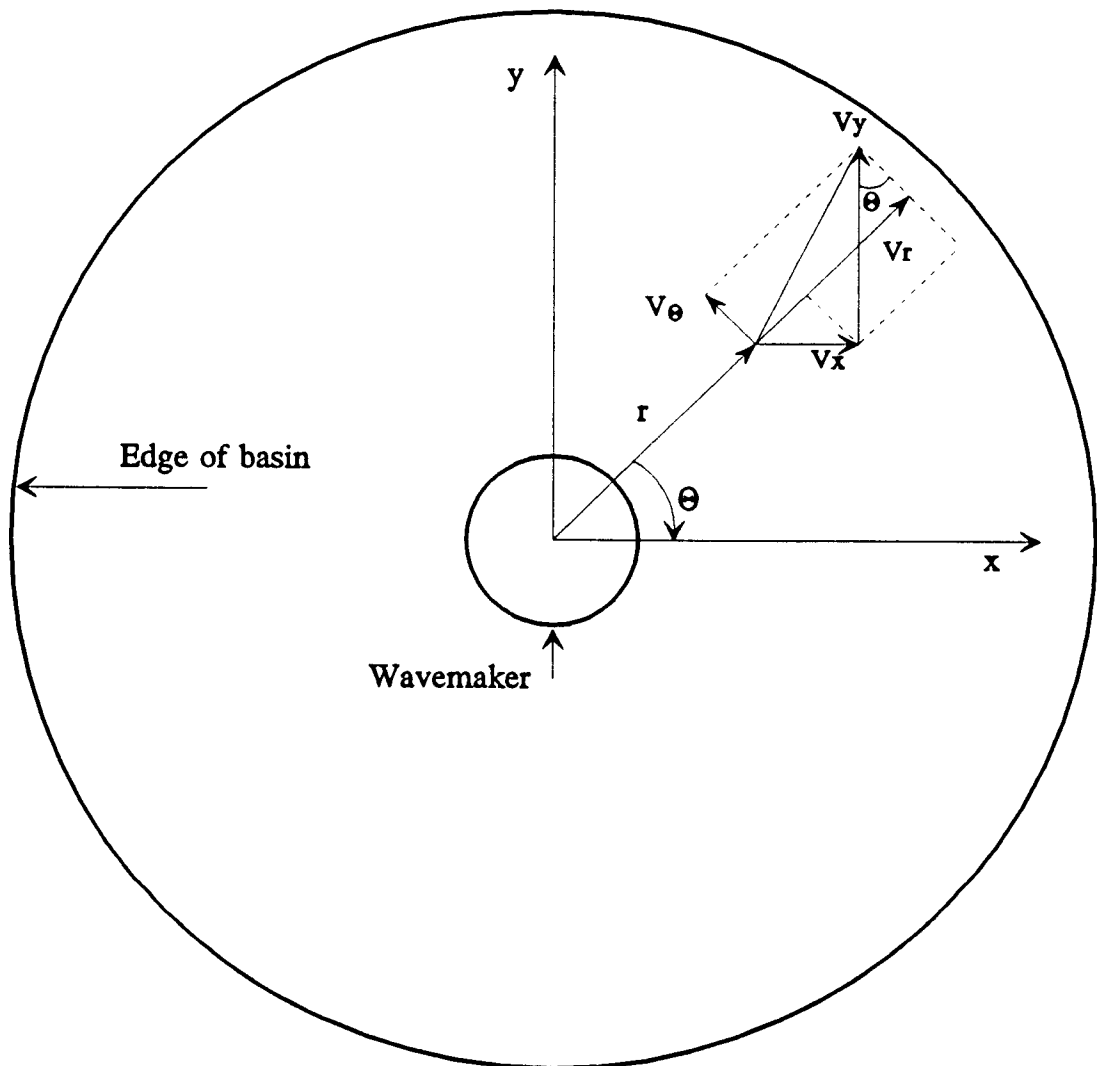


Figure 3.5 Coordinate system for velocities in circular wave basin.

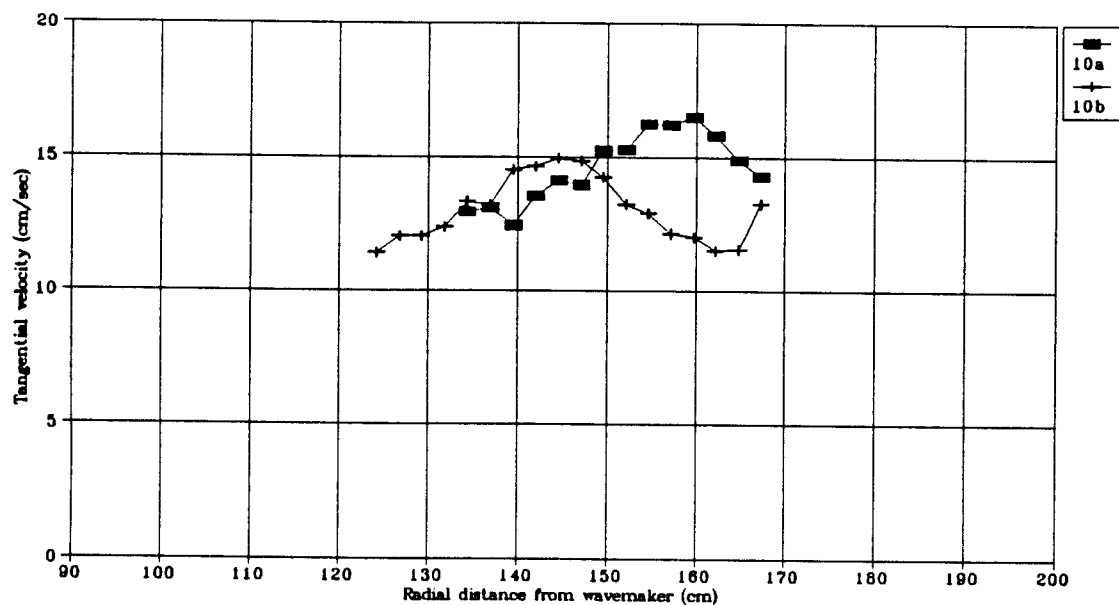


Figure 3.6 Tangential velocity for two cases:  $T=0.8$  sec,  $H=4.88$  cm.

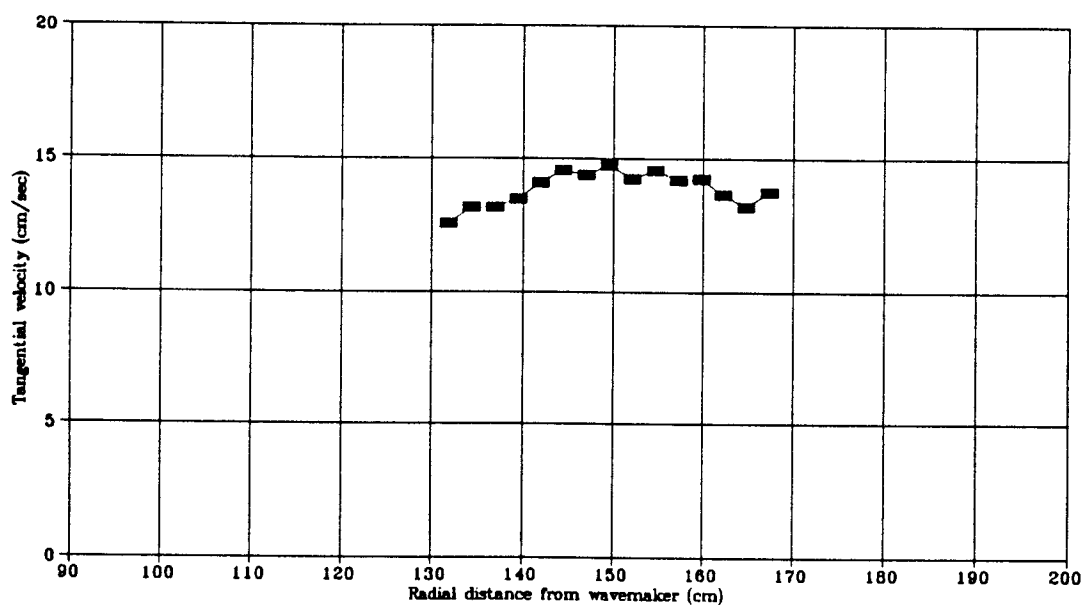


Figure 3.7 Average tangential velocity for two cases:  $T=0.8$  sec,  $H=4.88$  cm.

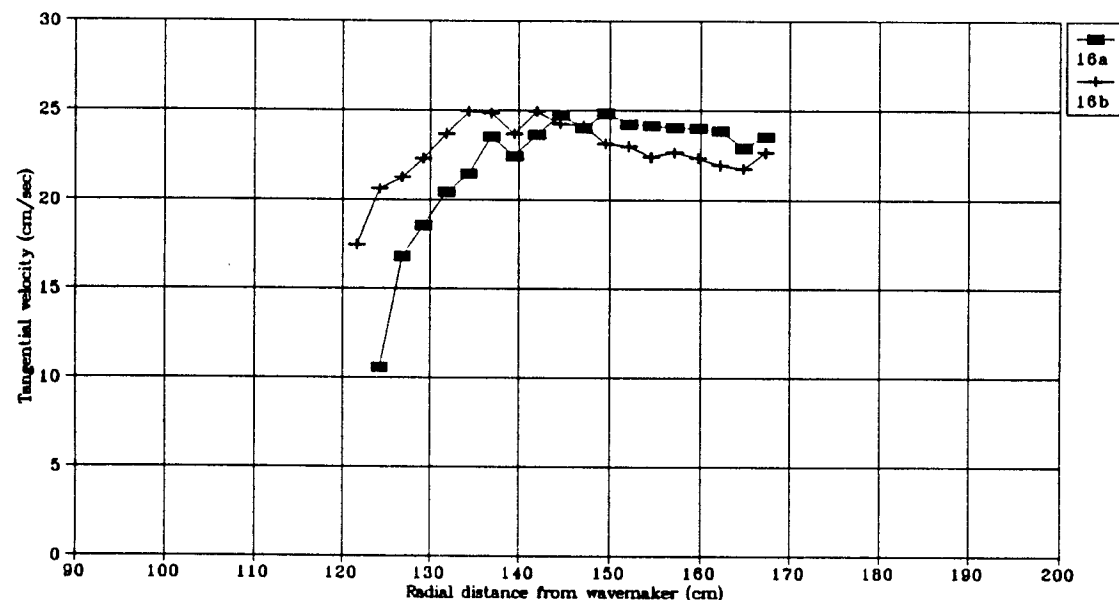


Figure 3.8 Tangential velocity for two cases:  $T=1.0$  sec,  $H=7.6$  cm.

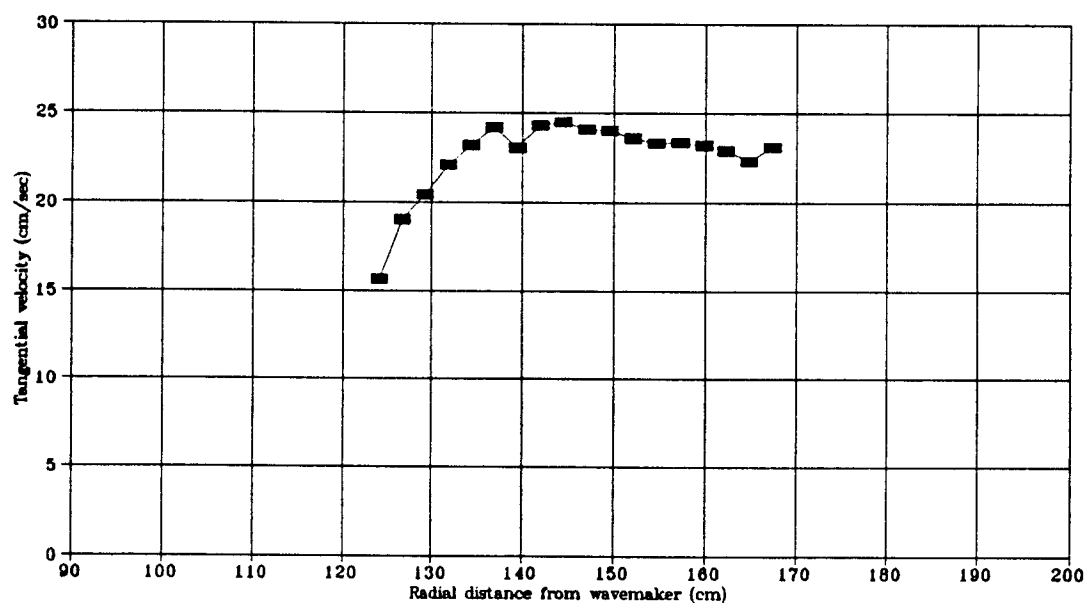


Figure 3.9 Average tangential velocity for two cases:  $T=1.0$  sec,  $H=7.6$  cm.

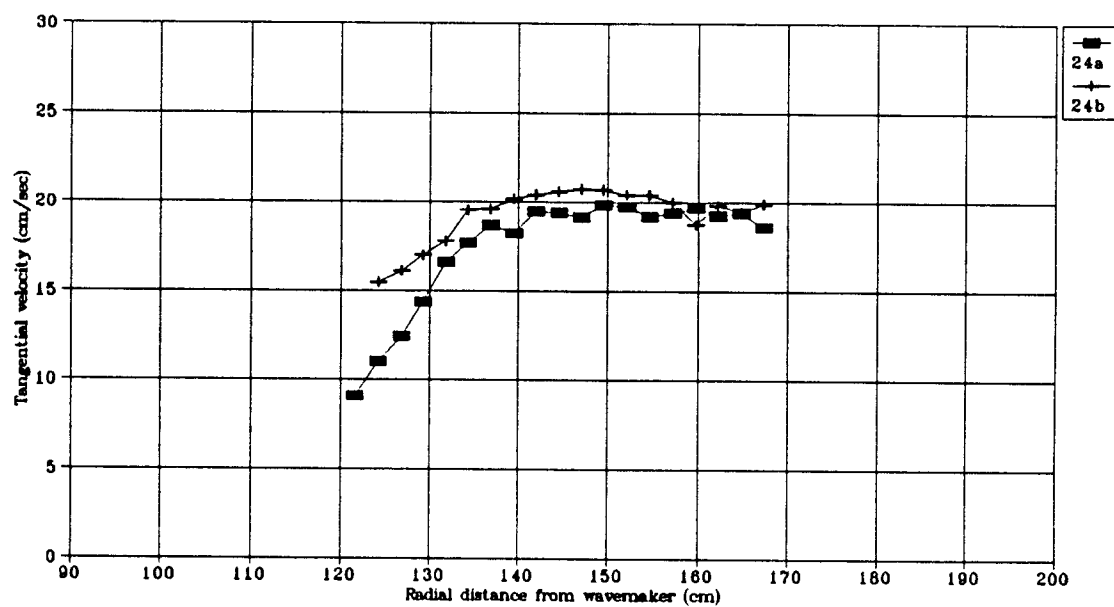


Figure 3.10 Tangential velocity for two cases:  $T=1.2$  sec,  $H=6.65$  cm.

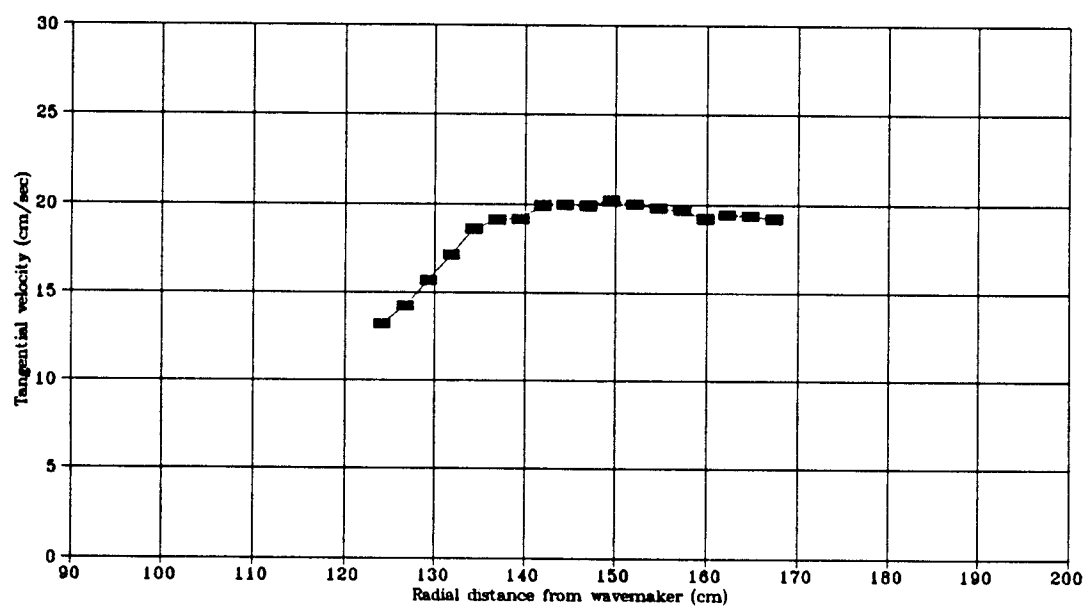


Figure 3.11 Average tangential velocity for two cases:  $T=1.2$  sec,  $H=6.65$  cm.

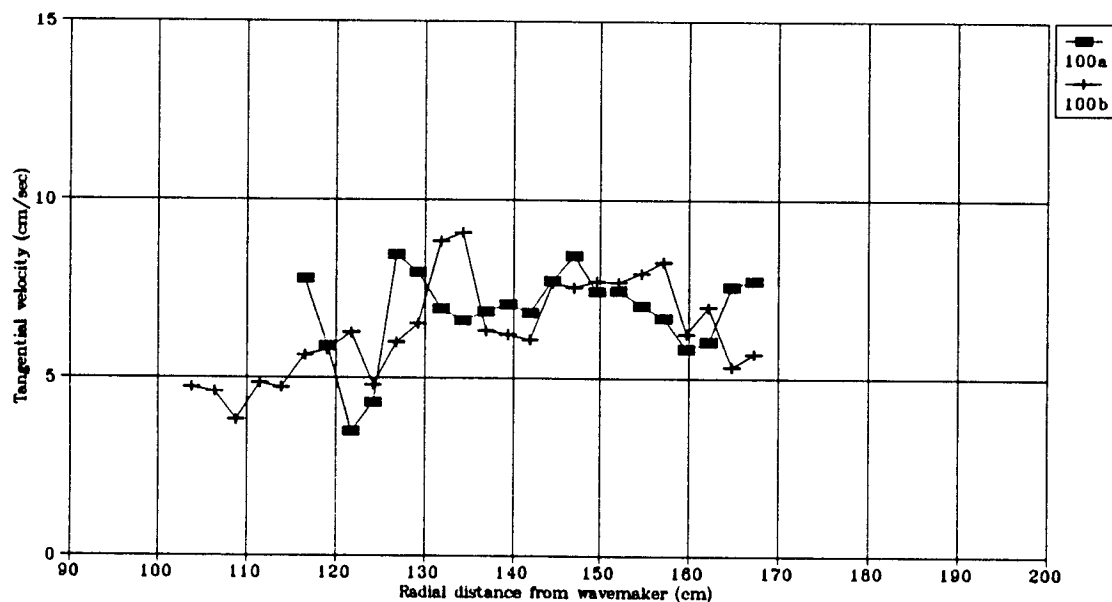


Figure 3.12 Tangential velocity for two cases:  $T_1=0.5$  sec,  $T_2=1.0$  sec.

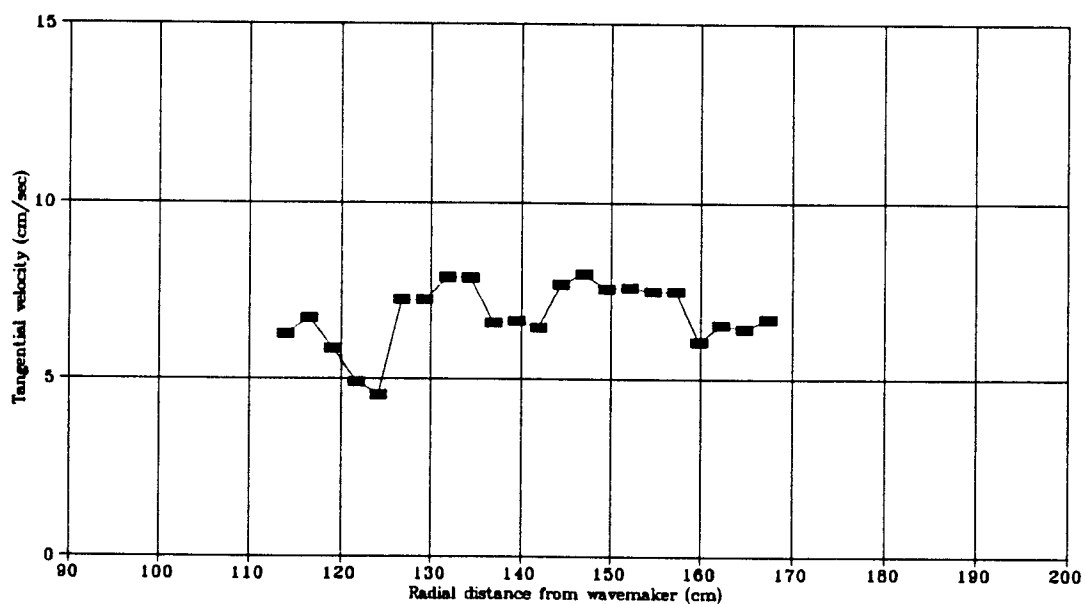


Figure 3.13 Average tangential velocity for two cases:  $T_1=0.5$  sec,  $T_2=1.0$  sec.

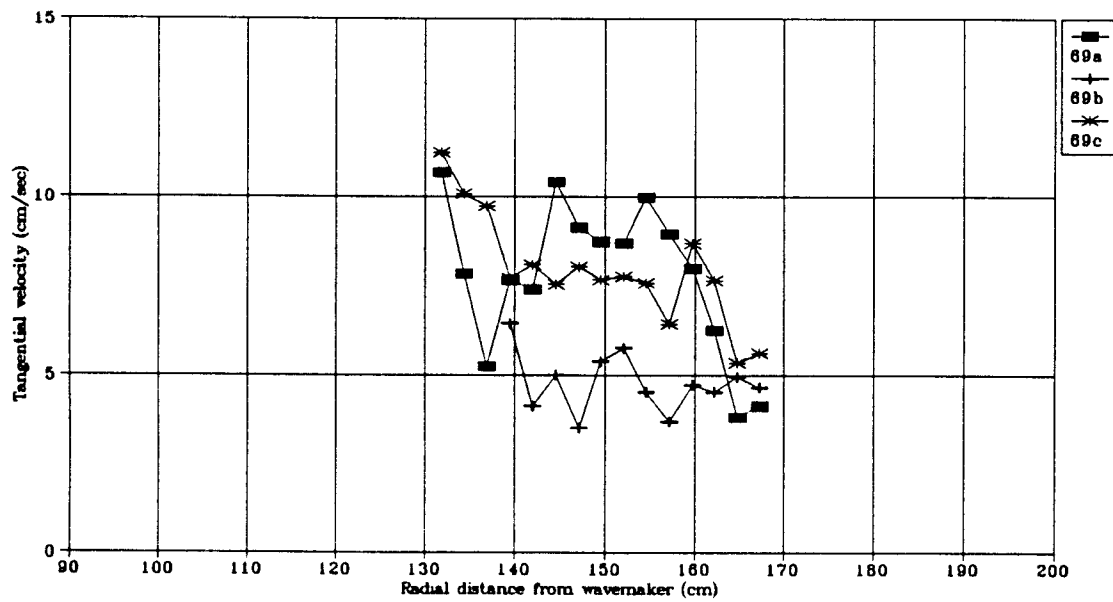


Figure 3.14 Tangential velocity for three cases: 11 component wave.

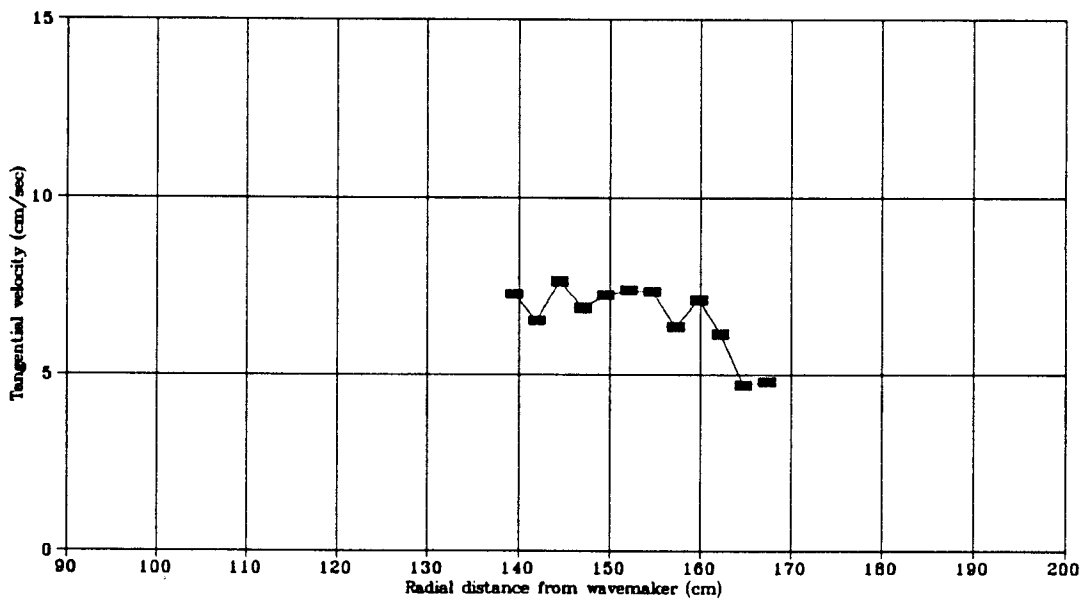


Figure 3.15 Average tangential velocity for three cases: 11 component wave.

to 3.18 show averaged measured velocities for monochromatic waves with respect to distance from the shoreline and the breaker line. These figures also show the SWL, the breaker line, and the wavemaker as a function of cross shore distance in the circular wave basin.

Each test began with the ball at rest and ended with the ball circulating around the wave basin. To see how the circulation developed upon starting the wavemaker, the ball was tracked for three revolutions at the beginning of a test. The data file was analyzed by taking 30 second segments and calculating velocities. Figure 3.19 shows four 30 second segments of tangential velocity approximately 160 cm from the center of the wavemaker. It is apparent from this plot that the tangential current developed quite quickly in the first minute and then remained steady. To look at circulation after the test, the ball was tracked for one revolution after the wavemaker was shut off. The data file was analyzed by taking 15 second segments and calculating velocities. Figure 3.20 shows four 15 second segments of tangential velocity approximately 145 cm from the center of the wavemaker. It is clear from this plot that there is strong circulation in the basin with no waves at the end of the run. The rate at which the current begins to slow down is approximately half the spin up rate.

Figure 3.21 show a comparison of tangential current data taken with the current meter and tracked with the video system. In the region in which one can compare the two measurement techniques, the tracking method with the video gives larger values for the tangential velocity than that of the current meter. This could be a function of two things. First, the ball was pushed or tossed forward by the motion of the waves

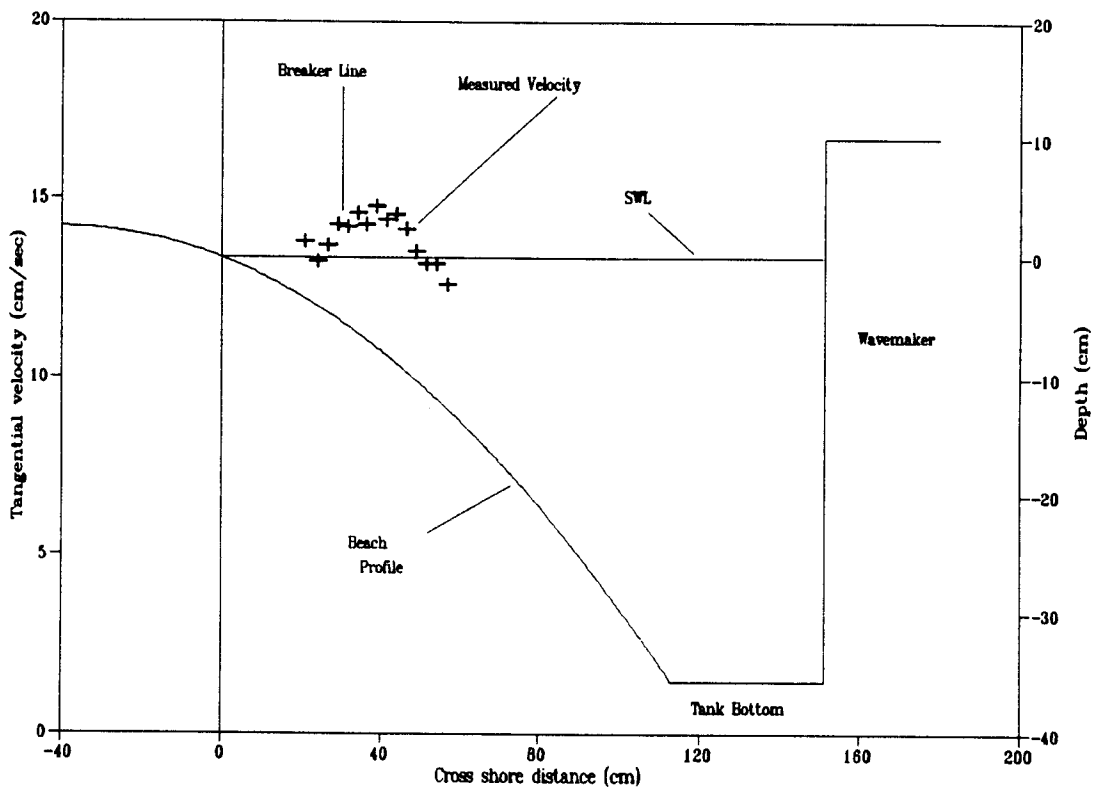


Figure 3.16 Average tangential velocity vs. cross shore distance in circular wave basin:  $T=0.8$  sec,  $H=4.88$  cm.

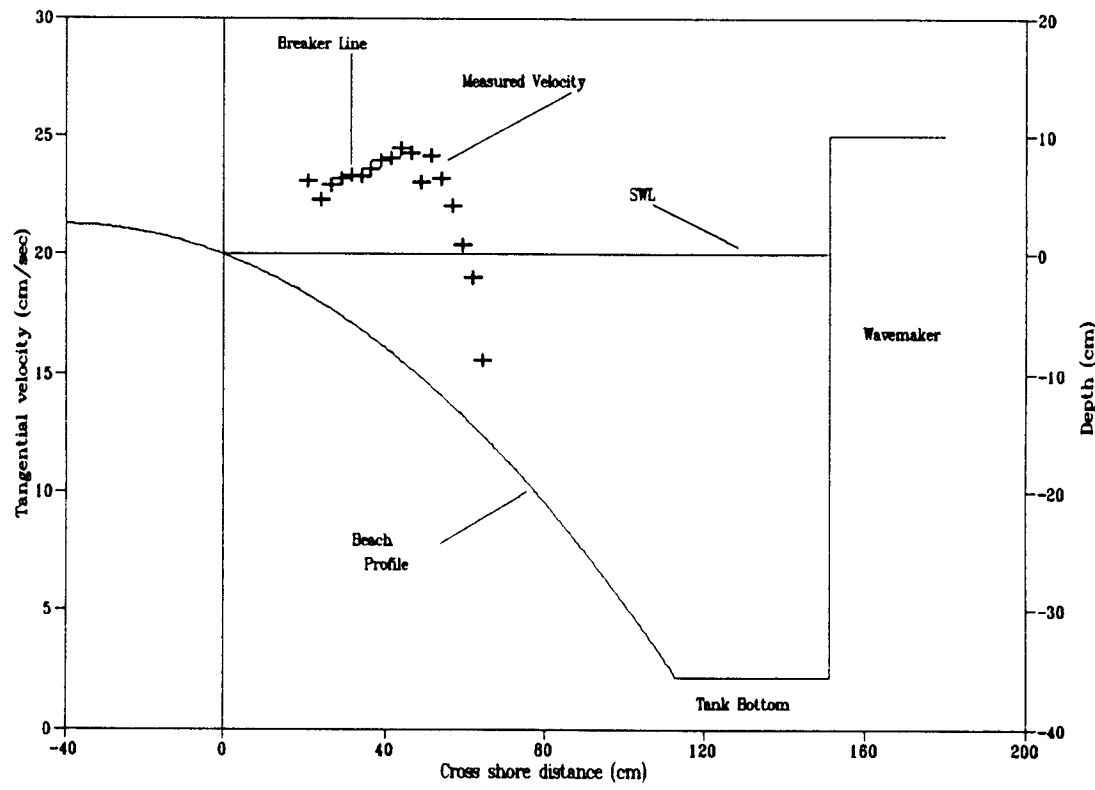


Figure 3.17 Average tangential velocity vs. cross shore distance in circular wave basin:  $T=1.0$  sec,  $H=7.6$  cm.

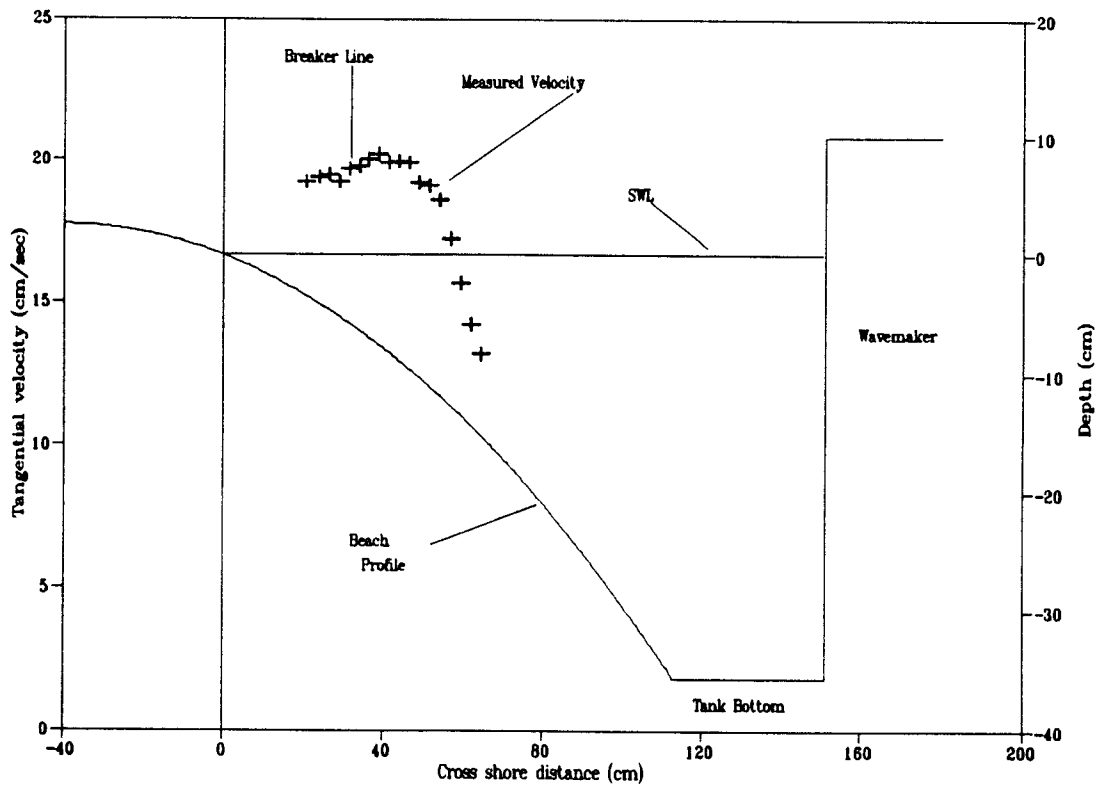


Figure 3.18 Average tangential velocity vs. cross shore distance in circular wave basin:  $T=1.2$  sec,  $H=6.65$  cm.

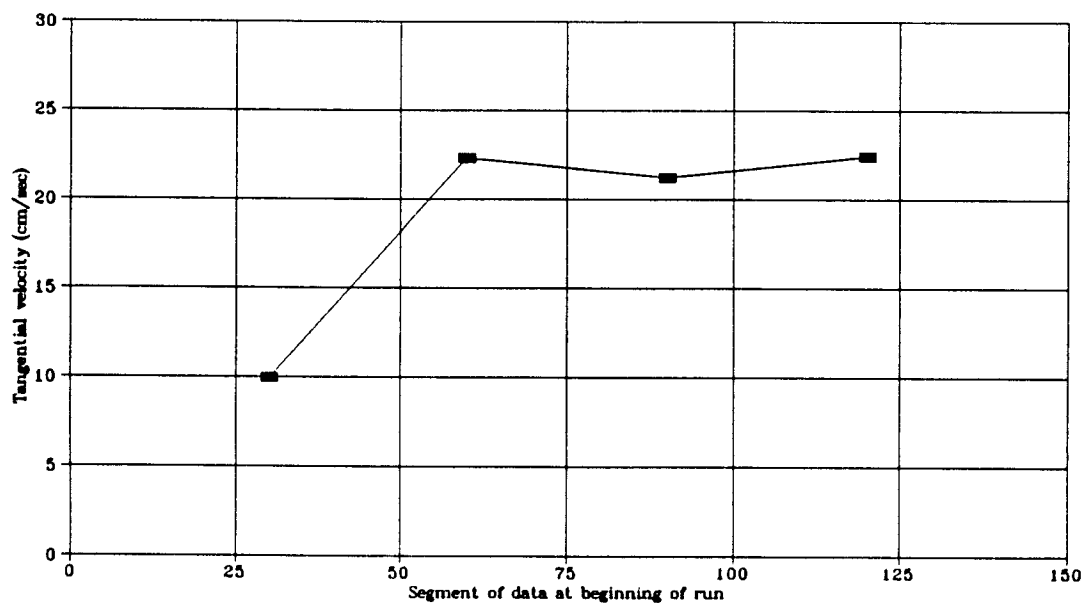


Figure 3.19 Startup conditions for 30 sec data segments:  $T=1.0$  sec,  $H=7.6$  cm.

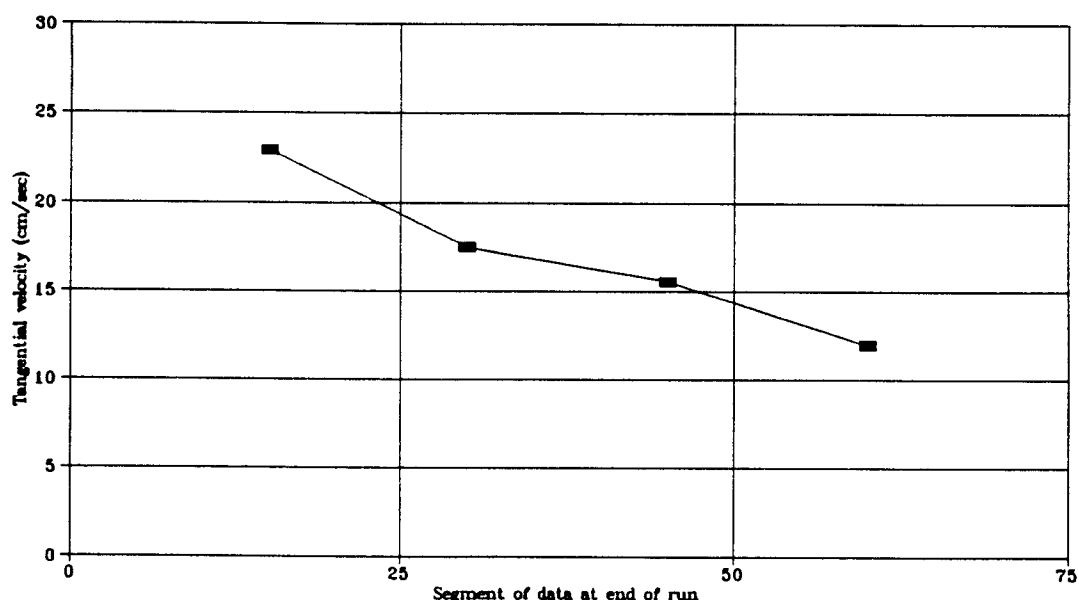


Figure 3.20 Circulation at end of run for 15 sec data segments:  
 $T=1.0$  sec,  $H=7.6$  cm.

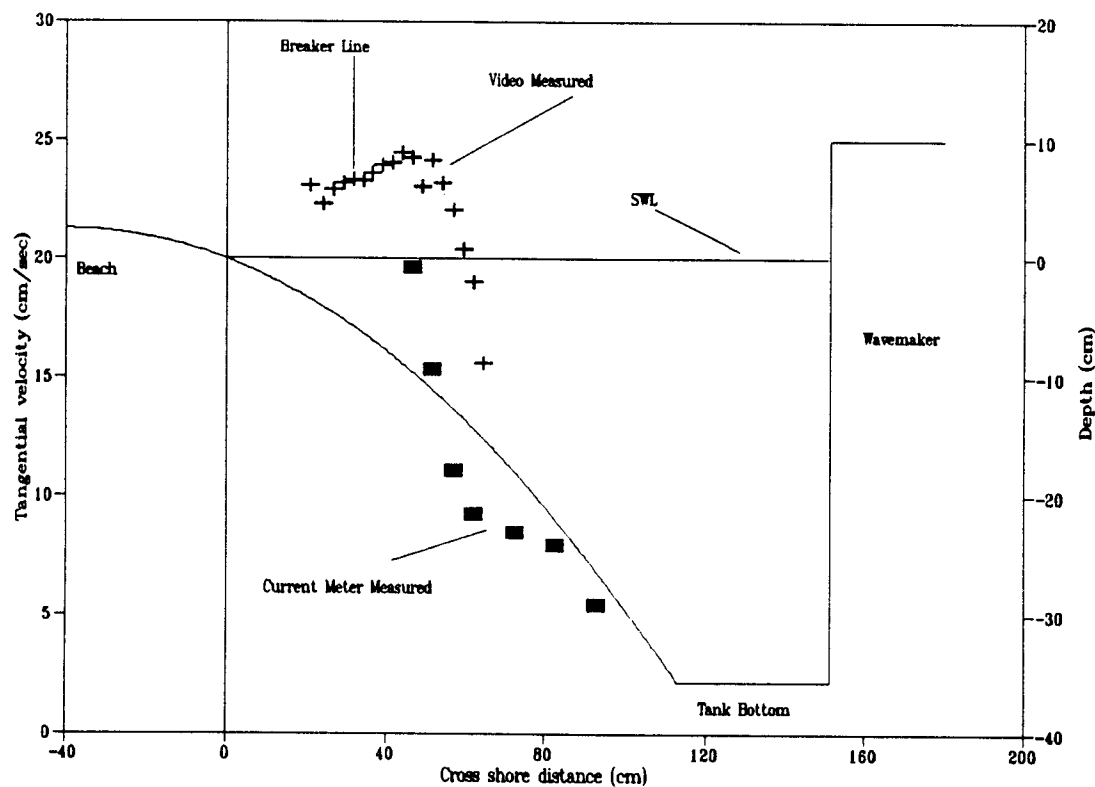


Figure 3.21 Comparison of tangential velocity taken with the video and current meter:  $T=1.0$  sec,  $H=7.6$  cm.

in the surf zone. Second, the ball would occasionally wash up on the shore and roll on the surface of the beach. For both of these cases, the velocity of the ball would increase. It was possible to eliminate errors from the second source by not including data near the shoreline. However, it was not possible to remove the data when the ball was tossed forward by the waves. As a result, tracking the ball with the video tended to give larger values for measured currents.

The longshore current is generated by waves approaching the shoreline at an oblique angle of incidence. In the governing equations for wave induced currents the angle of incidence is extremely important. It was essential to accurately measure the angle at which the waves were propagating in the circular wave basin. A subroutine to find the location of cross hairs on the screen utilizing the video imaging system was employed. For each monochromatic wave condition, a segment of video was analyzed. The subroutine would freeze the image on the screen and the user would position the cross hairs on the crest of the wave with the mouse. Each time the mouse was clicked, x and y coordinates would be recorded and written to a data file. Approximately 10 points along the crest of the wave would be recorded for each freeze frame. The coordinates were then plotted as shown in Figure 3.22. A line was drawn through successive points along the wave crest. A wave ray was drawn perpendicular to the wave crest. The angle that the wave ray is offset from a perpendicular drawn from the shoreline is the angle of incidence. Each monochromatic wave condition was analyzed with this method 5 times and an average value for  $\theta$  was determined for each case.

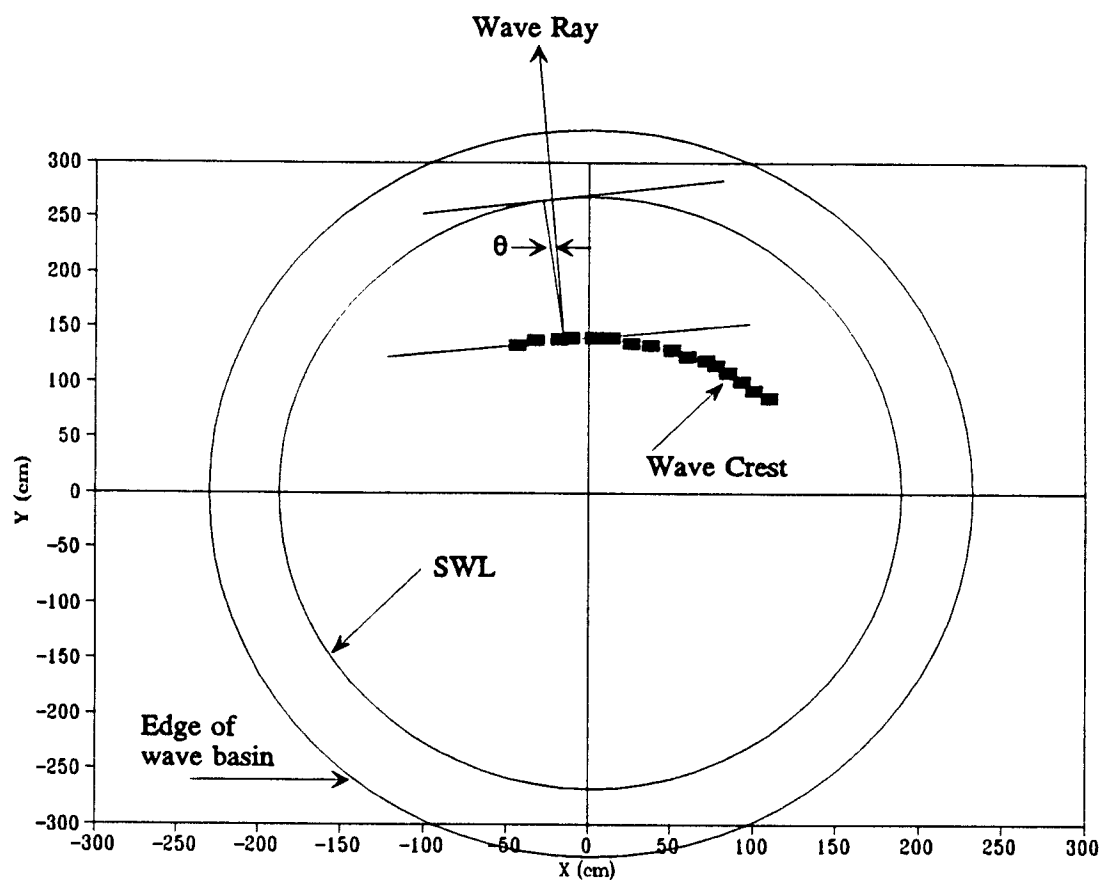


Figure 3.22 Method for calculating the angle of incidence of a spiral wave in the circular wave basin.

Longshore current data measured with both the video technique and current meter were compared with results from the numerical model, NMLONG. The coefficient of friction in the numerical model calculations was decreased from the default value of 0.01 to 0.001 to account for the smooth and impermeable concrete beach. The calculated profiles with  $C_f=0.001$  compared better with the data than by using a value of  $C_f=0.01$ . Figure 3.23 shows a comparison of a calculated NMLONG profile with current meter data for monochromatic waves with  $T=1.0$  sec,  $H=7.6$  cm,  $\theta=4^\circ$ . Although there is scatter in the data, it compares reasonably well. Figures 3.24, 3.25, and 3.26 show comparisons of NMLONG profiles with video measured longshore current data. Figure 3.24 is for monochromatic waves with  $T=1.0$  sec,  $H=7.6$  cm, and  $\theta=4^\circ$ . For this case, the magnitude of the peak velocity measured with the video is the same order of magnitude of that predicted with NMLONG, but the cross shore locations do not agree. Figure 3.25 is for monochromatic waves with  $T=0.8$  sec,  $H=4.88$  cm, and  $\theta=4^\circ$ . For this case, the NMLONG profile predicts the magnitude of the longshore current to be considerably greater than the measured data. Similar to Figure 3.24, the cross shore locations of the peak current do not agree. Figure 3.26 is for monochromatic waves with  $T=1.2$  sec,  $H=6.65$  cm, and  $\theta=4^\circ$ . This case is very similar to Figure 3.24 where the measured peak longshore current is of the same order of magnitude of the predicted maximum in the longshore current by NMLONG. However, the measured maximum for the longshore current with the video is farther offshore, approximately 80 cm from the edge of the basin where as the predicted maximum velocity is approximately 50 cm from the edge of the basin.

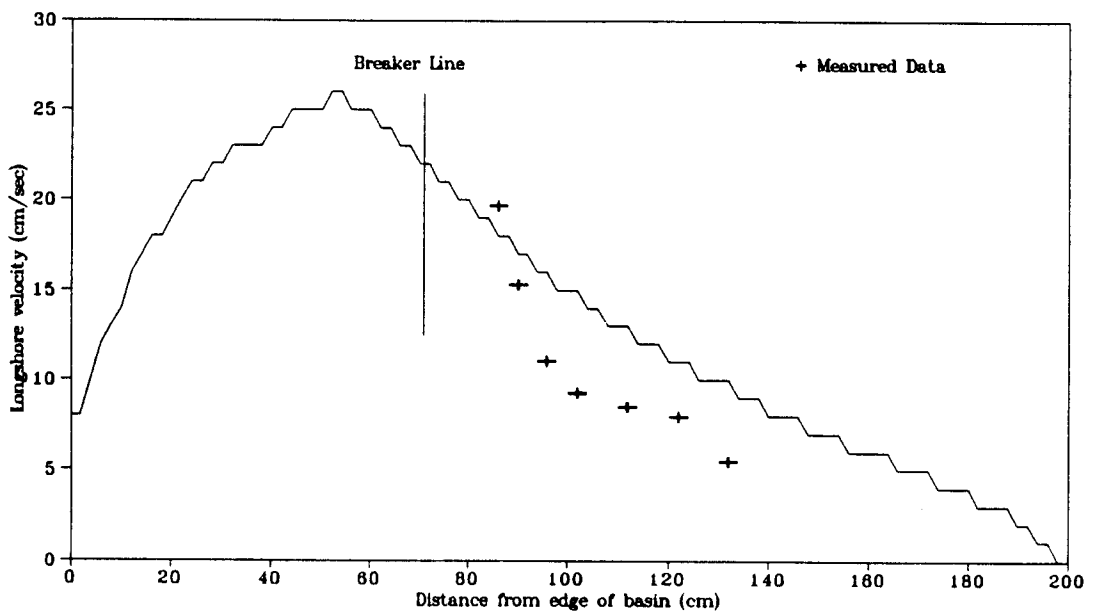


Figure 3.23 NMLONG profile and longshore current meter data:  
 $T=1.0$  sec,  $H=7.6$  cm,  $\theta=4^\circ$ .

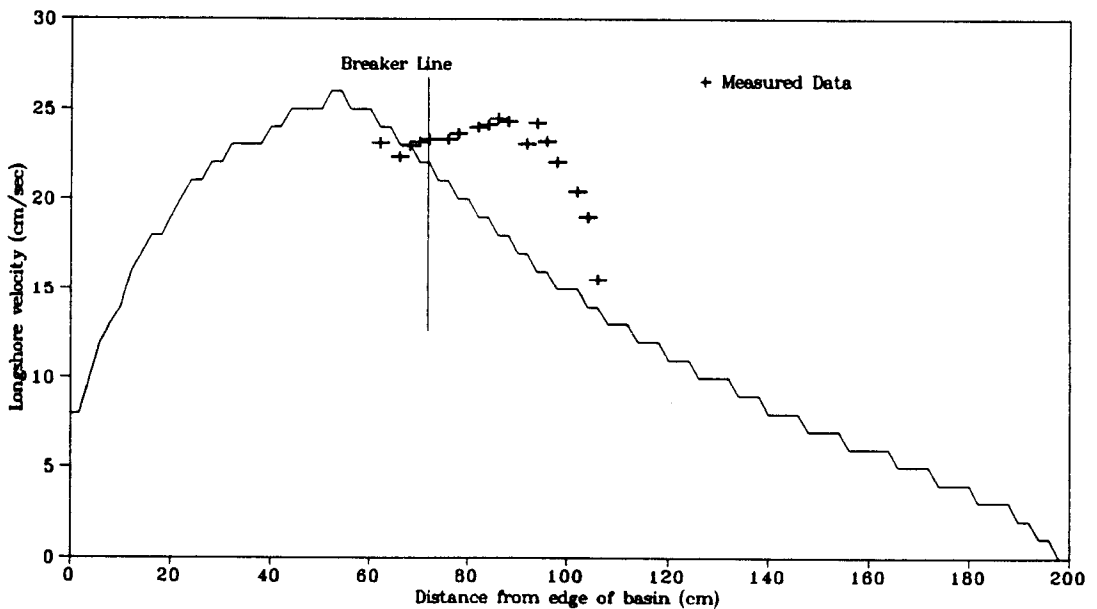


Figure 3.24 NMLONG profile and video measured longshore current data:  
 $T=1.0$  sec,  $H=7.6$  cm,  $\theta=4^\circ$ .

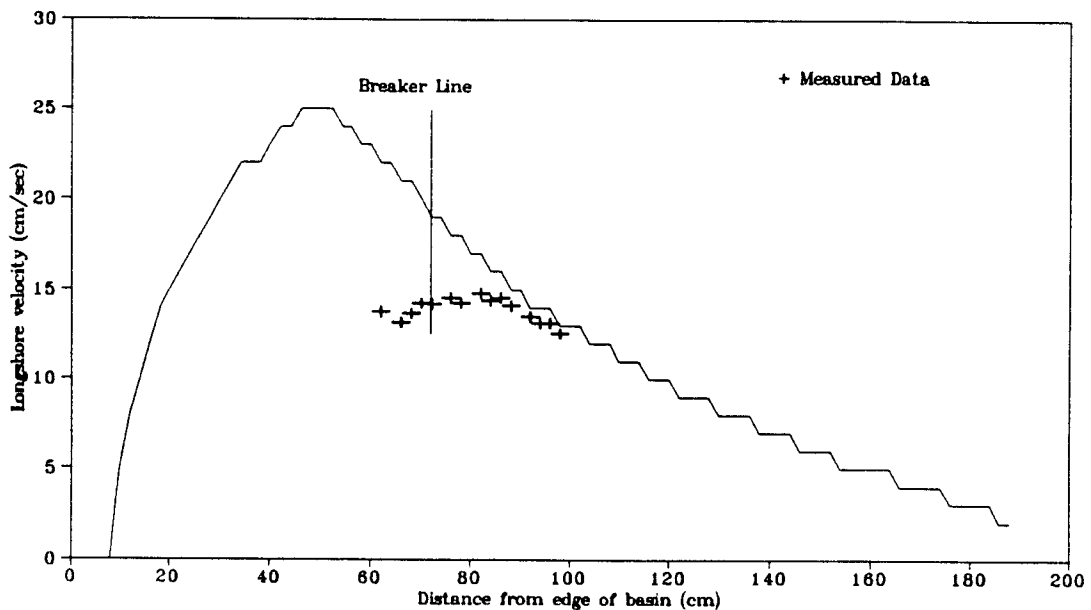


Figure 3.25 NMLONG profile and video measured longshore current data:  
 $T=0.8$  sec,  $H=4.88$  cm,  $\theta=4^\circ$ .

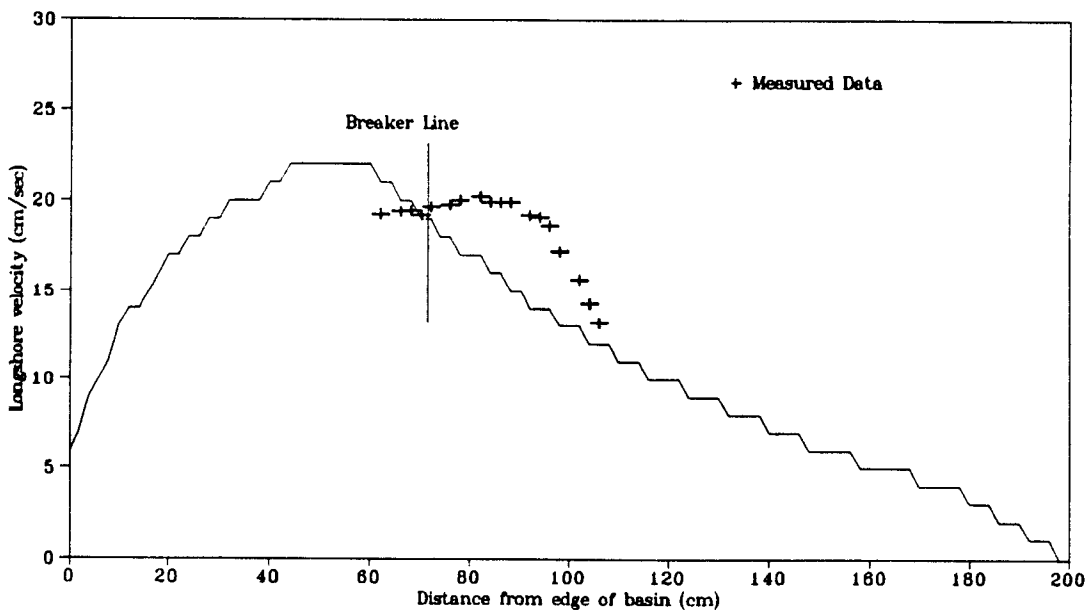


Figure 3.26 NMLONG profile and video measured longshore current data:  
 $T=1.2$  sec,  $H=6.65$  cm,  $\theta=4^\circ$ .

Comparisons of the magnitudes of the measured data both with the current meter and the video agree reasonably well with NMLONG. However, the profiles for the measured data do not agree with the NMLONG profiles as a function of cross shore location. Kraus and Larson (1991) compared field data for longshore currents from Thornton and Guza (1986) with NMLONG. In their report (Kraus and Larson, 1991), the measured and predicted magnitudes compared well, but the location of the peak in the longshore current was closer to the shoreline than the field measurements. Therefore, NMLONG seems to accurately predict the magnitude of the longshore current profile, but positions the location of the maximum longshore current more shoreward than both field and laboratory measurements indicate.

## Chapter 4

### Shear Waves

#### 4.1 Introduction

Wind generated gravity waves are typically observed at frequencies of 0.2 to 0.05 hz. As wind waves shoal and break on the coastline, their momentum and energy are transferred into several nearshore phenomena that can be distinguished as a function of frequency. Edge waves are a class of infragravity waves that are trapped in the surf zone and travel in the longshore direction. Edge waves, like gravity waves have a sea surface displacement and are usually observed at frequencies below 0.05 hz. Shear waves can have frequencies on the order of 0.001 hz (Bowen and Holman, 1989). Unlike gravity and edge waves, shear waves do not have a sea surface displacement and occur in the far-infragravity band.

An analytical shear wave model was developed by Bowen and Holman (1989) for a hypothetical longshore current profile. The model is based on the shear in the longshore current and an instability which can result in waves with exponential growth. The model depends on the conservation of potential vorticity. Oltman-Shay, et al. (1989) analyzed longshore current data from the 1986 SUPERDUCK experiment at Duck, North Carolina and found long period oscillations in the longshore current approximately on the order of 100 seconds. The wave lengths of the oscillations were approximately 100 m, so were much too short to be gravity or infragravity waves. These oscillations are very low frequency, in the far-infragravity range and possibly

related to shear waves. Dodd et al. (1989) expanded Bowen and Holman's shear wave model to include dissipation of energy by bottom friction. The results compared favorably with longshore current data taken from one day of the SUPERDUCK experiment.

Lynn Berkery and Rob Holman (College of Oceanography at OSU) have for the past two years been conducting a comprehensive series of experiments to investigate the existence of shear waves in the circular wave basin. They have collected many velocity time series using the acoustic current meter. They have conducted a variety of spectral analyses on these current data and have established the presence of shear waves in the circular wave basin. Their preliminary findings were presented at the Fall American Geophysical Union meeting in 1991.

In this study, only an overview of shear waves is presented to demonstrate the utility of the circular wave basin. In addition to the analysis of early current meter data, the Lagrangian velocity measurements of the motion of the ball will also be analyzed for shear wave characteristics.

#### **4.2 Theoretical Background**

The shallow water equations of motions in the x and y directions, assuming bottom friction to be negligible, are

$$\frac{\partial u}{\partial t} + u \frac{\partial u}{\partial x} + v \frac{\partial u}{\partial y} = -g \frac{\partial \eta}{\partial x} \quad (4.1)$$

$$\frac{\partial v}{\partial t} + u \frac{\partial v}{\partial x} + v \frac{\partial v}{\partial y} = -g \frac{\partial \eta}{\partial y} \quad (4.2)$$

where  $u$  and  $v$  are cross shore and longshore velocities,  $t$  is time,  $g$  is the acceleration due to gravity, and  $\eta$  is the water surface displacement. Bowen and Holman (1989) consider the total velocity vector  $\mathbf{u}$  to be

$$\mathbf{u} = [u(x,y), v(x,y) + V(x)] \quad (4.3)$$

where  $V$  is the steady longshore current and  $u, v \ll V$ . By substituting equation 4.3 into 4.1 and 4.2 and retaining only linear terms, the momentum equations become

$$\frac{\partial u}{\partial t} + v \frac{\partial u}{\partial y} = -g \frac{\partial \eta}{\partial x} \quad (4.4)$$

$$\frac{\partial v}{\partial t} + u \frac{\partial V}{\partial x} + v \frac{\partial v}{\partial y} = -g \frac{\partial \eta}{\partial y} \quad (4.5)$$

Assuming that  $\partial \eta / \partial t$  is small, the conservation of mass equation is

$$\frac{\partial(uh)}{\partial x} + \frac{\partial(vh)}{\partial y} = 0 \quad (4.6)$$

where  $h$  is bottom depth. By representing  $\mathbf{u}$  in terms of a stream function so that  $uh = -\psi_y$  and  $vh = \psi_x$  equations 4.4 and 4.5 can be reduced to one equation. Assuming that the stream function is harmonic in space and time

$$\psi = \Re [\psi(x)e^{i(ky-\sigma t)}] \quad (4.7)$$

where  $k$  is the longshore wavenumber,  $\sigma$  is the longshore wave angular frequency, and  $\Re$  means the real part. In this solution,  $k$  is assumed to be real whereas  $\sigma$  and  $\psi$  can be complex. Combining the above equations yields a linearized equation for which shear waves are a possible solution

$$(V - c_p) \left[ \psi_{xx} - k^2 \psi - \frac{\psi_x h_x}{h} \right] - h \psi \left[ \frac{V_x}{h} \right]_x = 0 \quad (4.8)$$

where  $c_p$  is the phase velocity of the shear wave and the cross shore structure is defined by  $\psi$ .

Bowen and Holman (1989) determined that if the solution to equation 4.8 is complex and  $\sigma$  has a positive imaginary part,  $\sigma = \sigma_{\text{real}} + i\sigma_{\text{imag}}$ , an instability will develop. When the imaginary component of  $\sigma$  is positive, the instability has an exponential growth rate. In this region of instability, a fastest growing wave can be determined where  $\sigma_{\text{imag}}$  is a maximum. Bowen and Holman (1989) examined a solution to equation 4.8 for a flat bottom beach with a sea wall at the shoreline. A triangular longshore current profile in the cross shore was used which contained a local maximum. Typical values were used for the peak longshore current and width of surf zone compared to field data from Oltman-Shay, et al. (1989). For the flat bottom beach, a fastest growing wave was determined to have a period of 753 seconds and a wave length of 250 m. The frequency of this wave, approximately 0.001 hz, is a result of the instability, and thus referred to as a shear wave.

#### 4.3 Shear Wave Experimental Analysis

To determine the existence of shear waves in the circular wave basin it would be desirable to set up an array of current meters in both the longshore and cross shore directions. With an array of current meters, an analysis could be performed on the structure of the cross shore and longshore current. This data would indicate longshore wave length and a cross shore phase dependence between the cross shore and longshore current. This is part of the study that Berkery and Holman have been conducting. However, for initial experiments only one current meter was available at the WRL. The current meter was used in the cross shore at different radial locations from the center of the wavemaker. The video imaging system was used to track the motion of a ball in the surf zone. A summary of current data acquisition and an explanation of the experimental process was presented in Chapters 2 and 3. To investigate the possibility of shear waves existing in the circular wave basin, a spectral analysis was done for each method of measuring currents.

Measurements for cross shore and longshore currents as well as water surface profile were first analyzed at a distance of 142 cm from the center of the wavemaker. Monochromatic waves were run with a wave period of 1 second and wave height of 7.6 cm. Current measurements were recorded with the 3-D acoustic current meter and the water surface profile was measured with a resistance wave gauge. An analysis of data at this location was selected because it was near the region of maximum shear in the longshore current. Also, at this location, shear wave amplitude should be largest

and phase results most diagnostic.

Figures 4.1 and 4.3 show time series measurements for longshore and cross shore velocities. The data was collected at a sampling rate of 20 hz for approximately 205 sec. A Fourier analysis was performed on the data. Figures 4.2 and 4.4 show energy spectra for the longshore and cross shore currents. As expected, both plots show spikes at the dominant wave frequency of 1 hz. Both plots also show several superharmonics appearing at equally spaced intervals of 1 hz with decreasing amplitudes at the higher frequencies. Figure 4.5 shows a time series measurement for water surface profile sampled at 16 hz for 256 sec. A Fourier analysis was also performed for this data and an energy spectrum is shown in Figure 4.6. The water surface profile spectrum also shows the dominant energy at 1 hz with superharmonics decreasing in amplitude at the higher frequencies.

Shear waves have been identified to be most energetic in the low frequency range around 0.001 hz (Oltman-Shay et al., 1989) for field observations. The spectra plots for longshore velocity, cross shore velocity, and wave height were zoomed in on the low frequency end and shown in Figures 4.7, 4.8, and 4.9. The longshore current has low frequency energy which is more energetic than the longshore component of the wave orbital velocity as shown in Figure 4.7. Figure 4.8 shows that in the cross shore, the low frequency energy is about 1% of the incident wave energy. The longshore low frequency energy is approximately three times greater than the cross shore. Figure 4.9 shows that there is some low frequency energy in the free surface spectrum. These spectra do not confirm the presence of shear waves, but do not

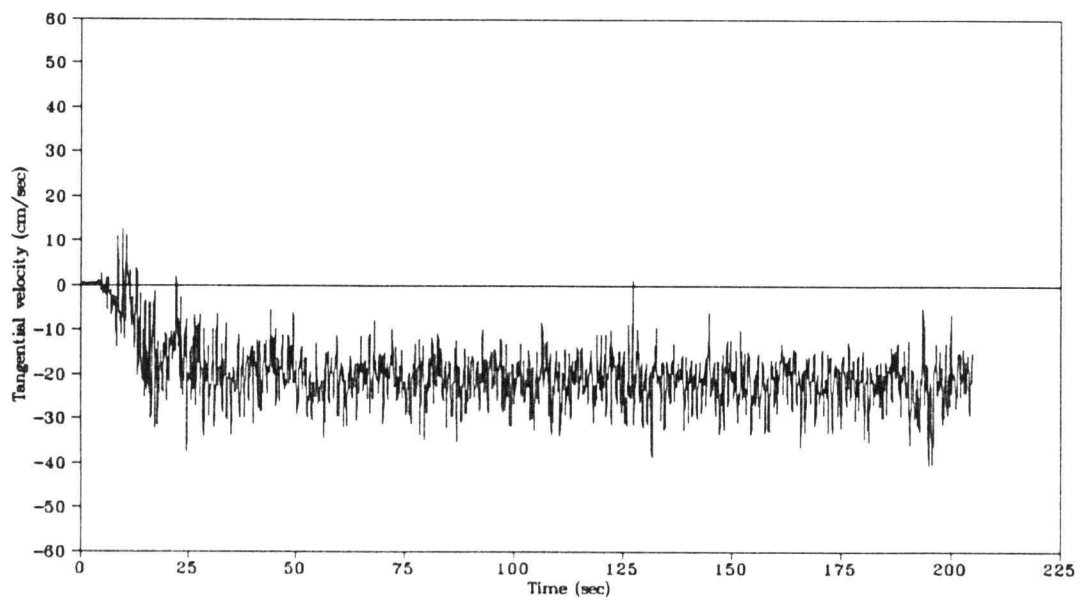


Figure 4.1 Longshore velocity 142 cm from wavemaker:  $T=1.0$  sec,  $H=7.6$  cm.

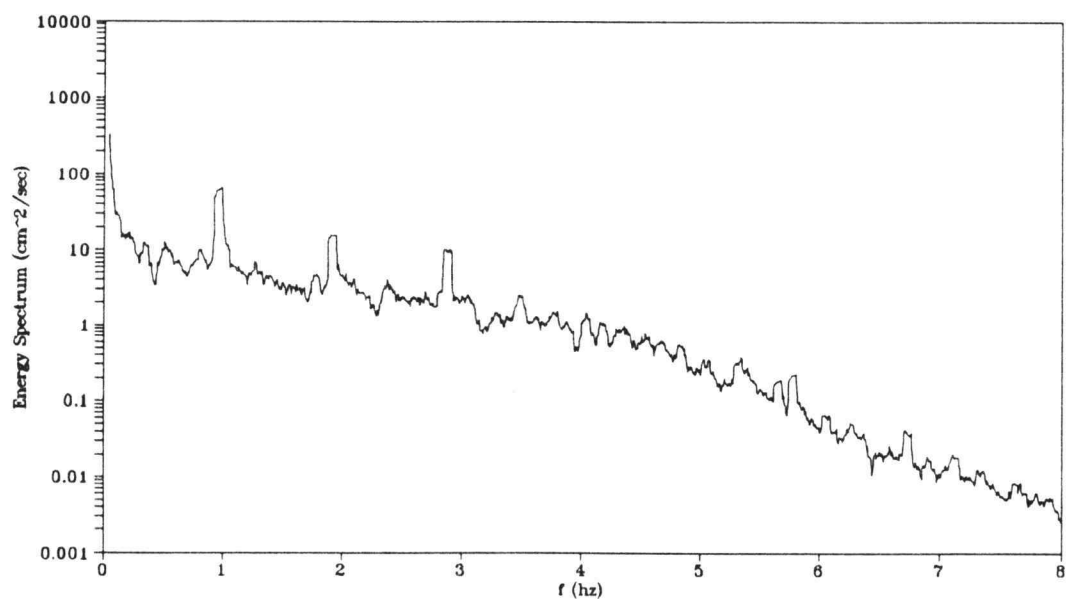


Figure 4.2 Longshore velocity spectrum:  $T=1.0$  sec,  $H=7.6$  cm.

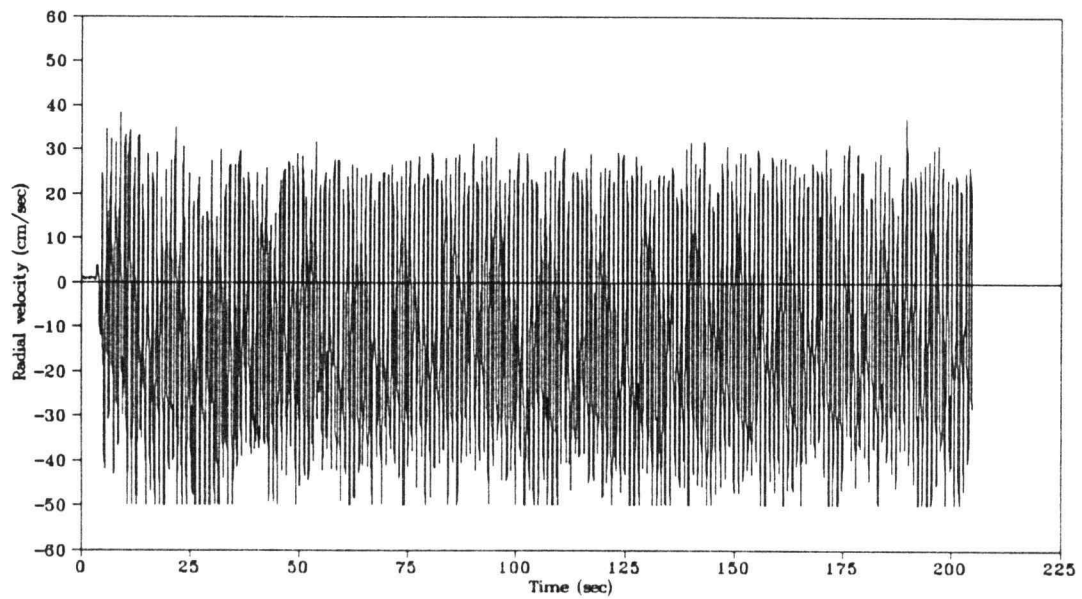


Figure 4.3 Cross shore velocity 142 cm from wavemaker:  $T=1.0$  sec,  $H=7.6$  cm.

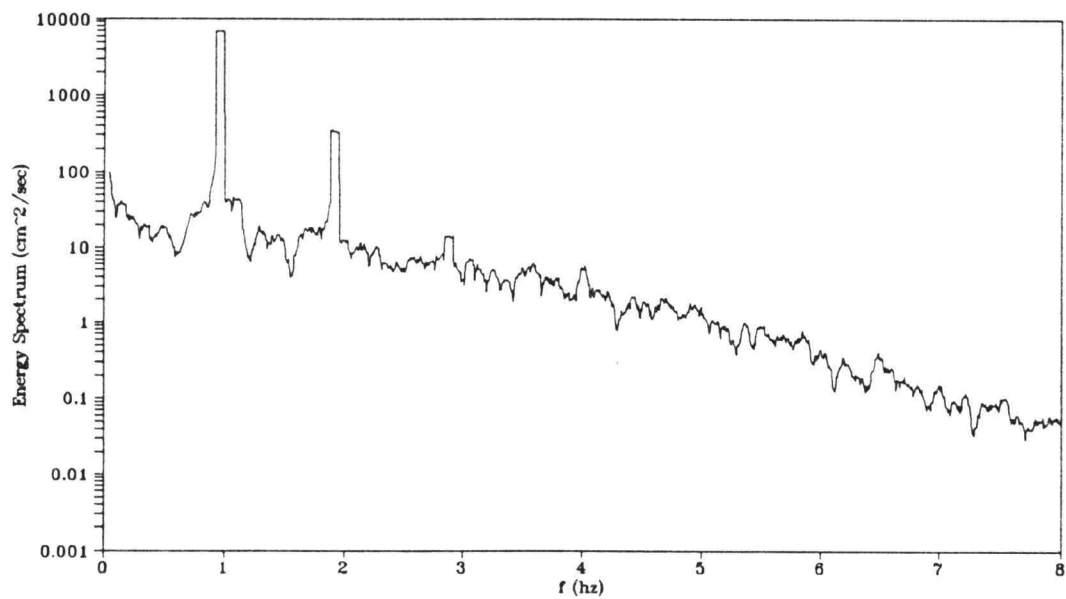


Figure 4.4 Cross shore velocity spectrum:  $T=1.0$  sec,  $H=7.6$  cm.

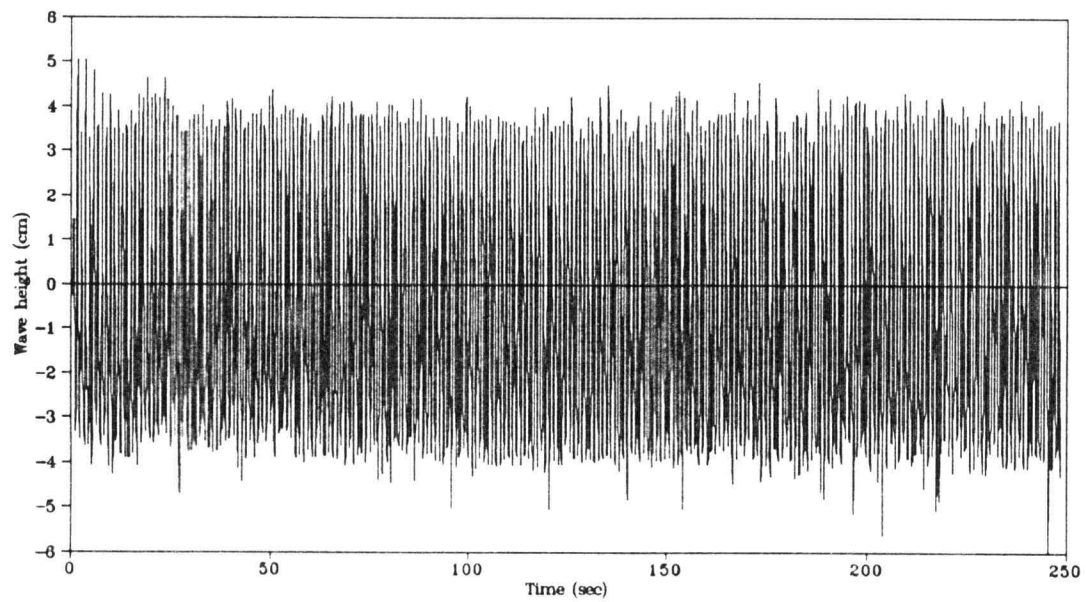


Figure 4.5 Wave profile 142 cm from wavemaker:  $T=1.0$  sec,  $H=7.6$  cm.

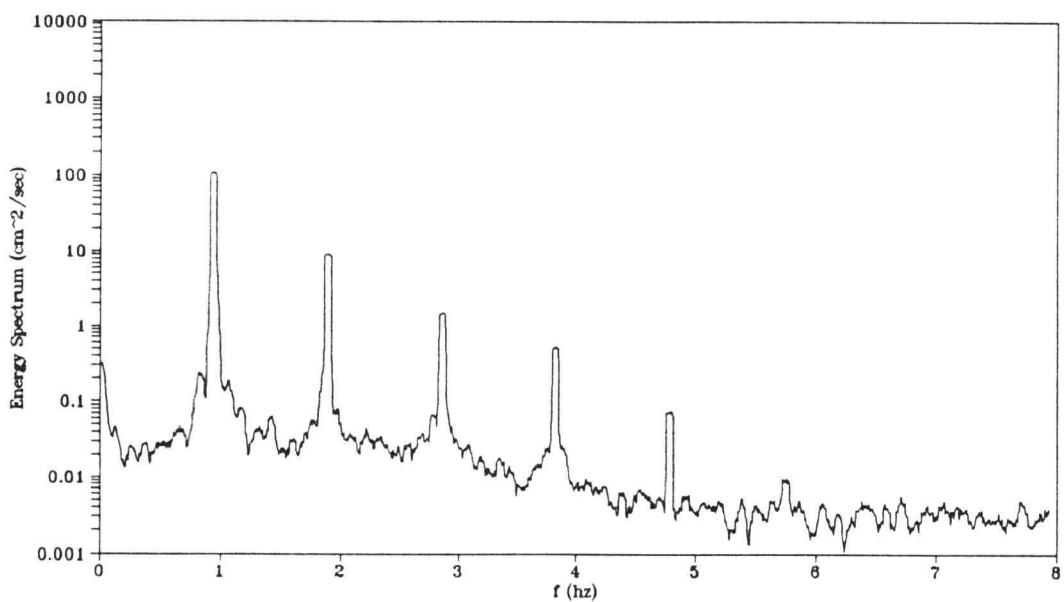


Figure 4.6 Wave profile spectrum:  $T=1.0$  sec,  $H=7.6$  cm.

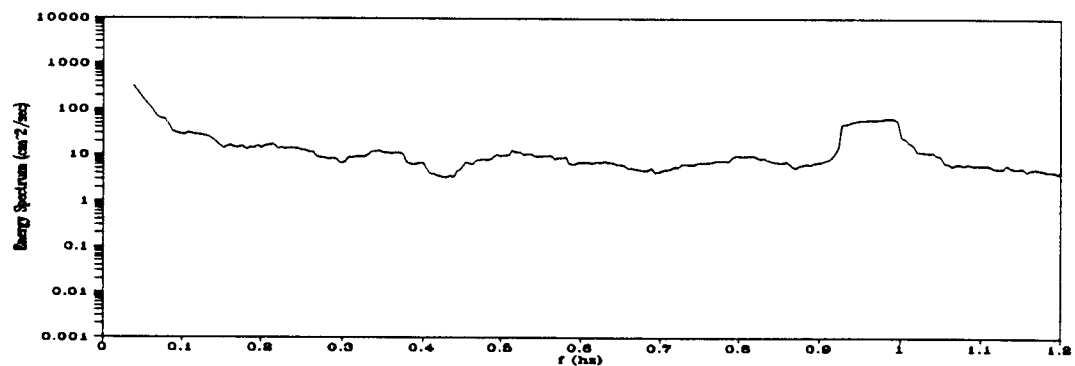


Figure 4.7 Low frequency spectrum for longshore velocity:  $T=1.0$  sec,  $H=7.6$  cm.

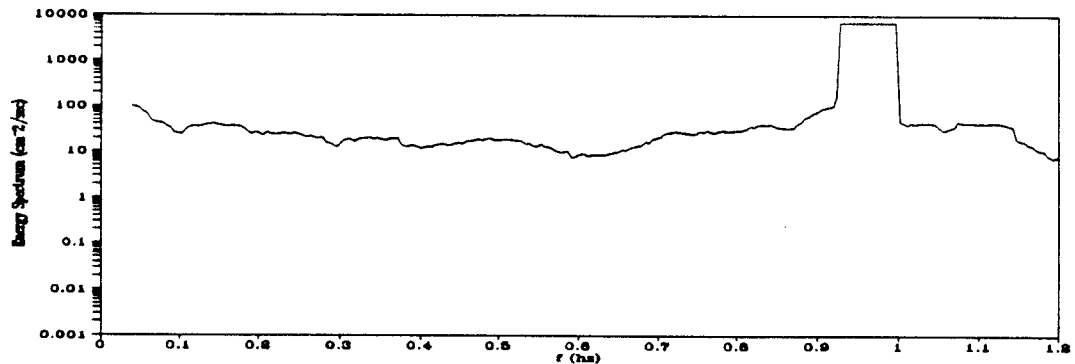


Figure 4.8 Low frequency spectrum for cross shore velocity:  
 $T=1.0$  sec,  $H=7.6$  cm.

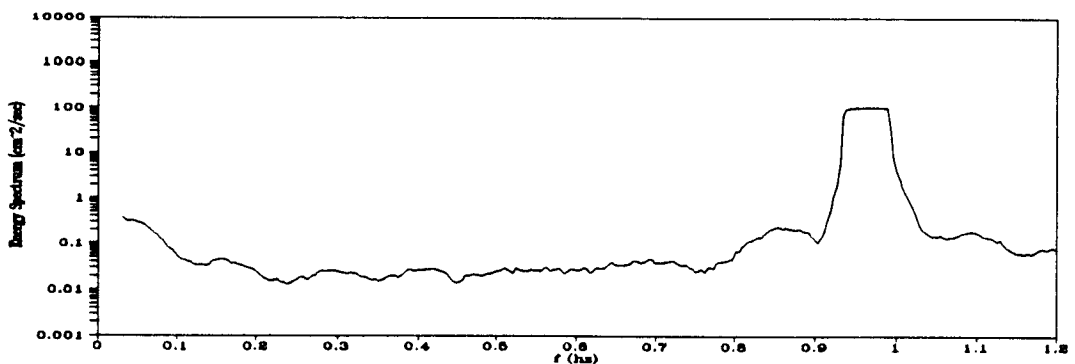


Figure 4.9 Low frequency spectrum for wave profile:  $T=1.0$  sec,  $H=7.6$  cm.

eliminate the possibility of their existence in the circular wave basin.

A spectral analysis was also performed for the video measured current data. To perform an FFT, the input needs to be spaced at equal time intervals. Unfortunately, velocity data for the ball tracking system were not equally spaced. This is because data would be discarded when the ball would come into contact with the beach and the imaging system was unable to sample data at equal time steps. To create time series for cross shore and longshore velocities with equal time steps, a linear interpolation was performed between successive velocity points. An algorithm, LINSPL, listed in Appendix A interpolates a time series of non-equal time intervals into one with equal time intervals using a linear spline.

Figures 4.10 and 4.12 show the linear interpolated time series for cross shore and longshore velocities measured with the video. Figures 4.11 and 4.13 show energy spectra for both the cross shore and longshore currents. In comparing video spectra with current meter spectra for the same monochromatic wave conditions, there is some similarity. Both methods of measurement show spikes at the dominant incident wave frequency of 1 hz as expected. The magnitude of energy for the longshore current measured with the current meter and the video seem to agree well at both 1 hz and the low frequency end. Cross shore spectra for both methods of measurement show similar results for the magnitude of energy at 1 hz. However, there is much more energy observed with the video at the low frequency end than with the current meter. The increase in low frequency energy for the video measurements may be due to filling the gaps in the time series by linear interpolation. The video spectra for both the

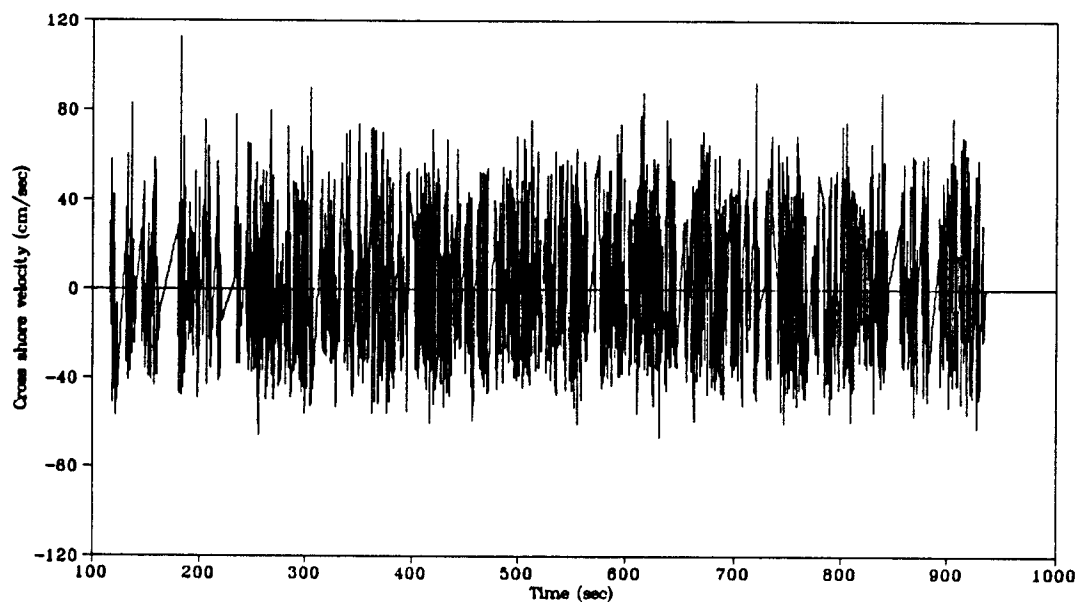


Figure 4.10 Cross shore velocity measured with video:  $T=1.0$  sec,  $H=7.6$  cm.

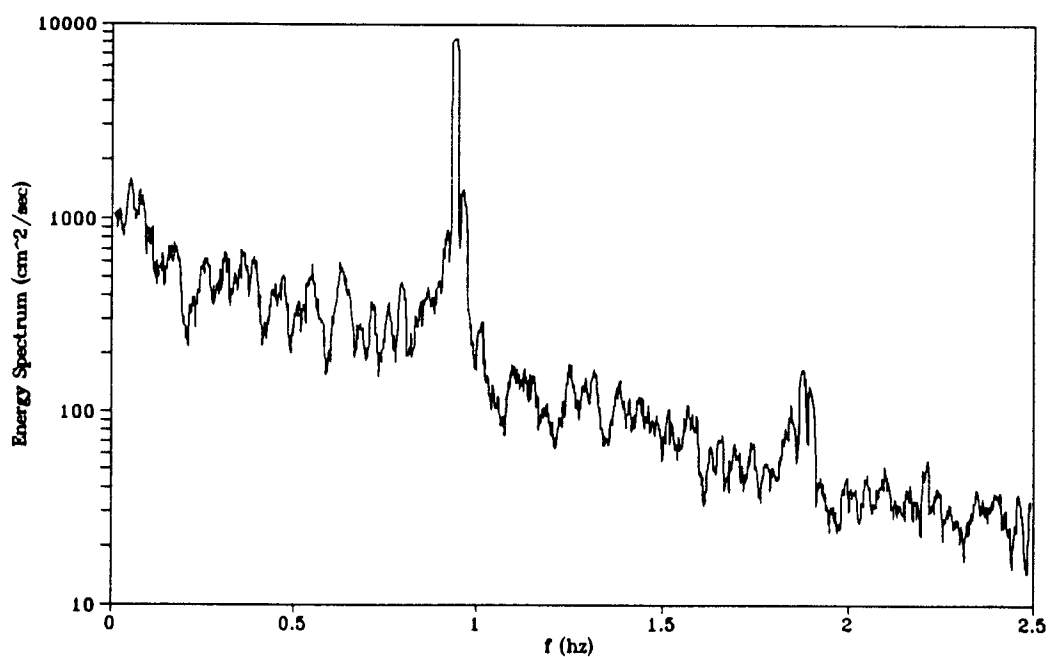


Figure 4.11 Cross shore video velocity spectrum:  $T=1.0$  sec,  $H=7.6$  cm.

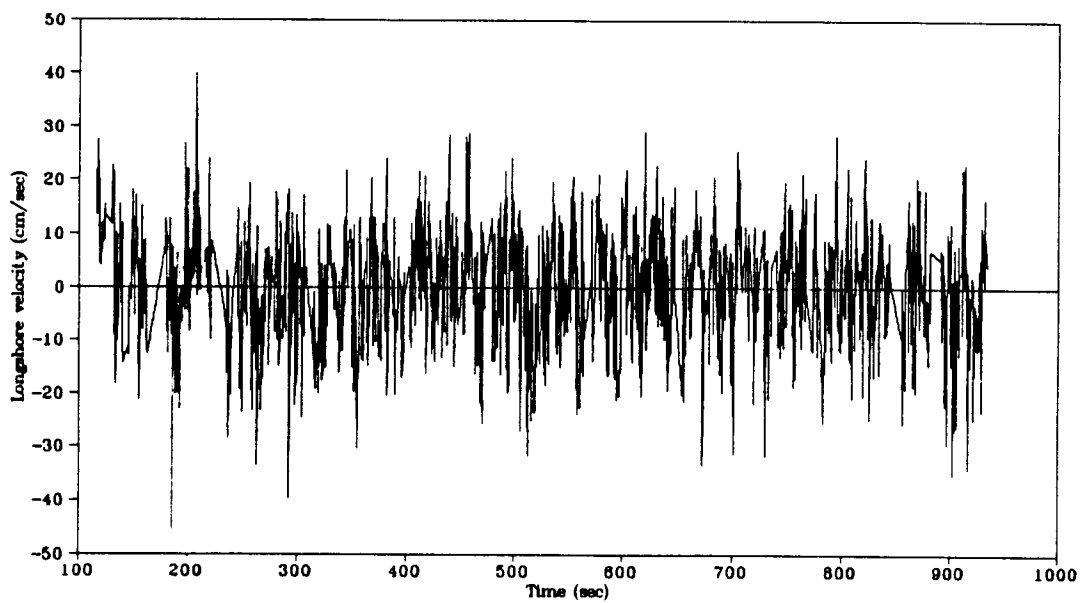


Figure 4.12 Longshore velocity measured with video:  $T=1.0$  sec,  $H=7.6$  cm.

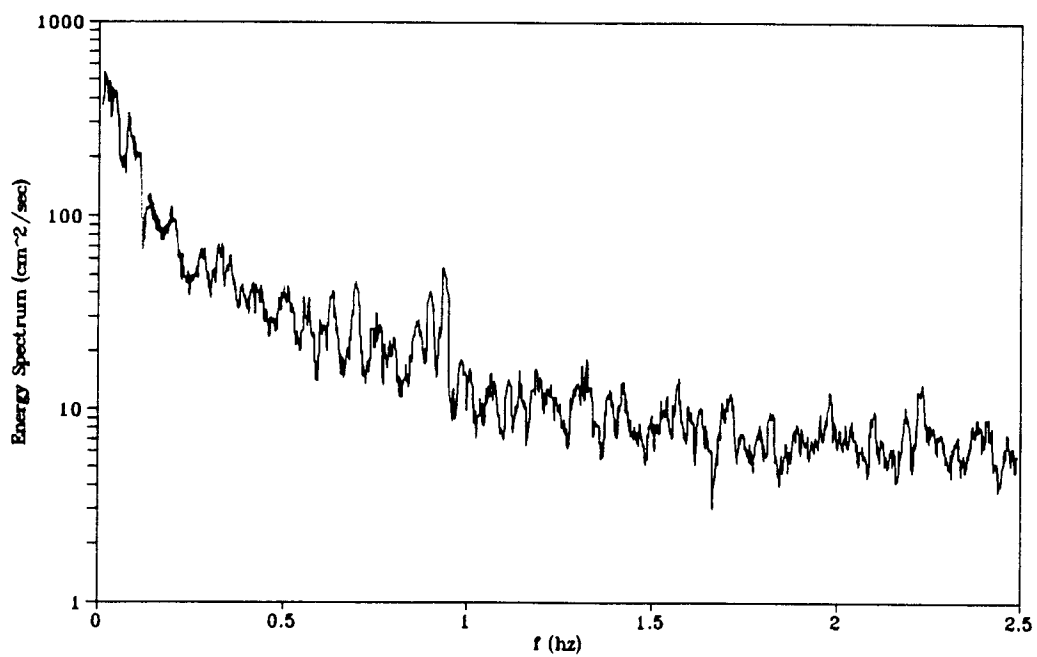


Figure 4.13 Longshore video velocity spectrum:  $T=1.0$  sec,  $H=7.6$  cm.

longshore and cross shore velocities also show a considerable amount of noise associated with the calculated velocities.

The low frequency end of the spectrum is shown in Figure 4.14 for the cross shore and longshore velocities measured with the video. The spectrum shows the longshore current to be much more energetic at the low frequency end. On the other hand, the dominant wave energy measured in the cross shore velocity is much larger than the energy in the low frequency. The video spectra, like the current meter spectra, show the existence of energetic motions in the low frequency range for the longshore current.

More measurements are needed to clearly conclude the presence of shear waves. Berkery and Holman have been pursuing this line of research and have demonstrated that shear waves do exist in the circular wave basin. The circular wave basin appears to be a useful tool in generating energetic low frequency oscillations in the longshore current.

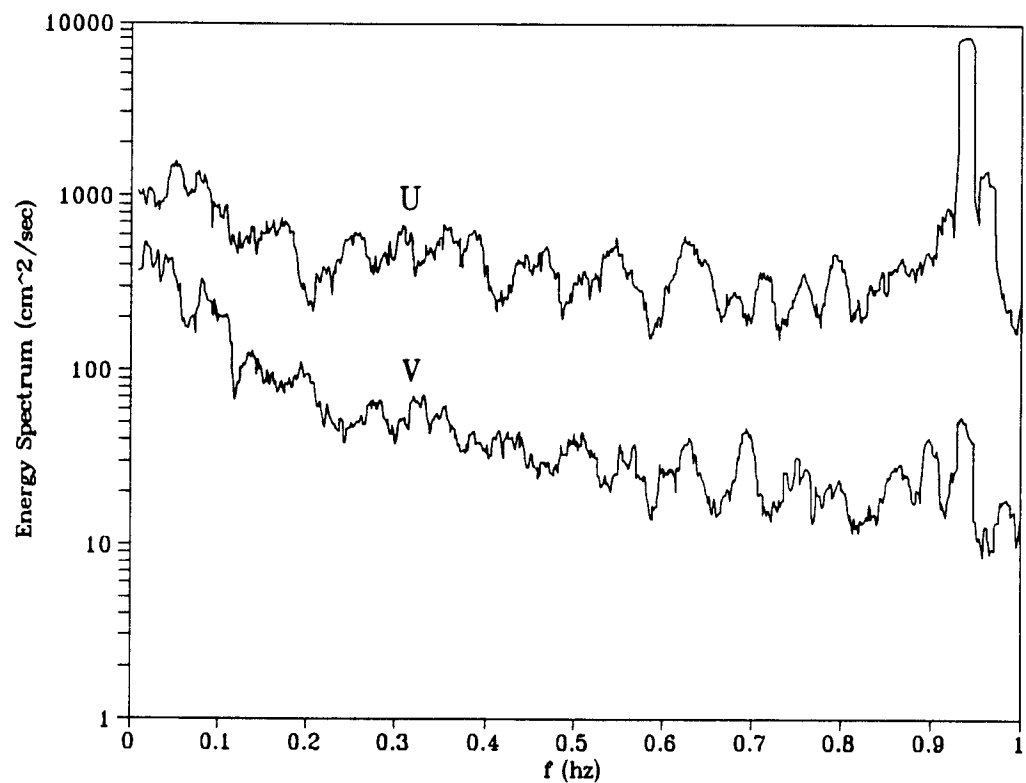


Figure 4.14 Low frequency spectrum for cross shore (U) and longshore (V) velocities measured with the video:  $T=1.0$  sec,  $H=7.6$  cm.

## Chapter 5

### Groins

#### 5.1 Introduction

Groins and jetties are common coastal structures built to reduce erosion and improve navigation. Jetties are constructed at entrances to harbors and bays to shelter navigation channels from shoaling and breaking waves and to block sediment transport. Groins are placed along the shoreline to interrupt the longshore transport to minimize erosion and maintain beaches. The longshore transport of sand is a function of the direction of the incoming waves and the longshore current. When a groin or a jetty is built, coastal circulation processes are altered and erosion and accretion can occur. It is necessary to have an understanding of how the natural littoral process will change before coastal structures are built.

Groins and jetties both interrupt the sand transport along the shoreline. However, they are built with different purposes. Groins are usually built perpendicular to the shoreline and extend out well past the breaker zone. Groins are designed to be impermeable or permeable depending on the wave climate and sand transport. Impermeable groins are built with sheet pile or concrete whereas permeable groins are built with rip rap or wood beams. When a groin is constructed along the shoreline as shown in Figure 5.1a, accretion of sediment occurs on the updrift side and erosion occurs on the downdrift side. With one groin it is possible to maintain and stabilize a small portion of coastline. To counteract the erosion on the downdrift side it might

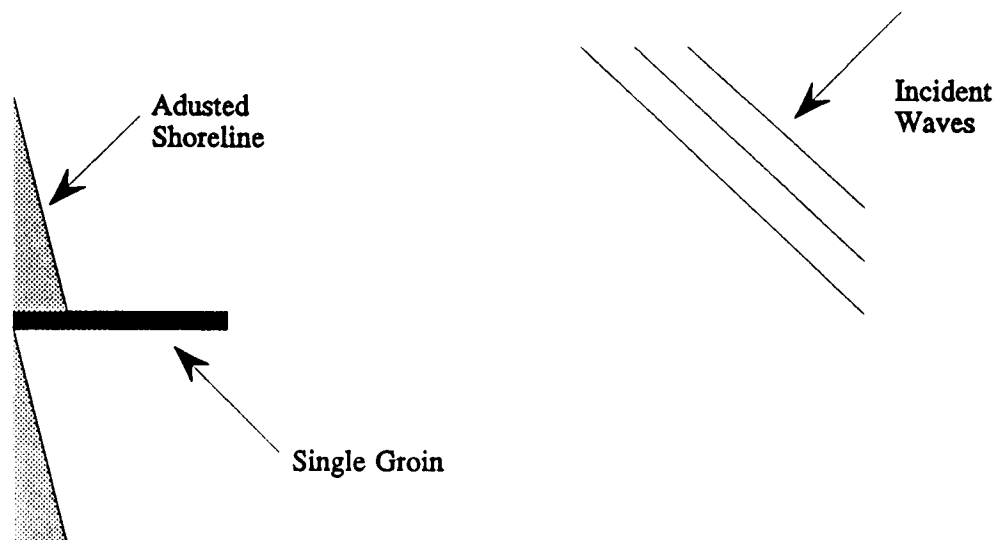


Figure 5.1a Adjusted shoreline for a single groin.

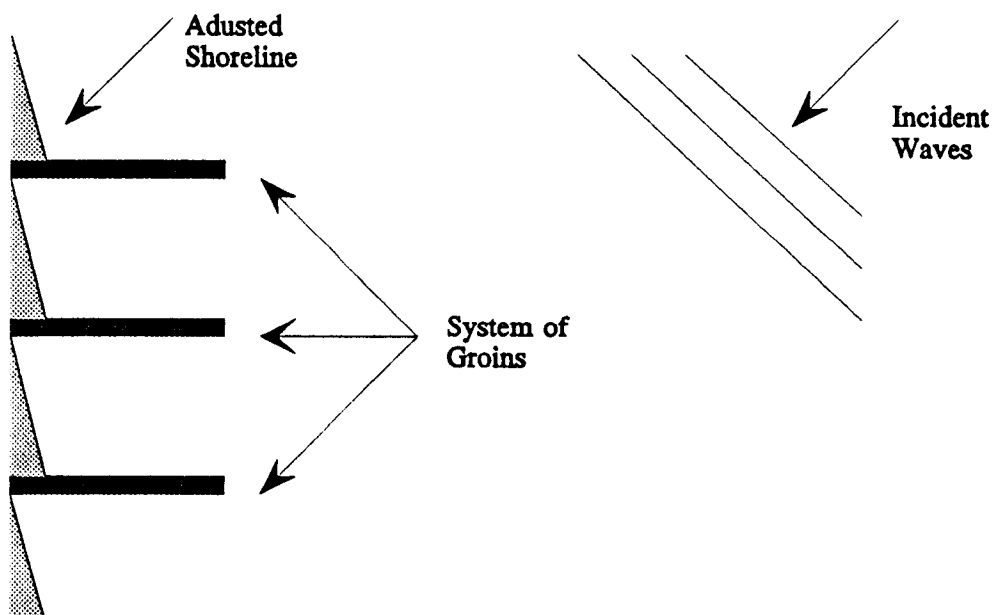


Figure 5.1b Adjusted shoreline for a system of groins.

be necessary to build another groin. A system or field of groins is usually built to stabilize a long stretch of coastline as shown in Figure 5.1b. The erosion process is shifted from one groin to the other in the longshore direction.

## 5.2 Groin Design and Predicted Circulation

The circular wave basin at the WRL was used to examine circulation around a single groin and two groins placed perpendicular to the shoreline. Results from Chapter 3 show that the spiral wavemaker in the circular wave basin generates a strong current in the longshore direction. Therefore, the circular wave basin provides an opportunity to study the impact of groins on an open coastline.

The length of the groins was determined by visual observation of the distance offshore to the breaker line. The distance from the shoreline to the breaker line was approximately 20-25 cm. The length of the groins were slightly longer than twice the distance from the shoreline to the breaker line. In the field, groins are typically built to this length or shorter to reduce erosion and trap sediment from the net longshore transport. The shoreline is 40 cm from the edge of the basin for still water depth of 35.56 cm next to the wavemaker. Thus, the groins were constructed to a length of approximately 100 cm from the edge of the basin. A wooden template was made to fit the beach profile and the groins were fabricated out of 16 gauge sheet metal. The placement of single groin in the circular wave basin is shown in Figure 5.2.

With the groins in the circular wave basin, the longshore flow will be diverted around the structures since they are impermeable. Dean (1978), proposes two

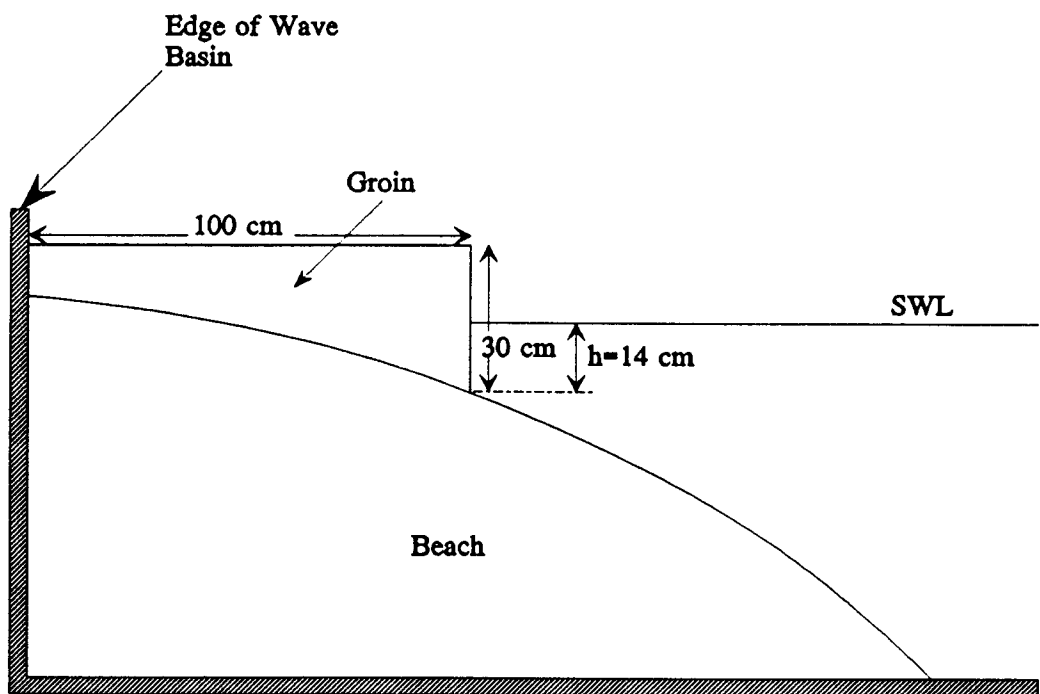


Figure 5.2 Groin design and placement in circular wave basin.

mechanisms for the generation of rip currents and cell circulation in and around groins. These cases are for waves approaching the shoreline at an oblique angle of incidence. The first case, shown in Figure 5.3a shows a rip current along the updrift side of the groin. This is due to the channelling of the net longshore flow by the groin. The current is fixed in position and flows along the adjusted shoreline and out along the updrift edge of the groin. The second case, shown in Figure 5.3b is a prediction of current circulation between two groins. The circulation is a result of a gradient in setup where the updrift groin acts as a shield to the incident waves. A gradient in wave height is generated in the longshore direction from the updrift to the downdrift groin. The flow of the current travels with the longshore gradient of setup and a circulation cell is generated. In predicting the circulation around groins, each case shows the possible existence of rip currents as a result of the groins acting as barriers and guides for the longshore flow. Presently, there is little published research available on the prediction of currents around a groin field in a laboratory environment.

### **5.3 Groin Circulation Experiments**

Two tests were designed to measure the circulation around groins in the circular wave basin. The first case consisted of one groin placed perpendicular to the shoreline. A second groin was added normal to the shoreline for the second case to simulate a groin field. The second groin was placed approximately 2-3 surf zone widths from the first groin as recommended by the Shore Protection Manual (1984).

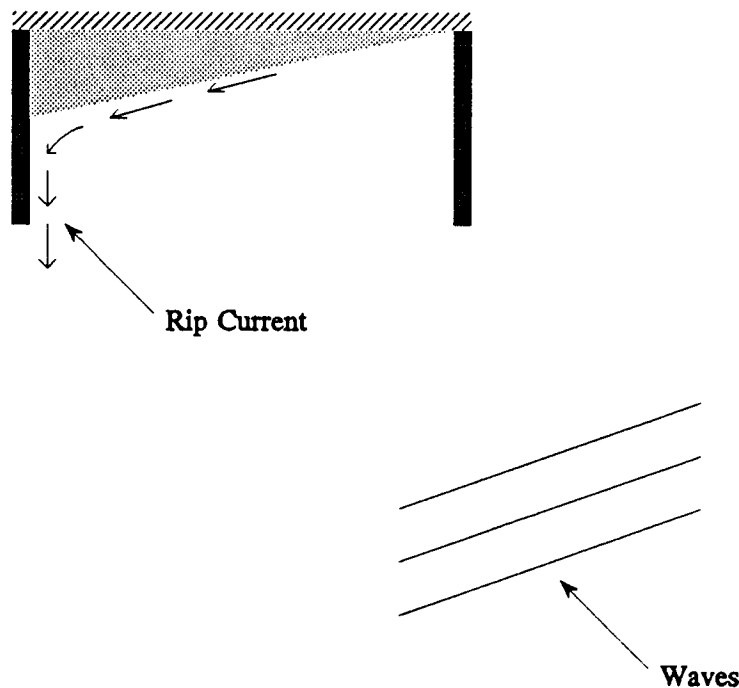


Figure 5.3a Generation of rip current within two groins (Dean, 1978).

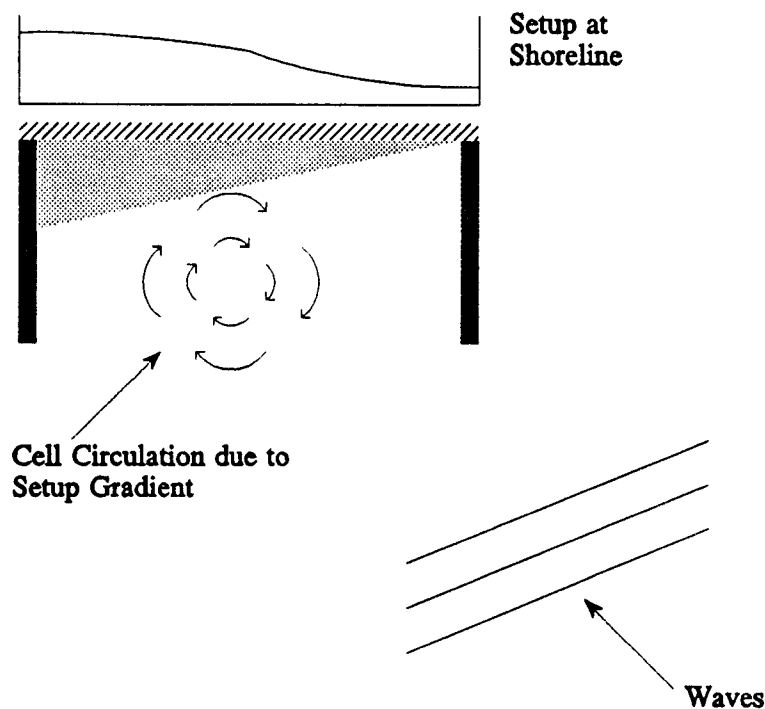


Figure 5.3b Generation of cell circulation within two groins (Dean, 1978).

The groins were attached to the beach with anchor bolts. A silicone sealer was applied between the groins and the surface of the beach to make the groin completely impermeable. Monochromatic waves were run for both tests at a basin water depth of 35.6 cm with  $T=1.0$  sec and  $H=7.6$  cm.

The video imaging system was used to track the ball and velocities were calculated as previously described in Chapter 3. The ball was tracked to determine the velocities close to the groin and within the cell created by the two groins. Program LSCBALL was modified to calculate the magnitude and direction of the resultant velocity of the ball. The new program, VGROIN, listed in Appendix A, divides the section of the wave basin where the structures are into a grid with respect to  $r$  and  $\Theta$ . The origin of the coordinate system is the center of the wavemaker and an average value for  $r$  and  $\Theta$  were calculated for each grid section. For the resultant velocities, both the magnitudes and directions were summed and averaged in each section. The average velocity vector was then positioned in the center of each corresponding grid region.

Figures 5.4 and 5.5 show plots of velocity vectors for each case. The velocity vectors were drawn in proportion to the scale shown on the right side of each figure. The groins were also drawn to scale with respect to the SWL and positioned perpendicular to the shoreline. Figure 5.4 shows the flow with one groin in the circular wave basin. For this case, the test was filmed for 30 minutes. For the duration of the run, the ball was continually being pushed forward by the waves into the groin and remained in general, just updrift of the groin. The ball would frequently

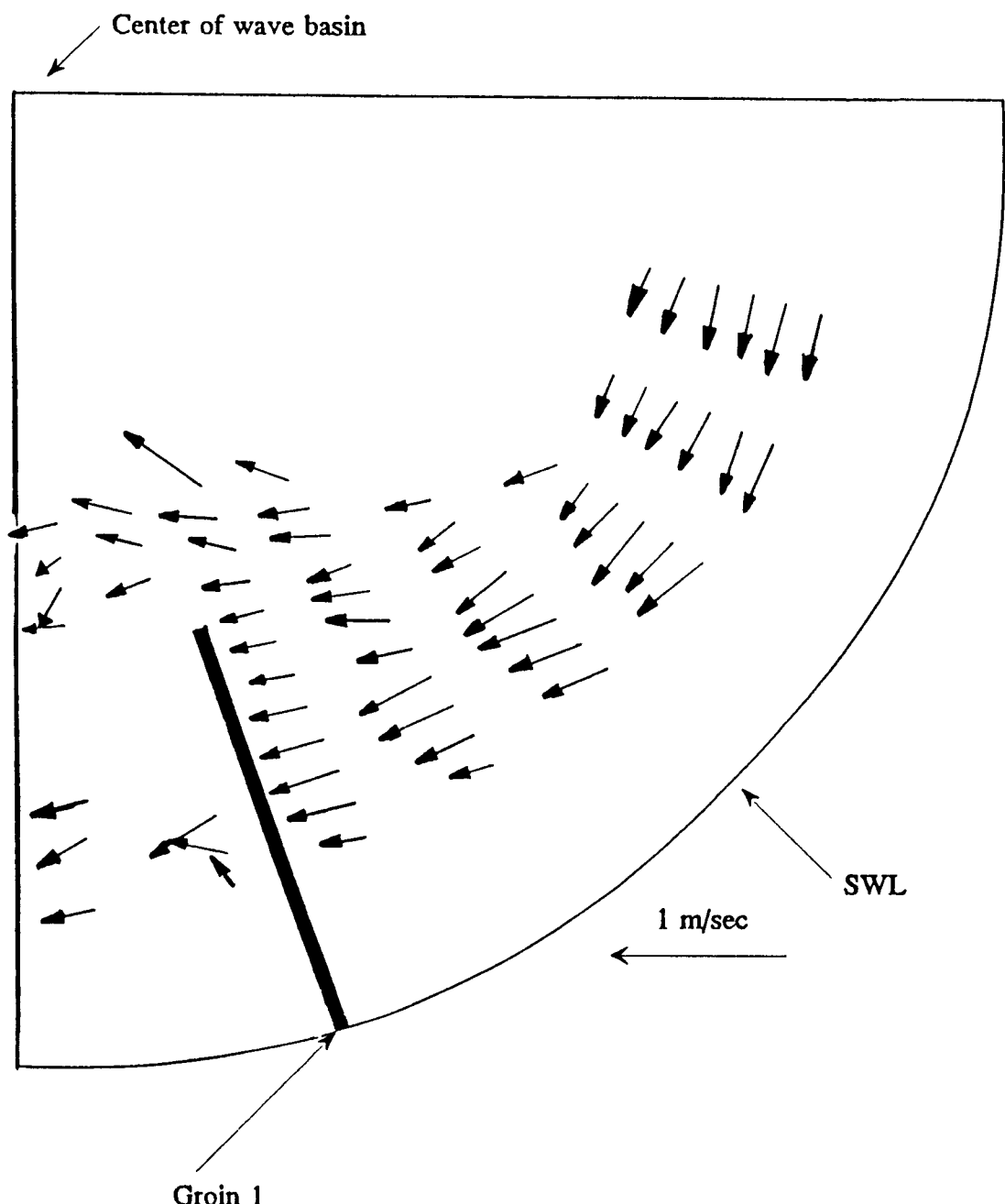


Figure 5.4 Velocity vector field with one groin:  $T=1.0$  sec,  $H=7.6$  cm.

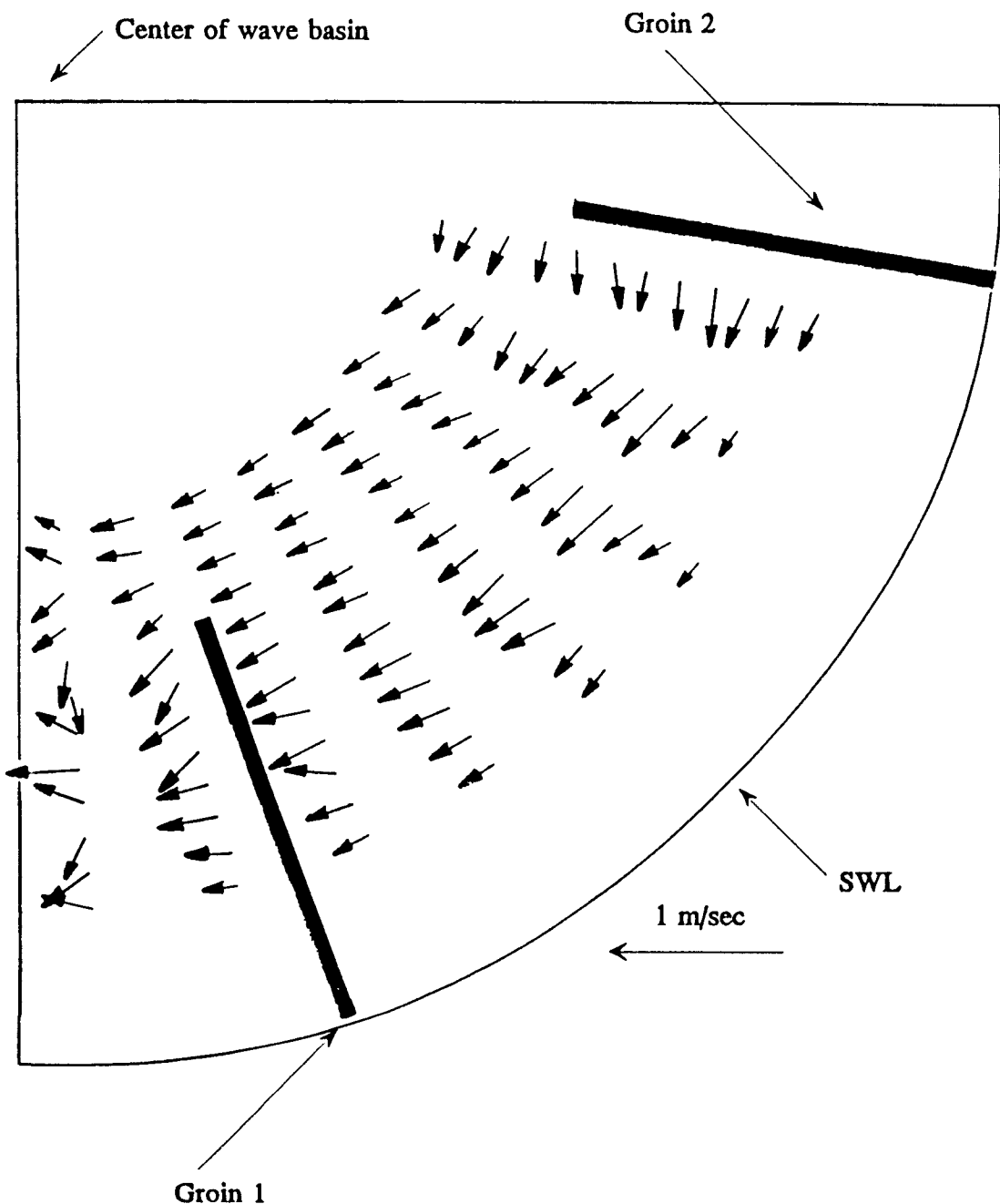


Figure 5.5 Velocity vector field with two groins:  $T=1.0$  sec,  $H=7.6$  cm.

recirculate in this region in the opposite direction of the longshore flow. The velocity vector field does not show this recirculation because the ball would mostly flow away from the groin when in contact with the beach and the data was discarded. The majority of the flow on the updrift side seems to be directed towards the groin with varying magnitudes. The offshore flow was directed slightly towards the center of the wavemaker. When the ball flowed around the groin, it would either become caught in the current towards the wavemaker or it would circulate on the downdrift side of the groin. There are no velocity vectors shown in one region on the downdrift side of the groin. This was because the ball would make a semi-circular path on the downdrift edge of the groin and then flow directly forward in the longshore direction.

Figure 5.5 shows the flow between two groins. This test was also video taped for 30 minutes. For the duration of the run, the ball remained between the two groins. The flow between the two groins seemed to remain steady in the longshore direction. The magnitude of the velocities adjacent to the shoreline are smaller because at this location the ball would flow both towards the downdrift and updrift groins. Unfortunately, the time the ball was flowing in the direction towards the updrift groin, it was in contact with the beach and the data was discarded. In both cases, there were strong currents on the updrift side of the groins. However, the data does not show this because any time the ball was trapped in this current along the groin and begin flowing out towards the wavemaker, a wave would break and push it back up towards the beach.

Figure 5.6 shows the average longshore velocity with the insertion of one groin

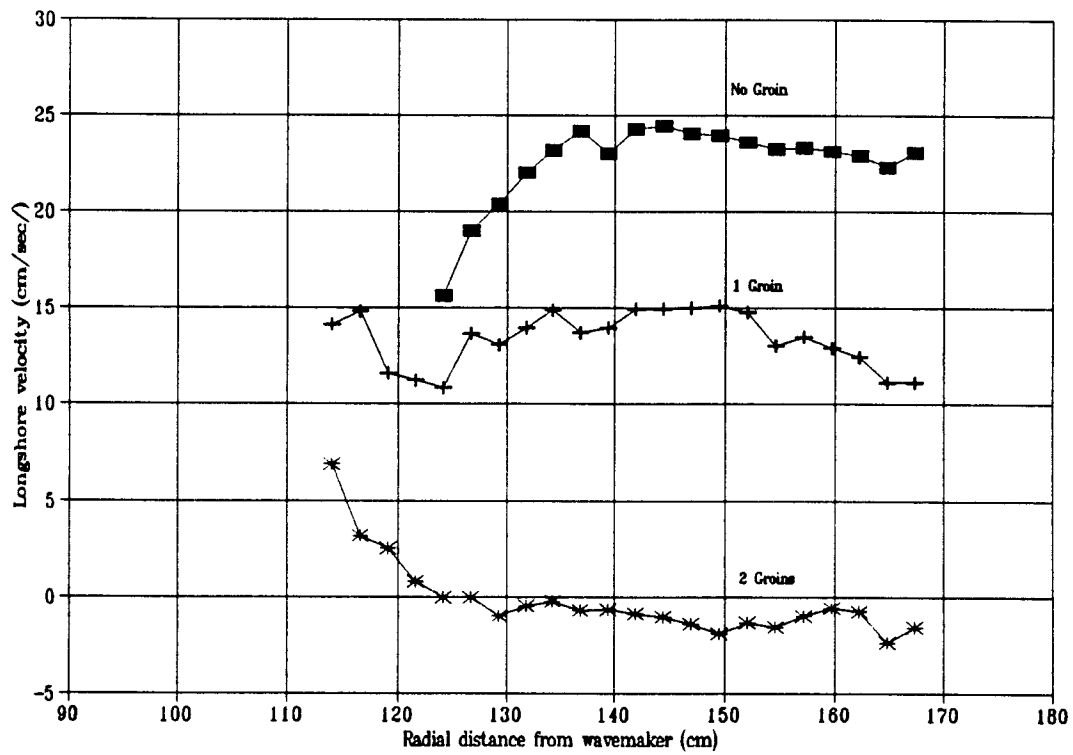


Figure 5.6 Average longshore velocity with and without groins:  
 $T=1.0$  sec,  $H=7.6$  cm.

and two groins compared to data taken without the groins. The edge of the groin is approximately 130 cm from the wavemaker. With one groin in the wave basin, the longshore velocity seemed to remain between 10 and 15 cm/sec across the surf zone. There is a slight dip in the velocity just offshore of the edge of the groin. With two groins the longshore velocity within the cell is negative and offshore from the edge of the groin it is positive. The direction of the longshore current in the groin field is from the downdrift to the updrift groin. Offshore, outside the edge of the groins, the velocity is in the direction from the updrift to the downdrift groin. In both cases, the groins significantly reduce the longshore current.

## Chapter 6

### Conclusions

#### 6.1 Summary of Results

The small circular wave basin at the WRL was successfully used to study coastal processes in a laboratory environment. With the construction of a beach in the circular wave basin, an infinitely long stretch of coastline was created with waves breaking obliquely to the shoreline. Initial measurements taken with the 3-D acoustic current meter verified the existence of strong currents in the longshore direction. With the insertion of fins on the tank bottom, the wavemaker induced circulation was reduced. As a result of the fins, the longshore current increased steadily in the radial distance from the wavemaker to the breaker line. The magnitude of the circulation in the wave basin remained steady over a long period and gave similar results for repeated tests.

Three different types of coastal processes were examined with the circular wave basin; longshore currents, shear waves, and groin circulation. To measure longshore currents a video tracking system was developed which enabled the calculation of velocities in the surf zone where the water depths were too shallow for current meters. Average longshore current profiles measured with the video technique and current meter were compared to numerical model results for longshore currents using NMLONG, developed by Kraus and Larson (1991). The longshore profile measured by the current meter for monochromatic waves with  $T=1.0$  second and  $H=7.6$  cm

compared favorably with the numerical model. The measured video longshore current profiles for monochromatic waves compared reasonable well with respect to the numerical model. However, the location of the peak currents measured with the video and predicted with the model did not correspond in cross shore location.

To examine the existence of shear waves in the circular wave basin, a spectral analysis was performed on cross shore currents, longshore currents, and water surface profile. Bowen and Holman (1989) and Oltman-Shay, et al. (1989) have both concluded through theory and field measurements that shear waves do exist and are energetic at very low frequencies. Spectra calculated for both the current meter and video measured longshore current show considerable energy in the low frequency bands. Thus, energetic long period motions of the longshore current are generated in the circular wave basin which may be a result of a shear instability.

The interaction of currents and groin structures was examined in the circular wave basin. Impermeable sheet metal groins were placed in the circular wave basin and velocities were calculated using the video tracking technique. The groins reduced the magnitude of the longshore current in the surf zone. With one groin, part of the resultant flow field was altered towards the wavemaker and with two groins, circulation patterns were observed between the two structures.

## 6.2 Future Research

It is the goal of a laboratory to produce experiments which model field situations. The impact of surf zone currents on coastal erosion is an extremely

important consideration in coastal engineering. This research has shown that coastal processes can be reasonably simulated by a spiral wavemaker in a circular wave basin. Future research should be focused on the full size circular wave basin at the WRL. In the larger wave basin, longshore currents, edge waves, and shear waves can be examined at a larger scale which will make measurements easier. The large circular wave basin will also enable an examination of longshore sediment transport.

### References

- Bowen, A.J. and Holman, R.A., Shear Instabilities of the Mean Longshore Current; 1. Theory, *Journal of Geophysical Research*, Vol. 94, pp. 18023-18030, 1989.
- Dalrymple, R.A. and Dean, R.G., The Spiral Wavemaker for Littoral Drift Studies, *Proceedings of the 13th Coastal Engineering Conference*, ASCE, pp. 689-704, 1973.
- Dean, R.G., Coastal Structures and Their Interaction with the Shoreline, *Application of Stochastic Properties in Sediment Transport*, H.W. Shen and H. Kikkawa, editors, Water Resources Publication, Littleton, Colorado, pp. 18,1-18,46, 1978.
- Dodd, N., Oltman-Shay, J. and Thornton, E.B., Instabilities in the Longshore Current, *Proceedings of the 22nd Coastal Engineering Conference*, ASCE, pp. 584-596, 1990.
- Elsasser, W.F., *A Random Spiral Wavemaker and Circular Wave Basin*, Engineering Project Report, Oregon State University, 1989.
- Kraus, N.C. and Larson, M., *NMLONG: Numerical Model for Simulating the Longshore Current*, US Army Corps of Engineers, Washington, DC, Technical Report DRP-91-1, 1991.
- Liu, P. L-F. and Dalrymple, R.A., Bottom Frictional Stresses and Longshore Currents due to Waves with Large Angles of Incidence, *Journal of Marine Research*, Vol. 36, pp. 357-375, 1978.

Longuet-Higgins, M.S., Longshore Currents Generated by Obliquely Incident Waves,  
1, *Journal of Geophysical Research*, Vol. 75, pp. 6778-6789, 1970.

Longuet-Higgins, M.S., Longshore Currents Generated by Obliquely Incident Waves,  
2, *Journal of Geophysical Research*, Vol. 75, pp. 6790-6801, 1970.

McDougal, W.G. and Hudspeth, R.T., Longshore Current and Sediment Transport on  
Composite Beach Profiles, *Proceedings of the 21st Coastal Engineering  
Conference*, ASCE, pp. 315-338, 1989.

McDougal, W.G. and Hudspeth, R.T., Influence of Lateral Mixing on Longshore  
Currents, *Journal of Ocean Engineering*, Vol. 13, pp. 419-433, 1986.

Mei, C.C., Shoaling of Spiral Waves in a Circular Wave Basin, *Journal of Geophysical  
Research*, Vol. 78, pp. 977-980, 1973.

Oltman-Shay, J., Howd, P.A., and Birkemeier, W.A., Shear Instabilities of the Mean  
Longshore Current; 2. Field Observations, *Journal of Geophysical Research*,  
Vol. 94, pp. 18031-18042, 1990.

*Physical Modeling in Coastal Engineering*, R.A. Dalrymple, editor, A.A. Balkema,  
Rotterdam, Boston, 276 pp., 1985.

*Shore Protection Manual*, Volumes I and II, US Army Corps of Engineers, Washington,  
DC, 1984.

Svendsen, I.A. and Jonsson, I.G., *Hydrodynamics of Coastal Regions*, Denmark,  
282 pages, 1976.

Thornton, E.B., and Guza, R.T., Surf Zone Longshore Currents and Random Waves: Field Data and Models, *Journal of Physical Oceanography*, Vol. 16, pp. 1165-1178. 1986.

Trowbridge, J., Dalrymple, R.A. and Suh, K., A Simplified Second-Order Solution for a Spiral Wavemaker, *Journal of Geophysical Research*, Vol. 91, pp. 11,783-789. 1986.

Williams, A.N. and McDougal, W.G., Hydrodynamic Analysis of Variable Draft Spiral Wavemaker, *Journal of Ocean Engineering*, Vol. 16, pp. 401-410, 1989.

## **Appendix**

## Appendix A: Computer Programs and Data Files

C      Program:Lscball

C-----  
C-----

C      This program calculates the velocity of a moving object  
 C      in the model spiral wave basin. A video camera is set up  
 C      above the wave tank to record on VHS tape the movement of an  
 C      object due to the motion of waves. The tape is then digitized  
 C      frame by frame by an image processor. The movement of the  
 C      object is then tracked in x,y coordinates in time by existing  
 C      software. The origin of the coordinate system is in the upper  
 C      left hand corner of the video screen. Coordinates are given in  
 C      pixels and time in Hr:Min:Sec:Frames. Two benchmark points are  
 C      read in order to translate the origin to the center of the  
 C      wavemaker. Distances between two successive points are  
 C      calculated and divided by the corresponding time difference.

C-----  
C-----

\$Debug

Program Lscball

Real L1,K  
 Real Hr,Min,Sec,Fr  
 Integer P,Kount,NumDR  
 Character \*12 A,AA

Dimension X1(10000),Y1(10000),T(10000),Tt(10000),Vt(10000)

Dimension Vrad(10000),Vtheta(10000),R(10000),Vr(10000)

Dimension Ravg(30),Vtbar(30),Vrbar(30),SD(30),Var(30),Nt(30)

Open (Unit=22, File='Vr.dat',Status='Unknown')  
 Open (Unit=24, File='Vt.dat',Status='Unknown')

C-----  
C-----

C      Name of the track data file and velocity output file

```

Write (*,*) 'Enter the tracking data file'
Read (*,5) A
5 Format (A12)
Open (Unit=10,File=A,Status='Old')
Write (*,*) 'Enter the filename for average velocities'
Read (*,10) AA
10 Format (AA12)
Open (Unit=12,File=AA,Status='Unknown')

```

C-----  
C-----

C Transformation of video origin to center of wave tank.  
 C Read in benchmark points to calibrate.  
 C Bm1x,Bm1y,Bm2x,Bm2y-Benchmark points to calibrate.  
 C X0,Y0-Center of the wavemaker.  
 C K-Calibration constant in pixels/centimeter.

```

13 Read (10,13) Bm1x,Bm1y
Format (8(/),F3.0,8X,F3.0)
Read (10,14) Bm2x,Bm2y
14 Format (1(/),F3.0,7X,F3.0)

```

C L1 is the diameter of the tank.  
 C K is the calibration constant  
 C Multiply x coordinates by 1.25 to account for aspect ratio

```

L1=457.20
Bm1x=1.25*Bm1x
Bm2x=1.25*Bm2x

```

```

K=Sqrt((Bm2x-Bm1x)**2+(Bm2y-Bm1y)**2)/L1
X0=(Bm2x/K)+228.6
Y0=(Bm2y/K)

```

C-----  
C-----

C Read in X and Y coordinates and Time(Hr:Min:Sec:Frames)  
 C N is the total number of coordinates  
 C Data file ends when X and Y are equal to -1  
 C If X and Y are equal to zero, no object has been tracked  
 C Video is digitized at 30 frames per second  
 C X1,Y1-Coordinates of moving object w.r.t center of wave tank.

C T-Time in seconds.

15     Read (10,15)  
      Format (1(/))

N=0  
Do 20 I=1,10000

16     Read (10,16) IX,IY,Hr,Min,Sec,Fr  
      Format (I4,7x,I3,9x,F2.0,1x,F2.0,1x,F2.0,1x,F2.0)

If (IX.eq.(-1.0).and.IY.eq.(-1.0))Then  
Goto 25  
Else  
EndIf

If (IX.eq.0.0.and.IY.eq.0.0)Then  
N=N  
Goto 20  
Else  
N=N+1  
X1(N)=((IX\*1.25)/K)-X0  
Y1(N)=Y0-(IY/K)  
T(N)=(Hr\*60\*60)+(Min\*60)+Sec+(Fr/30)  
EndIf

20     Continue

C-----  
C-----

C     Calculation of velocities  
C     If the time difference between two successive points is greater  
C     than 0.3 sec than the velocity between those two points is  
C     ignored and if it is less than 0.3 sec than it is retained.  
C     If two successive points are the same than the velocity is  
C     not calculated and the loop is continued.  
C     If the distance between two successive points is greater than  
C     10 cm, than the velocity is not calculated and the loop is continued.  
C     P is the number of good points.  
C     Velocity vectors are then placed midway between each pair of points.  
C     The X and Y components of velocity are then converted to polar  
C     coordinates with corresponding R and Theta values with respect to  
C     the center of the wavemaker.

C Dt-Time difference  
 C X2,Y2-Midway coordinates between two successive points.  
 C R,Theta-Polar coordinates with respect to X2,Y2.  
 C V-Velocities at midway points X2,Y2.

25 P=0.0  
 M=N-1  
 Do 30 I=1,M

Dt=T(I+1)-T(I)

If (Dt.gt.0.3) Then  
 Goto 30  
 Else

If (X1(I).eq.X1(I+1).and. Y1(I).eq.Y1(I+1))Then  
 Goto 30  
 Else

dx=abs(X1(I+1)-X1(I))  
 dy=abs(Y1(I+1)-Y1(I))  
 If (dx.gt.20.and.dy.gt.20) Then  
 Goto 30  
 Else

X2=(X1(I+1)+X1(I))/2  
 Y2=(Y1(I+1)+Y1(I))/2  
 Theta=ATan2(Y2,X2)

P=P+1  
 Sx=Sign(1.0,X1(I+1)-X1(I))  
 Sy=Sign(1.0,Y1(I+1)-Y1(I))

Vx=Sqrt((X1(I+1)-X1(I))\*\*2)/(Dt\*Sx)  
 Vy=Sqrt((Y1(I+1)-Y1(I))\*\*2)/(Dt\*Sy)

Vrad(P)=(Vx\*Cos(Theta))+(Vy\*Sin(Theta))  
 Vtheta(P)=-(Vx\*Sin(Theta))+(Vy\*Cos(Theta))  
 R(P)=Sqrt(X2\*\*2+Y2\*\*2)  
 T(P)=T(I)

EndIf  
 EndIf  
 EndIf

30 Continue

C-----  
C-----

C The surf zone in the model spiral wavemaker is divided into  
C radial sections of equal distance.  
C For each section the average velocity is determined by summing  
C all the velocities which coincide within that particular  
C section and dividing by the total number.  
C Rmax,Rmin,Dr=Max radius, min radius, and increment to average over.  
C NumDR is the number of sections to average the velocity over.  
C Kount=Number of velocities in given section.  
C Ravg=Average radius over specified section.  
C Vtbar,Vrbar=Average tangential and radial velocities in sections.  
C Vt=Vtheta-Vtbar in each section  
C Vr=Vrad-Vrbar in each section

Data Rmax,Rmin,Dr/168.6,92.4,2.54/  
NumDR=(Rmax-Rmin)/Dr

Write (12,44) A,P  
 44 Format(A10.2x,'Number of coordinates tracked = ',I4)  
 Write (12,45) 'Ravg', 'Vavg', 'SD', 'Nt'  
 45 Format(/,1x,A4,T11,A4,T21,A4,T31,A4,/1x, 40(''))

n=0  
 Rmin2=Rmax-Dr  
 Do 70 J=1,NumDR  
 Kount1=0.0  
 Kount2=0.0  
 SumVt=0.0  
 SumVr=0.0

Do 50 I=1,P

If(R(I).le.Rmax.and.R(I).gt.Rmin2)Then  
 SumVt=Vtheta(I)+SumVt  
 Kount1=Kount1+1.0  
 Else  
 EndIf

If(R(I).le.Rmax.and.R(I).gt.Rmin2)Then  
 SumVr=Vrad(I)+SumVr

```

        Kount2=Kount2+1.0
    Else
    EndIf

```

50 Continue

```
Ravg(J)=(Rmax+Rmin2)/2
```

```

If (SumVt.eq.0.0)Then
Vtbar(J)=0.0
Else
Vtbar(J)=SumVt/Kount1
EndIf

```

```

If (SumVr.eq.0.0)Then
Vrbar(J)=0.0
Else
Vrbar(J)=SumVr/Kount2
EndIf

```

C Subtract out the mean velocity in each section from  
C calculated values for Vtheta and Vrad within that particular section.

Do 55 I=1,P

```

If(R(I).le.Rmax.and.R(I).gt.Rmin2)Then
n=n+1
Vt(n)=Vtheta(I)-Vtbar(J)
Vr(n)=Vrad(I)-Vrbar(J)
Tt(n)=T(I)
Else
EndIf

```

55 Continue

C Calculation of standard deviation and variance for Vtheta

```

Kount=0.0
Sumt=0.0
Do 60 I=1,P

```

```

If(R(I).le.Rmax.and.R(I).gt.Rmin2)Then
Sumt=((Vtheta(I)-Vtbar(J))**2)+Sumt
Kount=Kount+1.0

```

```

Else
EndIf

60      Continue

Nt(J)=Kount

If (Sumt.eq.0.0)Then
SD(J)=0.0
Var(J)=0.0
Else
SD(J)=Sqrt(Sumt/(Kount-1))
Var(J)=Sumt/(Kount-1)
EndIf

C      For each increment, write average radius and velocity to file

65      Write (12,65) Ravg(J), Vtbar(J), SD(J), Nt(J)
          Format(3F8.3,7X,I4)

          Rmax=Rmax-Dr
          Rmin2=Rmin2-DR

70      Continue

C      Write Vr and Vt to a file with 4097 points

Do 80 I=1,4097

          Write (22,*) Tt(I), Vr(I)
          Write (24,*) Tt(I), Vt(I)

80      Continue

          Stop
          End
C-----
C-----

```

Track file: e:run10a.dat

Date: 08/27/91

Time: 13:23:20.36

Calibration coefficient

388.000000

BM1 x    BM1 y

437       226

BM2 x    BM2 y

49       226

x	y	Frame
---	---	-------

---

264	78	00:30:01:19
268	78	00:30:01:24
272	80	00:30:01:28
275	80	00:30:02:03
278	80	00:30:02:07
282	82	00:30:02:11
285	82	00:30:02:14
288	82	00:30:02:18
291	84	00:30:02:22
294	86	00:30:02:26
297	90	00:30:03:00
0	0	00:30:03:05
302	93	00:30:03:09
305	94	00:30:03:13
308	96	00:30:03:16
310	98	00:30:03:21
0	0	00:30:03:25
316	102	00:30:03:29
318	104	00:30:04:03
320	104	00:30:04:07
322	107	00:30:04:11
325	109	00:30:04:15
328	111	00:30:04:19
331	112	00:30:04:23
333	114	00:30:04:26
335	117	00:30:05:00
338	118	00:30:05:04
340	120	00:30:05:08
342	122	00:30:05:12
344	126	00:30:05:16
346	128	00:30:05:20

10a.dat Number of coordinates tracked=9766

Ravg	Vavg	SD	Nt
167.330	-14.316	6.824	861
164.790	-14.911	6.987	910
162.250	-15.834	6.180	869
159.710	-16.524	8.562	907
157.170	-16.216	8.791	884
154.630	-16.260	6.830	720
152.090	-15.297	10.136	615
149.550	-15.260	11.699	432
147.010	-13.967	10.265	294
144.470	-14.158	6.424	160
141.930	-13.562	5.431	126
139.390	-12.463	6.124	96
136.850	-13.129	6.811	65
134.310	-12.991	5.729	27
131.770	-12.783	4.402	8
129.230	.000	.000	0
126.690	.000	.000	0
124.150	.000	.000	0
121.610	.000	.000	0
119.070	.000	.000	0
116.530	.000	.000	0
113.990	.000	.000	0
111.450	.000	.000	0
108.910	.000	.000	0
106.370	.000	.000	0
103.830	.000	.000	0
101.290	.000	.000	0
98.750	.000	.000	0
96.210	.000	.000	0
93.670	.000	.000	0

C Program Vgroin: calculates velocity vector field around a single  
 C groin and two groins.

C-----

C-----

C This program calculates the velocity of a moving object  
 C in the model circular wave basin. The video camera is set up  
 C above the wave tank to record on VHS tape the movement of an  
 C object due to the motion of waves. The tape is then digitized  
 C frame by frame by an image processor. The movement of the  
 C object is then tracked in x,y coordinates in time by existing  
 C software. The origin of the coordinate system is in the upper  
 C left hand corner of the video screen. Coordinates are given in  
 C pixels and time in Hr:Min:Sec:Frames. Two benchmark points are  
 C read in to translate the origin to the center of the  
 C wavemaker. Distances between two successive points are  
 C calculated and divided by the corresponding time difference.

C-----

C-----

\$Debug

### Program Vgroin

Real L1,Kc,Pi  
 Real Hr,Min,Sec,Fr  
 Integer P,Kount  
 Character \*12 A,AA

Dimension X(10000),Y(10000),T(10000)  
 Dimension V(10000),Al(10000),R(10000),Th(10000)  
 Dimension Ravg(30,30),Vbar(30,30)  
 Dimension Thavg(30,30),Albar(30,30)

C-----

C-----

C Name of the track data file and velocity output file

Write (\*,\*) 'Enter the tracking data file'

Read (\*,5) A

5 Format (A12)

Open (Unit=10,File=A,Status='Old')

Write (\*,\*) 'Enter the filename for average velocities'

10     Read (\*,10) AA  
       Format (AA12)  
       Open (Unit=12,File=AA,Status='Unknown')

C-----  
 C-----

C     Transformation of video origin to center of wave tank.  
 C     Read in benchmark points to calibrate.  
 C     Bm1x,Bm1y,Bm2x,Bm2y-Benchmark points to calibrate.  
 C     X0,Y0-Center of the wavemaker.  
 C     Kc-Calibration constant in pixels/centimeter.

13     Read (10,13) Bm1x,Bm1y  
       Format (8(/),F3.0,8X,F3.0)  
       Read (10,14) Bm2x,Bm2y  
 14     Format (1(/),F3.0,7X,F3.0)

C     L1 is the diameter of the tank.  
 C     K is the calibration constant  
 C     Multiply x coordinates by 1.25 to account for aspect ratio

L1=457.20  
 Bm1x=1.25\*Bm1x  
 Bm2x=1.25\*Bm2x

Kc=Sqrt((Bm2x-Bm1x)\*\*2+(Bm2y-Bm1y)\*\*2)/L1  
 X0=(Bm2x/Kc)+228.6  
 Y0=(Bm2y/Kc)

C-----  
 C-----

C     Read in X and Y coordinates and Time(Hr:Min:Sec:Frames)  
 C     N is the total number of coordinates  
 C     Data file ends when X and Y are equal to -1  
 C     If X and Y are equal to zero, no object has been tracked  
 C     Video is digitized at 30 frames per second  
 C     X,Y-Coordinates of moving object w.r.t center of wave tank.  
 C     T-Time in seconds.

15     Read (10,15)  
       Format (1(/))

```

N=0
Do 20 I=1,10000

16      Read (10,16) IX,IY,Hr,Min,Sec,Fr
          Format (I4,7x,I3,9x,F2.0,1x,F2.0,1x,F2.0,1x,F2.0)

          If (IX.eq.(-1.0).and.IY.eq.(-1.0))Then
          Goto 25
          Else
          EndIf

          If (IX.eq.0.0.and.IY.eq.0.0)Then
          N=N
          Goto 20
          Else
          N=N+1
          X(N)=((IX*1.25)/Kc)-X0
          Y(N)=Y0-(IY/Kc)
          T(N)=(Hr*60*60)+(Min*60)+Sec+(Fr/30)
          EndIf

```

20 Continue

C-----  
C-----

C Calculation of velocities  
 C If the time difference between two successive points is greater  
 C than 0.3 sec than the velocity between those two points is  
 C ignored and if it is less than 0.3 sec than it is retained.  
 C P is the number of good points.  
 C Velocity vectors are then placed midway between each pair of points.  
 C The X and Y components of velocity are then converted to polar  
 C coordinates with corresponding R and Theta values with respect to  
 C the center of the wavemaker.  
 C Dt-Time difference  
 C X2,Y2-Midway coordinates between two successive points  
 C R-Polar coordinates with respect to X2,Y2  
 C Theta-Angle with respect to X2,Y2  
 C V-Velocities at midway points X2,Y2  
 C Vx,Vy-X and Y components of velocity, V  
 C Alpha-Angle with respect to Vx,Vy

25 P=0.0

```

Pi=4*ATAN(1.0)
M=N-1
Do 30 I=1,M

Dt=T(I+1)-T(I)

If (Dt.gt.0.3) Then
Goto 30
Else
EndIf

If (X(I+1).eq.X(I).and.Y(I+1).eq.Y(I))Then
Goto 30
Else
EndIf

dx=ABS(X(I+1)-X(I))
dy=ABS(Y(I+1)-Y(I))
If (dx.gt.10.and.dy.gt.10) Then
Goto 30
Else
EndIf

X2=(X(I+1)+X(I))/2
Y2=(Y(I+1)+Y(I))/2

P=P+1
Sx=Sign(1.0,X(I+1)-X(I))
Sy=Sign(1.0,Y(I+1)-Y(I))
Vx=Sqrt((X(I+1)-X(I))**2)/(Dt*Sx)
Vy=Sqrt((Y(I+1)-Y(I))**2)/(Dt*Sy)
V(P)=Sqrt(Vx**2+Vy**2)
R(P)=Sqrt(X2**2+Y2**2)

If (Vx.eq.0.0.and.Vy.lt.0.0)Then
Al(P)=270.0
Else
EndIf
If (Vx.eq.0.0.and.Vy.gt.0.0)Then
Al(P)=90.0
Else
EndIf
If (Vy.eq.0.0.and.Vx.lt.0.0)Then
Al(P)= 180.0

```

```

Else
EndIf
If (Vy.eq.0.0.and.Vx.gt.0.0)Then
Al(P)=0.0
Else
EndIf

Alpha=ATan2(Vy,Vx)
If (Alpha.le.Pi.and.Alpha.ge.0.0)Then
Al(P)=(Alpha*180)/Pi
Else
Al(P)=360+(Alpha*180)/Pi
EndIf

Theta=ATan2(Y2,X2)
If (Theta.lt.Pi.and.Theta.ge.0.0)Then
Th(P)=(Theta*180)/Pi
Else
Th(P)=360+(Theta*180)/Pi
EndIf

```

30 Continue

C-----  
C-----

C The surf zone in the model spiral wavemaker is divided into  
 C a grid with corresponding r and theta coordinates.  
 C For each section an average velocity vector is determined by  
 C summing up all the velocities which coincide within that  
 C particular section and dividing by the total number.  
 C Rmax,Rmin,Dr-Max radius, min radius, and increment to average over.  
 C Thmax,Thmin,DTh-Max angle, min angle, and increment to average over.  
 C Kount-Number of velocities in given section.  
 C Ravg,Thave-Average radius and angle of each section.  
 C Vbar,Albar-Average velocity and direction in each section.

```

Data Rmax,Rmin,Dr/170,90,5/
Data Thmax,Thmin,Dth/270,180,10/

```

```

NumDth=(Thmax-Thmin)/Dth
NumDr=(Rmax-Rmin)/Dr

```

```
Do 70 J=1,NumDth
```

```

Thmax2=Thmin+Dth
Do 60 K=1,NumDr
Kount=0.0
SumV=0.0
SumAl=0.0
Rmin2=Rmax-Dr

Do 50 I=1,P

If(R(I).le.Rmax.and.R(I).gt.Rmin2.and.
* Th(I).ge.Thmin.and.Th(I).lt.Thmax2)Then

SumV=V(I)+SumV
SumAl=Al(I)+SumAl
Kount=Kount+1.0
Else
EndIf

```

50 Continue

```

Ravg(J,K)=(Rmax + Rmin2)/2
Thavg(J,K)=(Thmin + Thmax2)/2

```

```

If (SumV.eq.0.0)Then
Vbar(J,K)=0.0
Else
Vbar(J,K)=SumV/Kount
EndIf

```

```

If (SumAl.eq.0.0)Then
Albar(J,K)=0.0
Else
Albar(J,K)=SumAl/Kount
EndIf

```

Write (12,\*) Ravg(J,K),Thavg(J,K),Vbar(J,K),Albar(J,K),Kount

Rmax=Rmax-Dr

60 Continue

```

Thmin=Thmin+Dth
Rmax=170

```

70 Continue

Return

End

C-----

C-----

C Program Linear Spline  
 C This program takes a date file of two arrays, XA and YA  
 C of length N and does a linear interpolation between each  
 C successive pair of data points.

\$Debug  
 Program Linspl2

Integer I,NP  
 Dimension XA(5000),YA(5000)  
 Character \*20 inputFile, outputFile

Write (\*,\*) 'Enter the length of the time series to be splined:'  
 Read (\*,\*) Ndata  
 Write (\*,\*) 'Enter the name of the input data file: '  
 Read (\*,5) inputFile  
 5 Format (A20)  
 Open (Unit=10,File=inputFile,Status='Unknown')  
 Write (\*,\*) 'Enter the name of the output data file: '  
 Read (\*,6) outputFile  
 6 Format (A20)  
 Open (Unit=15,File=outputFile,Status='Unknown')

Do 10 I=1,Ndata

Read (10,\*) XA(I), YA(I)

10 Continue

Dt=.20  
 NP=0

Do 40 I=2,Ndata

12 NP=NP+1

X=XA(1)+(NP\*Dt)

DIFT=X-XA(I)

If (DIFT) 15,20,25

15 Continue  
 YLow=YA(I-1)  
 Yhigh=YA(I)

Xlow=XA(I-1)  
Xhigh=XA(I)

Y=((X-Xlow)/(Xhigh-Xlow))\*(Yhigh-Ylow)+Ylow  
Goto 30

20 Continue

Y=YA(I)

X=XA(I)

Goto 30

25 Continue

NP=NP-1

Goto 40

30 Write (15,\*) X,Y

Goto 12

40 Continue

Stop

End